Characterization and Modelling of Additively Manufactured Hastelloy X Parts under Quasi-Static and Cyclic Loading

by

Reza Esmaeilizadeh

A thesis
presented to the University of Waterloo
in fulfillment of the
thesis requirement for the degree of

Doctor of Philosophy
in
Mechanical and Mechatronics Engineering

Waterloo, Ontario, Canada, 2021

Examining Committee Membership

The following served on the Examining Committee for this thesis. The decision of the Examining Committee is by majority vote.

External Examiner	IGOR YADROITSEV, Ph.D.
	Professor, Central University of Technology
Supervisor	EHSAN TOYSERKANI, Ph.D.
	Professor, University of Waterloo
Supervisor	HAMID JAHED, Ph.D.
	Professor, University of Waterloo
Internal Member	NORMAN ZHOU, Ph.D.
	Professor, University of Waterloo
Internal Member	KAAN INAL, Ph.D.
	Professor, University of Waterloo
Internal-External Member	ADIL AL-MAYAH, Ph.D.
	Associate Professor, University of Waterloo

Author's Declaration

This thesis consists of material all of which I authored or co-authored: see Statement of Contributions included in this thesis. This is a true copy of the thesis, including any required final revisions, as accepted by the examiners.

I understand that my thesis may be made electronically available to the public.

Statement of Contributions

I would like to acknowledge my co-authors who contributed to the research described in this thesis:

- Prof. Ehsan Toyserkani: Supervision of the research, providing the original idea for the current thesis, editing and reviewing papers, providing experimental facilities, providing funding.
- Prof. Hamid Jahed: Supervising the research work in the area of mechanical testing, fatigue analysis and modeling, editing and reviewing papers, providing experimental facilities.
- Dr. Ali Bonakdar: Guiding the research and providing editorial feedback in the preparation of the individual manuscripts in Chapters 4-6.
- Dr. Usman Ali: Providing editorial feedback in the preparation of the individual manuscripts in Chapters 3-6 and running the CT scanning experiments and analyzing the nano-CT data.
- Dr. Behzad Behravesh: Providing technical training in mechanical testing and editorial feedback in the preparation of the individual manuscripts in Chapters 4-6.
- Dr. Yahya Mahmoodkhani: Providing editorial feedback in the preparation of the individual manuscripts in Chapters 3-4.
- Dr. Ehsan Marzbanrad: Providing editorial feedback in the preparation of the individual manuscripts in Chapter 3.
- Mr. Ali Keshavarzkermani: Conducting sample preparation and EBSD analysis and providing editorial feedback in the preparation of the individual manuscripts in Chapters 3-6.

Abstract

Laser powder-bed fusion (LPBF) is one of the main additive manufacturing (AM) methods, which has been proven to produce complex metallic parts with fine features. Understanding the correlation of process parameters to the microstructure and mechanical properties of the printed parts are one of the biggest challenges in the AM community. In this thesis, the manufacturability, performance and durability of LPBF Hastelloy X (HX) parts are investigated under quasi-static and cyclic loading.

To this end, the variation of density and surface roughness using X-Ray computed tomography and laser confocal profilometry respectively, were studied across the build plate to find the optimal region on the build plate for printing to minimize the variability of the printed samples. After obtaining the best possible location for the least amount of scatter in the parts' properties, the effects of manufacturing process parameters on the printed parts were of prime importance. As the laser scanning speed (LSS) has been shown to be one of the most significant process parameters in LPBF, the effects of LSS on the macro/microstructure using optical and electron microscopy on the printed parts were also studied. Grain structure of the LPBF parts was studied using electron back scattered diffraction (EBSD). Although, quasi-static properties of the LPBF parts have been found to be superior to the conventionally manufactured (CM) parts, their performance under cyclic loading has yet to be fully investigated. Such investigation is critical since HX components used in combustor liner and fuel nozzle are under fluctuating loads in real life applications. Moreover, it has been found that the volume fraction of defects and surface roughness of AM is more than CM. The effect of defects on fatigue performance can be minimized by choosing proper combination of process parameters. Reaching the proper combination of manufacturing conditions for acceptable performance under fatigue loading will bring the next step, which is the ability to predict the life under cyclic loading. Strain-controlled fatigue tests using servo-hydraulic frames were performed to investigate the proper fatigue modelling approach for the LPBF-HX samples. Finally, the fracture surfaces of the fatigue samples were analyzed using scanning electron microscope (SEM) to investigate the crack initiation and propagation steps.

It was concluded that the spatter generation, which is inevitable in LPBF process, affects the powder bed characteristics and spatter distribution, which is highly dependent on the machine architecture, causes a significant variability between parts printed on different locations. It was

found that spatter rich region is formed close to the gas outlet and contains parts with inferior surface roughness and larger porosities. Moreover, porous parts were manufactured at extremely high and low values of LSS and in the moderate LSS values, nearly full dense parts were obtained. At the nearly full dense processing window of LPBF-HX parts, the quasi-static properties are dependent on the microstructure, which is affected by the LSS. Parts printed with lower LSS in the nearly full dense window possess longer lives in low-cycle fatigue (LCF) tests due to smaller pre-strain damage and hysteresis stabilization at lower strains. On the other hand, higher LSS parts perform better in high-cycle fatigue (HCF) region where surface roughness plays an important role. Strain- and energy-based fatigue models were able to predict the fatigue lives under different loading conditions and fatigue design curves were constructed for strain and energy models.

Acknowledgements

The realization of this research work would have not been possible without the help and support of several people, to whom I wish to express my gratitude.

First and foremost, I would like to express my deepest gratitude to my supervisors, Prof. Ehsan Toyserkani, and Prof. Hamid Jahed for their guidance, caring, and patience through the completion of the work. I am mostly grateful for their friendship and persistent help during my graduate studies at the University of Waterloo.

I hereby acknowledge my thesis examining committee members, Prof. Igor Yadroitsev from Central University of Technology, Prof. Norman Zhou, Prof. Adil Al-Mayah, and Prof. Kaan Inal from the University of Waterloo for taking time to review my thesis and provide their valuable and constructive insights.

I thank my colleges in the Siemens project for their support and advice, Ali, Osezua, Francis, Pouyan, Shahriar, Katayoon, Ken, Dr. Ehsan Marzbanrad, Dr. Yahya Mahmoodkhani, Dr. Usman Ali and Dr. Ali Bonakdar. It would have not been possible to finish this work without the guidance and support of Dr. Behzad Behravesh.

I am also very grateful to all my colleagues at MSAM and FATSLAB laboratories for their friendship and assistance.

I acknowledge the support from Jerry Ratthapakdee and Karl Rautenberg for helping with design and printing of LPBF parts.

Furthermore, I would like to acknowledge the support of Natural Sciences and Engineering Research Council of Canada (NSERC), the Federal Economic Development Agency for Southern Ontario (FedDev Ontario) and Siemens Canada Limited.

Finally, and most importantly, I would like to thank my parents and my dear sister for their endless support and encouragement.

Dedication

To my Family.

Table of Contents

List of figures

Chapter 1

1 Introduction

1.1 Overview and Motivations

These days, reducing the energy consumption is crucial for most of the industries. For transportation industries, weight reduction by redesigning the parts could be a possible solution. However, these optimized designs are geometrically complex which makes their manufacturing almost impossible by conventional manufacturing processes. Additive manufacturing (AM), the general term used for the manufacturing methods in which a product is built up layer by layer using the CAD model, is being considered as alternative fabrication method. Producing complex geometries [1,2], multi-material/functionally graded materials and composites [3–8] are some of the benefits of Additive Manufacturing (AM) over traditional manufacturing techniques. Among different AM methods for metallic materials, laser powder-bed fusion (LPBF) has become more common in industry while being used to produce functional parts [9–11].

Before replacing the parts made with the conventional manufacturing processes, AM parts should pass the preliminary requirement for being used as structural components. Mechanical response of metallic AM parts is one of the main properties to study the requirements for load bearing parts. There are different approaches to mechanical properties from quasi-static to cyclic behaviour. Due to their fine solidified microstructural features because of high cooling rates during manufacturing, quasi-static behaviour of the metallic LPBF parts are above the conventionally made parts [12,13]. On the other hand, the surface roughness and defects of the parts produced by LPBF is the main reason which makes their cyclic behaviour worse than the conventionally made parts [14–16]. Decreasing the surface roughness would be the first step toward improving their cyclic properties. However, due to the complex geometries which are produced by AM it is not possible to machine the internal surfaces. Because of that, exploring the cyclic response of the samples with the as-built surface finish would be necessary as well. On the other hand, due to anisotropy which is a product of directional heat transfer and solidification, AM parts would show different response with respect to the building direction. This anisotropy and poor cyclic performance reduce the reliability and reproducibility of the AM parts [15,17].

1

Therefore, it can be concluded that understanding the LPBF parts performance under monotonic and cyclic loading is necessary for using these parts as structural components. In addition, reducing the need for post-processing by optimizing the process parameters to produce a sound part under cyclic loading is essential for large-scale adaption of AM parts.

1.2 Thesis Objectives

The ultimate goal in this research is to establish a link between AM manufacturing conditions, process parameters, the corresponding microstructure, properties, and fatigue performance of LPBF Hastelloy X parts. This is done by understanding the effects of manufacturing conditions on the as-built microstructure and mechanical behaviour of the additively manufactured Hastelloy X under quasi-static and cyclic loadings (Figure 1). To achieve this goal the following research objectives are proposed.

- **To quantify the effect of part locations and spatter particles on the quality of Hastelloy X printed parts**

In this study, a comparison will be made between the virgin and spatter powder particles. Chemical composition, phases, microstructure, morphology and thermal behavior of virgin and spatter Hastelloy X (HX) powders will be studied to assess their contributions to the powder bed quality. Moreover, surface roughness and density of the parts from different locations are studied. This part of the research will shed light on understanding the effect of manufacturing conditions on the variability of the sample properties in one single build plate. The best place in the build platform will be identified from the results of these parts.

- **To understand the effect of process parameters (laser scanning speed) on mechanical behaviour of Hastelloy X under quasi-static loading at different loading directions (Tension/Compression)**

A systematic study is made to understand the effect of laser scanning speed, one of the main process parameters in laser powder-bed fusion (LPBF), on the quasi-static tensile response of Hastelloy X at room temperature. The effect of different as-manufactured features, such as process defects and microstructure, will be investigated. In addition to that, the effect of loading direction will be analyzed as well to quantify the compressive properties of HX printed samples. These results will be employed to establish a link between process parameters, microstructure and quasi-static behaviour of LPBF HX.

- **To characterize cyclic behaviour of the additively manufactured parts with different manufacturing conditions**

Based on the previous study, full dense parts with minimized defect/flaw volume fraction and surface roughness will be manufactured. To fully characterize the behaviour of the samples, stress-controlled fatigue tests will be performed on the samples manufactured with optimized laser scanning speeds. Fracture surface and metallographic studies will be made on samples after applying cyclic loads to identify sites of crack initiation, crack propagation and final fracture. Root cause of crack initiation will be identified and related to the AM process parameters. Fatigue crack growth behaviour will be investigated to determine the effect of microstructure on the crack growth rate.

- **To investigate the different fatigue modelling approaches for life prediction of additively manufactured HX**

An attempt will be made to correlate the damage induced by cyclic load under strain-controlled testing condition to the life of the component. For this purpose, modelling the fatigue behaviour will be performed by selecting a suitable damage parameter in agreement with the observed damage mechanisms. Establishing fatigue life model(s) for prediction of fatigue life of parts made by LPBF. Most prominent strain- and energy-based fatigue damage model will be examined against the data. Fatigue design curves will be developed for the optimum manufacturing condition.
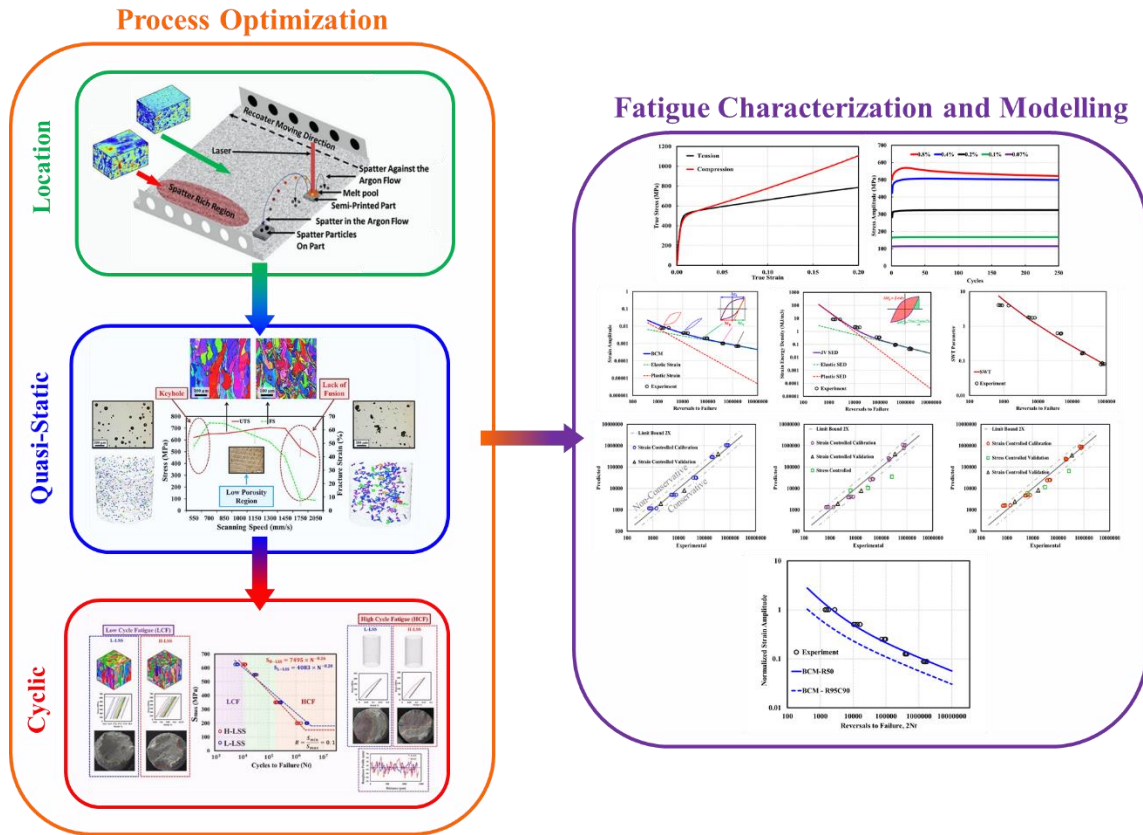
Figure 1 Thesis graphical abstract

1.3   Thesis Outline

The remaining contents of this thesis are organized as a manuscript-based thesis and it contains 7 chapters. Chapter 1 outlines the motivations, problem definition and objectives of the present research. Chapter 2 provides a review of the key topics and literature which is relevant to the current research. Chapters 3 to 6 are manuscripts which have been published or submitted for publication and the candidate is the first author of all manuscripts and is responsible for direct collection or co-ordination of data collection , and for the synthesis and analysis of the results. The only modifications made to each article are in the form of harmonizing references, table and figure numbers for unified integration into this larger thesis document.

Chapter 3 discusses the effect of spatter particle generation on the quality of Hastelloy X parts. A detailed characterization of the LPBF parts revealed a spatter rich region on the build plate that suffers from the higher surface roughness and larger porosities. Based on the findings of the chapter 3, spatter rich region was avoided in printing tensile coupons. A wide range of laser

scanning speeds (LSS) and the effect of changing LSS as a significant process parameter was investigated in chapter 4. Various type of defects (lack of fusion vs. keyhole porosities) and microstructures were characterized and their influences on the quasi-static tensile behaviour were studied. The key contribution of this research are the grain refining mechanisms in the nearly full dense window of the process parameters and finding the most important strengthening mechanisms in LPBF-HX through Hall-Petch analysis. Chapter 5 builds upon the contributions of the previous chapter, now extending the discussion of the effect of manufacturing conditions in the nearly full dense region to the mechanical response of the LPBF-HX samples under cyclic loading. Fatigue analysis over wide life span reveals that microstructure plays an important role in low cycle fatigue region where a significant amount of plastic strain is applied during cyclic loading. On the other hand, at high cycle fatigue region where most of life is spent on the crack initiation, surface roughness approved to be the critical feature. In chapter 6 the effect of loading direction (tension vs. compression) was investigated to study the asymmetry in mechanical behaviour of the LPBF-HX parts and symmetrical response has been observed. Moreover, based on the strain-controlled test results strain- and energy-based fatigue models are examined for different loading conditions and finally fatigue design curves are constructed for the strain and energy models. In chapter 7, conclusions and future work are outlined.

Chapter 2

2 Background and Literature Review

In this chapter after a brief overview of LPBF and metallurgy of nickel-based superalloys, the resultant microstructure and mechanical properties of nickel-based superalloys manufactured by LPBF will be reviewed and finally the common fatigue modelling approaches are studied.

2.1 Laser Powder Bed Fusion (LPBF)

In additive manufacturing (AM) or three dimensional (3D) printing process parts are produced layer by layer based on a CAD file design. In contrast to conventional manufacturing which a block is produced by casting or forging and final product is machined out of it, AM will produce directly the final geometry with minimum need for further processing [18,19] (Figure 2).
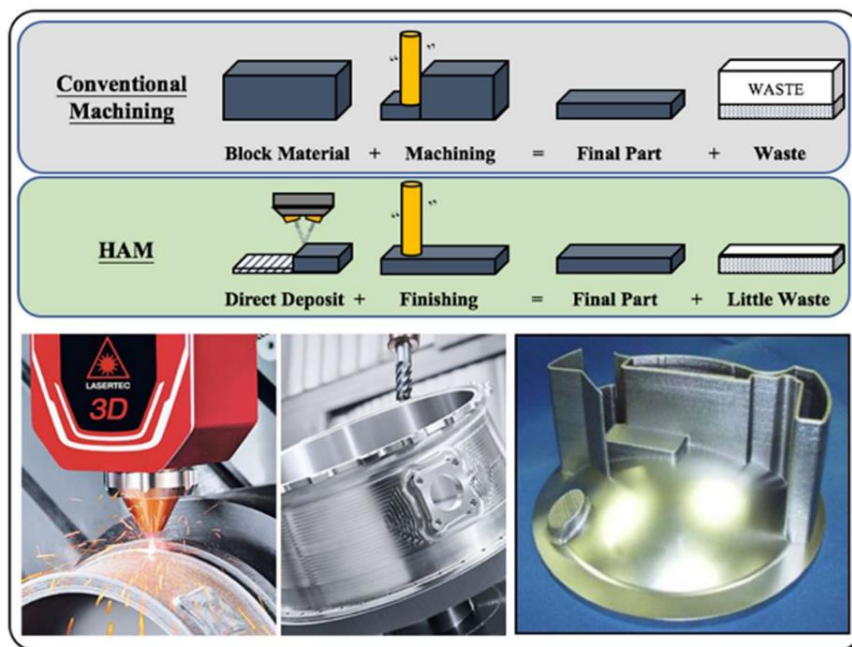
Figure 2 Concept of traditional (subtractive) and Additive Manufacturing [19]

In traditional manufacturing complex parts are made of different smaller and simpler parts which will be joined together in next steps. Interestingly, AM is able to produce complex parts in one step and will reduce the manufacturing steps to reach the final part [19]. Laser powder bed fusion (LPBF), Laser powder fed, Electron beam melting (EBM) and Binder jetting (BJ) are the main

AM methods which are used for producing metallic parts. There are different names for the LPBF process such as selective laser melting (SLM) or direct metal laser sintering (DMLS) based on the various developers. Generally, in LPBF a thin layer of powder is applied by the recoater system over the build area and laser will selectively melt specific regions of the build plate based on the cross section of the layered CAD file. This process will be repeated for successive layers until the manufacturing entire part (Figure 3). As indicated in Figure 3c there are different process parameters related to this process which the most important ones are laser power, scanning speed, hatching spacing and layer thickness. The large number of the process parameters involved in this process makes the process optimization necessary for specific materials under study. In LPBF, the minimum geometrical features sizes are between 40 and 200 μm [6] and the main limitations of the LPBF are low production rate and the need to powders with specific criteria [20].
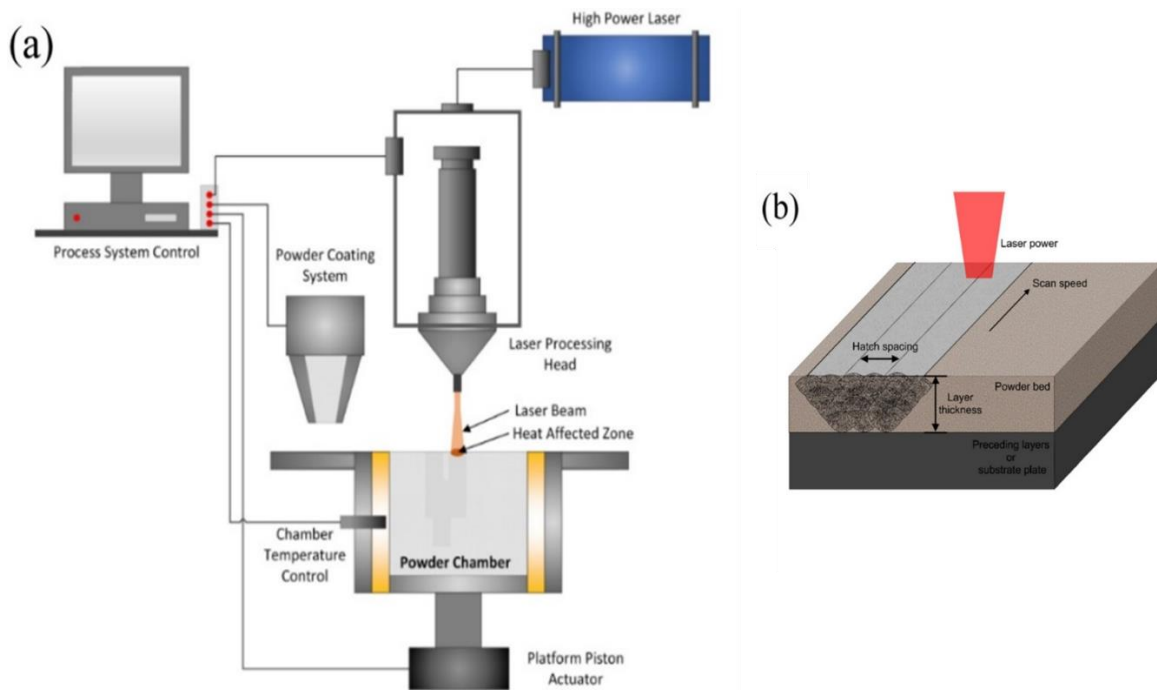
Figure 3 (a) Schematic of operating process design in LPBF showing its main constituents: laser source, computer system and build compartment systems and (b) close up of the LPBF process zone, showing the most important process parameters [6]

2.2   Nickel-Based Superalloys

Due to the ability to retain their strength at high temperature and perfect corrosion resistance Ni-based superalloys are mainly used in hot sections of the aero-engines [21], Figure 4a.

7

| (a) | (b) |
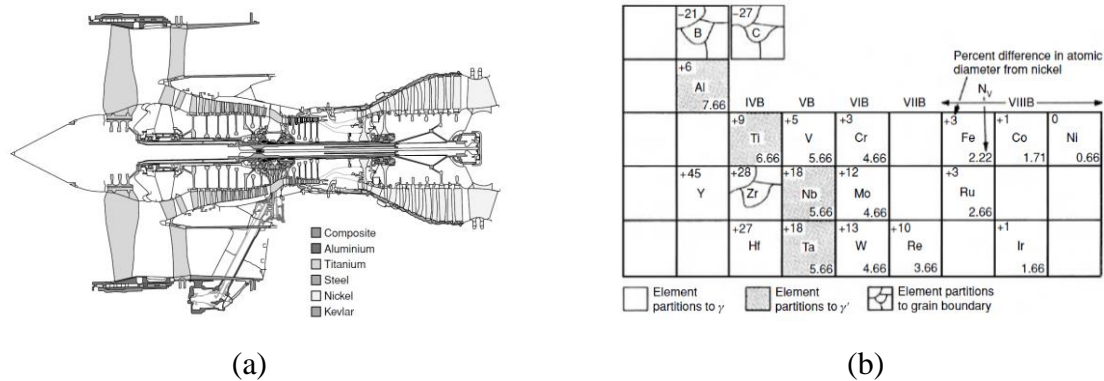
Figure 4 (a) Illustration of material usage in the Trent 800 engine. Note the extensive use of nickel-based superalloys in the combustor and turbine sections. (b) Categories of elements important to the constitution of the nickel-based superalloys [21].

Nickel-based superalloys are the most complicated engineered materials because they consist of up to ten alloying elements and different phases are present in their microstructure. The function of different alloying elements and different phases present in the microstructure will be discussed in this section.

2.2.1   Alloying Elements

The chemical composition of the three common Ni-based superalloys that have been widely studied in LPBF process are shown in Table 1. The role of the alloying elements is to make the alloy's response compatible with the design criteria.

Table 1 Nominal chemical composition of the three common LPBF processed superalloys: CM247LC, IN718 and Hastelloy X (HX) [17,22,23]

Element	Ni	Cr	Fe	Mo	Nb	Co	W	Ta	Al	Ti	Hf	Mn	C	B	Zr	Si
CM247LC	61.51	8.11	-	0.52	-	9.41	9.66	3.18	5.49	0.74	1.29	-	0.08	0.013	0.008	-
IN718	Bal.	19.2	19.6	3.0	5.2	-	-	-	0.43	0.95	-	0.16	0.05	-	-	0.21
HX	Bal.	21.3	19.5	9.0	-	1.04	0.56	-	-	-	-	0.48	0.057	-	-	0.32

Based on their function mainly alloying elements fall in three categories [24]:

1- Solid solution strengtheners: Co, Cr, Mo, W …

2- Precipitate formers: Al, Ti, Nb, Ta …

3- Grain boundary elements: C, B, Zr …

These alloying elements are distributed in the microstructure based on their size and chemical affinity to form specific phases. Solid solution elements have atomic radii not very different form that of nickel. Precipitate former elements will make new phases with the nickel and grain boundary elements will segregate toward the grain boundaries because their sizes are very different from the nickel as are highlighted in Figure 4b.

It should be noted that the specified categories in Figure 4b does not mean that the alloying element will not be present in other phases and parts of the microstructure. For example, tantalum exhibits a strong partitioning toward gamma prime with nominal partitioning ratio of 8 to 1 between gamma prime and the gamma matrix phase and it has solid solution strengthening effect in both phases. On the other hand, Ta is strong carbide former and it will also help high temperature properties in this way. Typically, 75 percent of Ta will partition to the gamma prime and 15 percent will form TaC and the rest will partition to the gamma matrix as a solid solution strengthener [24].

As-built microstructure is strongly related to the alloy chemistry. For solid solution hardening (SSH) alloys such as HX the as-printed microstructures consists of high dislocation density with little amount of carbides and no precipitate. Low carbon and precipitate former elements such as Al and Ti are responsible for this condition (Table 1) [17]. For IN718 higher amount of Nb in alloy composition has resulted in the formation of Laves phase with chemical formulae of (Ni, Cr, Fe)2(Nb, Mo, Ti) [23]. In comparison to CM247LC lower amount of Al and Ti did not let the gamma prime to form. On the other hand, high enough precipitate former alloying elements in CM247LC have led to presence of gamma prime in the as-built condition [22].

2.2.2   Phases and Microstructure of Nickel-Based Superalloys

Complex chemical composition of these alloys will produce different phases in microstructure. There are several phases present in the microstructure: Matrix, Geometrically Close-Packed (GCP), Topologically Close-Packed (TCP), carbides and borides [25]. In the following paragraphs a brief description of the most important features of these phases will be presented.

The matrix phase the Ni-based superalloys is FCC γ phase which has been selected to provide best performance at high temperatures due to several factors. It has optimal mechanical properties because of high modulus and multiple slip systems. Its high packing density cause low diffusivity

for alloying elements which would be desirable for high temperature applications. The FCC matrix let broad solubility for secondary elements which each of them are useful for specific purpose as discussed in the previous section [21].

GCP phases are intermetallics with the formula A_3B. The most important phases of these group are γ'-Ni$_3$(Al,Ti) and γ''-Ni$_3$Nb [25]. Due to the relative bonding energy of Ni-Ni, Al-Al and Ni-Al bonds, Ni-Al bonds are preferred in its FCC crystal structures which leads to long ordering (Figure 5a) in this phase and these precipitates are ordered even at high temperatures. The other feature of these ordered phase relative to the matrix is their relatively similar lattice parameter which enable these phases to establish coherent interfaces with the matrix. The properties of the superalloys are found to depend critically on the coherency of the γ/γ' interface. Coarsening of the γ' precipitates leads to loss of coherency with increasing the δ magnitude. γ' particles are mostly cubic in shape in the microstructure (Figure 5b). In superalloys containing nickel and iron such as IN718 which contain quantities of niobium, the primary strengthening precipitate is not γ' and a body-centred tetragonal (BCT) ordered compound with composition which can be represented approximately by γ''-Ni$_3$Nb is the main hardening phase. The γ'' displays a disc-shaped morphology, with 10 nm thickness and 50 nm diameter (Figure 5c).

| (a) | (b) | (c) |
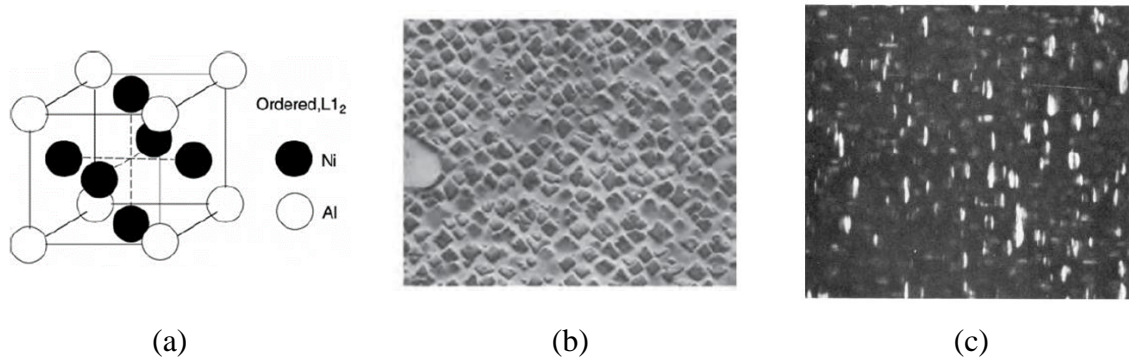
Figure 5 GCP phases (a) Ordered structure, (b) Cubic shape of Gamma prime and (c) Disc-shaped morphology of Gamma double prime [21]

Excessive quantities of alloying elements such as Cr, Mo, Nb, and Re promote the formation of specific intermetallic phases. High and uniform packing density of atoms, directional non-metallic bonding and complex crystallographic structures are the main features of these TCP phases. Generally, they have chemical formulae A_xB_y and Laves phases which are common in IN718 in the cast structure are from this group [21] (Figure 6a).

Various carbide and boride phases are formed in the Ni-based superalloys, depending on chemistry and the processing conditions. A number of morphologies, for example, globular, blocky and script have been reported (Figure 6b). Their role is a matter of controversy, but it is now accepted they can improve the creep properties, primarily due to their preferred location which is at the γ – grain boundaries. Thus, carbon and boron are often referred to as grain-boundary strengtheners. This explains the difference between the carbon and boron content of polycrystalline and single crystal superalloys. In the latter the grain boundary strengthening is not necessary due to lack of grain boundaries and their carbon content is lower than the polycrystalline alloys.

| (a) | (b) |
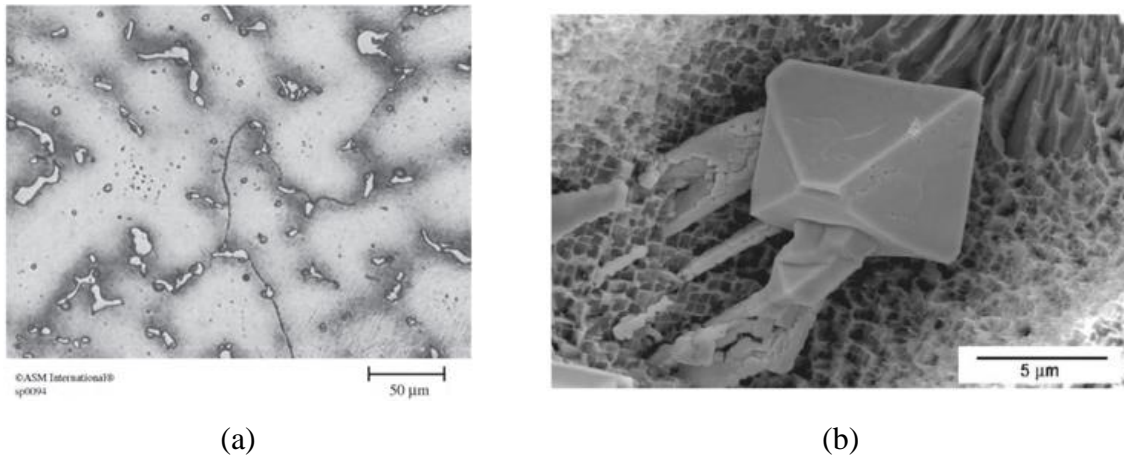
Figure 6 (a) Laves phase in IN718 cast structure [24] (b) Blocky MC carbide [21]

2.2.3   Strengthening Mechanisms

Several strengthening mechanisms are activated in Ni-based superalloys at high temperatures which help them to retain their mechanical properties. The main strengthening mechanisms are solid solution strengthening, precipitation hardening and grain boundary phases [21]. In solid solution strengthening the difference between the size of the solute and solvent (matrix) is a critical factor because it determines the amount of lattice distortion around the solute. The strain field surrounding the solute due to this distortion will interact with the strain field around the dislocation and make their movement on the slip plane more difficult (Figure 7a). It should be noted that by adding alloying elements to the matrix the stacking fault energy (SFE) of the matrix will change and generally addition of alloying elements will result in reduction of the SEF. Reduction of the SFE make the partial dislocation more separated and this will make the cross slip more difficult. Hence, solid solution elements will have two effect on the dislocations movements by imposing a strain field and reduction of the SFE.

11
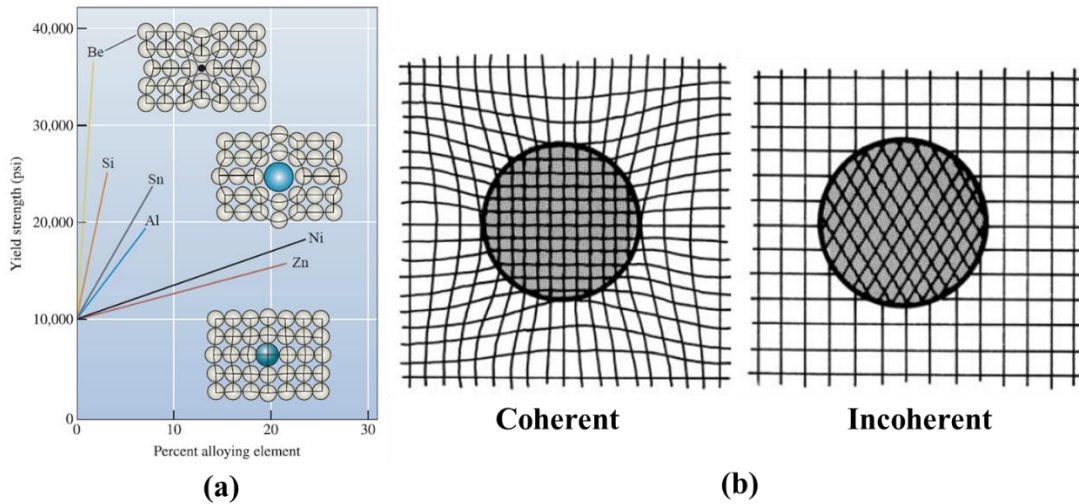
Figure 7 (a) Lattice distortion around solutes and strengthening effect of solute atoms [26], (b) Coherent and incoherent precipitates [27]

There are several factors which affect the precipitation hardening. The most important one is the crystallographic relationship between the matrix and the precipitates [21]. This will determine the type of the interface between them and precipitate dislocation interaction which are coherent and incoherent as shown in Figure 7b. If it is not possible to find similar arrangement of atoms in the matrix and precipitate incoherent interface will form and dislocations should bow between precipitates and make a loop around them in according to Orowan mechanism (Figure 8a). On the other hand, for coherent precipitates dislocations can shear the particles and cut them. The lattice misfit between the matrix and precipitates will interact with the moving dislocations and is able to increase to stress for dislocation movement.
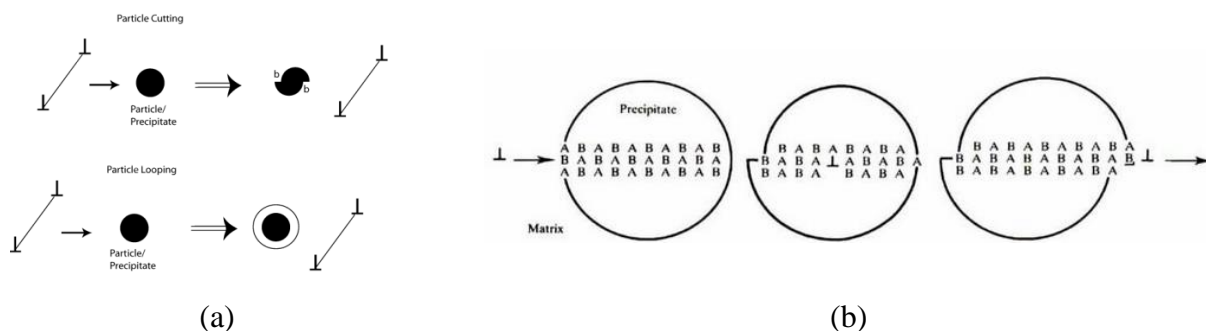
Figure 8 (a) Dislocation particle interactions, (b) Dislocation movement in an ordered phase [28]

As mentioned earlier the other important factor for precipitates in Ni-based superalloys is their long range ordered structure [21]. After passing the coherent interface dislocation will disturb the

local chemistry around the atoms as shown in Figure 8b and anti-phase boundary (APB) will impose an extra force on dislocation. In this ordered structures dislocations will move in pairs to minimize the disordered region in the ordered structures which is called superdislocation. These pair dislocations have been observed in Ni-based superalloys which indicates movement of dislocations in ordered precipitates as shown in Figure 9a.

(a)   (b)
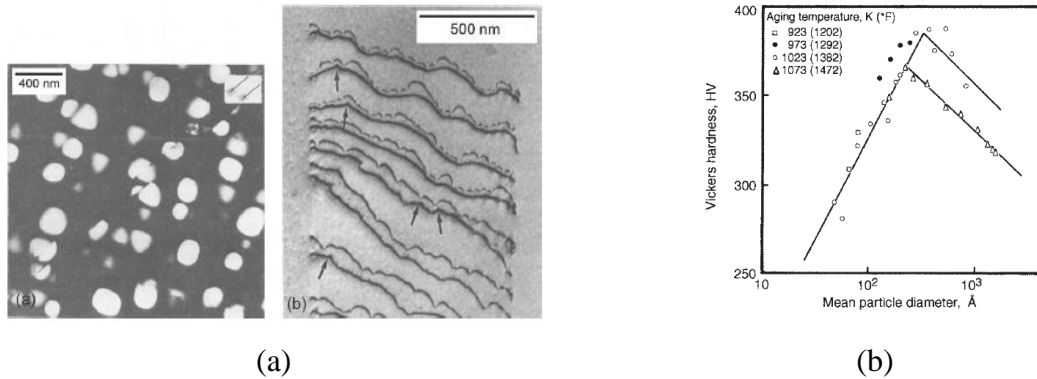
Figure 9 (a) Superdislocations in Ni-based superalloys, (b) Hardness variation during different heat treatments [21]

In addition to coherency and ordering, size and distribution of precipitates are crucial factors for strengthening. These factors are controlled by heat treatment, as the time is increased the precipitates will coarsen and their spacing will increase there would be a maximum in hardness which is correspond to the optimal distribution, size and interface features (Figure 9b).

Grain boundary phases which are mainly carbides and borides are mainly responsible for increase in the rupture life by reducing the creep rate through impeding grain boundary sliding. In many superalloys the MC carbide, which is usually rich in Ti, Ta and/or Hf since these are strong carbide formers, precipitates at high temperatures from the liquid phase. Consequently, the carbide and borides is often found in interdendritic regions and grain boundaries (Figure 10) due to carbon and boron segregation in these regions and with no distinct orientation relationship with the matrix is displayed. A number of morphologies, for example, globular, blocky and script have been reported [25].
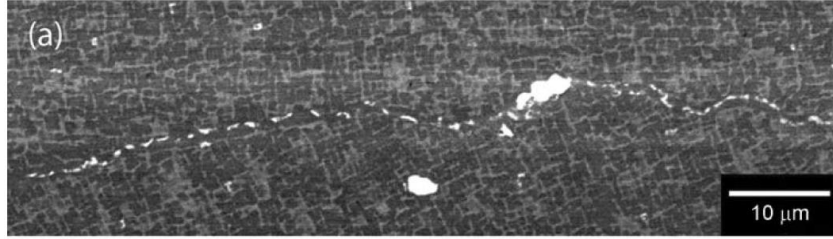
Figure 10 Precipitation of the M23C6 carbide on the γ –grain boundary [21]

Hastelloy X, the alloy under investigation in this thesis, has low amount of precipitate former elements and it is known as a solid solution strengthened alloy [25]. A combination of good corrosion resistance and high temperature strength make it a perfect candidate for usage in combustor liners of turbine engines [29].

2.3 Microstructure of Nickel-Based LPBF Parts

In this section firstly solidification conditions of the LPBF process will be investigated and the as-built microstructure of the Ni-based superalloys will be discussed. Microstructural features in different scales from grain to cells and alloying element distributions will be studied.

2.3.1 Solidification Microstructure

During LPBF melt pool is surrounded by three different phases which are air, metallic powder and substrate. Among these phases the solid substrate has the biggest thermal conductivity and is the main cause for the directional heat flow as shown in Figure 11a. The fastest heat flow direction would be always perpendicular to the solidification front or melt pool boundary toward the beneath substrate [30]. When laser heats the substrate, some remelting will happen and similar to autogenous welding the nucleation step is no longer needed and the solid will grow epitaxially from the remelted substrate. Due to similar chemistry of the substrate and the molten metal the interfacial energy between them is negligible and the interfacial energy between the molten metal and nucleus and substrate are approximately the same, therefore, the energy barrier for heterogeneous nucleation would be zero in contrast to casting (Figure 11b) [31].

(a)   (b)

Figure 11 (a) Heat flow condition in LPBF process [32] (b) Change in free energy due to formation of a new phase in different processes [31]
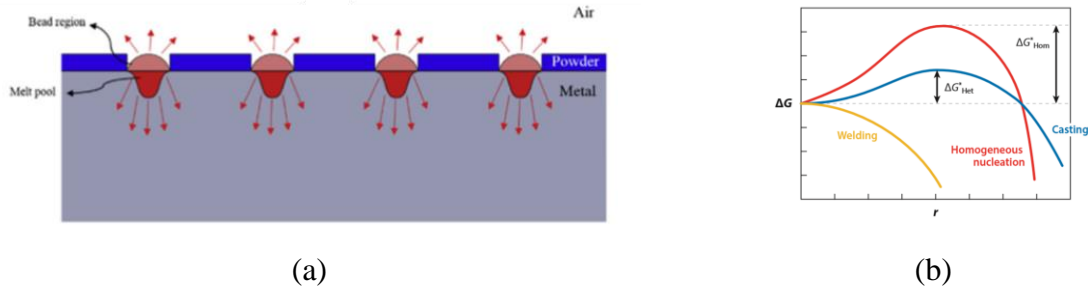
The morphology of the solidification microstructure is determined by the ratio of the G/R where G is the temperature gradient in front of the solidification front and R is solidification velocity (Figure 12a) [33]. Various experimental studies have shown that cellular solidification microstructure for LPBF process. Interestingly, cellular microstructure will remain through entire melt pool [34] in contrast to finally equiaxed solidified microstructure which has been observed in welding [33] as shown in Figure 12b, c and d.
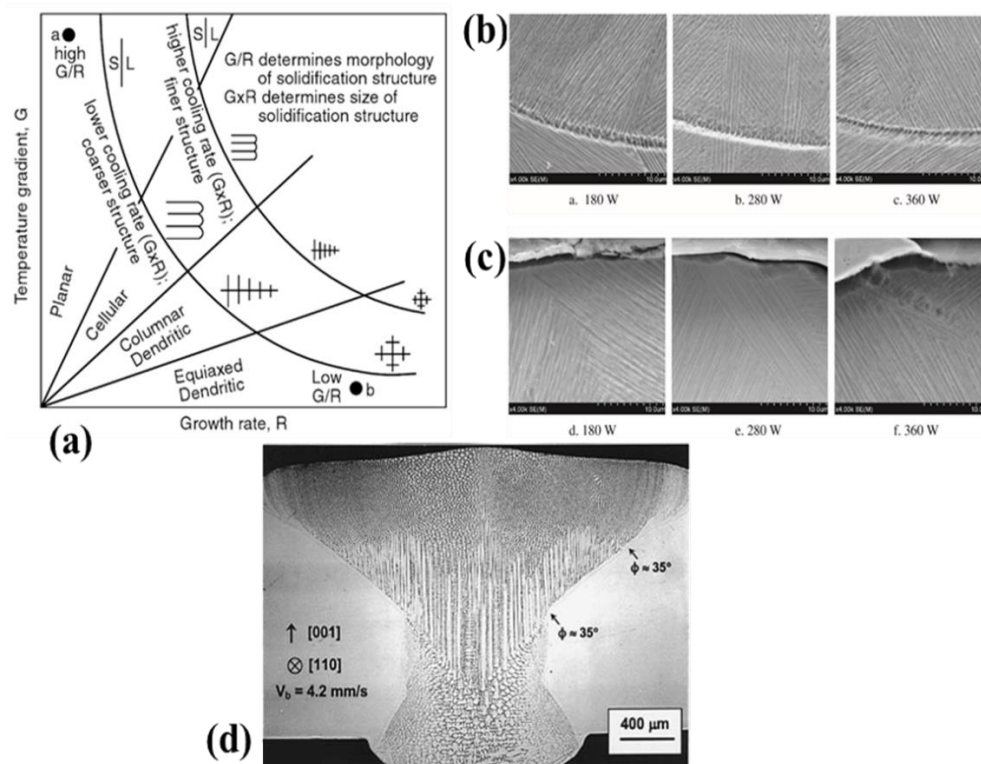
Figure 12 (a) Solidification microstructure map, (b) and (c) Cellular microstructure at the bottom and top of the melt pool respectively [34] and (d) Cellular to Equiaxed grains change in welding [33]

The solidification velocity is related to the laser beam speed $V_s = V_b \cdot \cos(\theta)$, where V_s is solidification velocity and V_b is laser beam velocity and θ is the angle between them as shown in Figure 13a [35]. Due to high laser beam speeds in LPBF in the range of 1 m/s the solidification velocity would be estimated as 0.173 m/s which is completely a high rate and it is proposed that $V_s \geq \frac{D_i}{\delta}$, where D_i is the interface diffusion and δ is interface thickness [36]. Therefore, the solidification front will move faster than the atomic diffusion and it will result in significant solute trapping [37]. Harrison et al. [36] have performed EDS in SEM to investigate the possibility of segregation around the cracks in the as-built materials and no segregation has been reported (Figure 13b). This could be an experimental result which support solute trapping in LPBF solidification condition, but it should be noted that the EDS resolution in SEM is in the range of 2-5 µm.

(a)   (b)
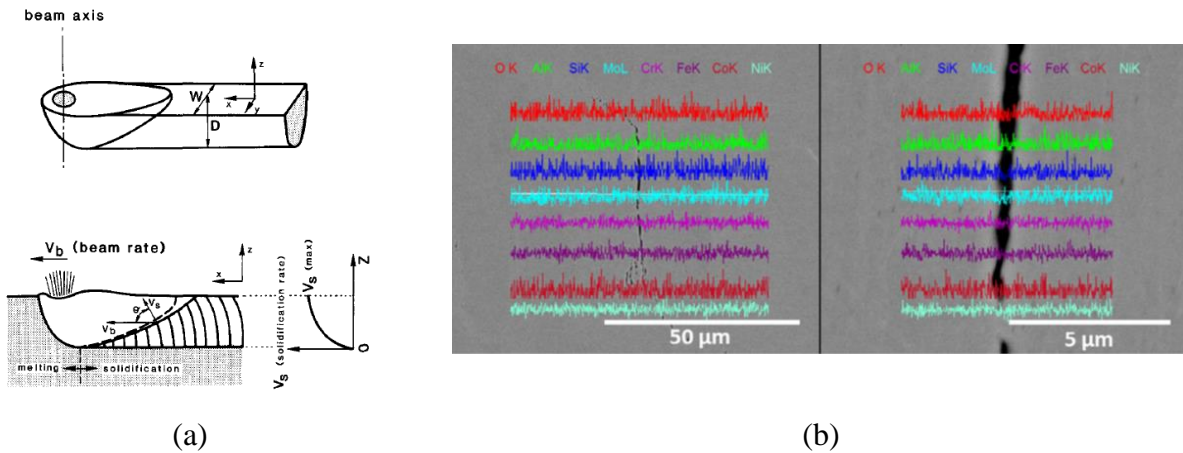
Figure 13 (a) The relation between beam velocity and solidification velocity [35], (b) EDS analysis around the cracks to study the segregation [36]

The other feature of the solidification microstructure of the LPBF process is competitive growth [34]. It should be noted that due the similar packing density of the {100} planes of the FCC microstructure with the melt packing density, these planes would have higher accommodation factor [38] and the solidification speed for <100> direction which is perpendicular to {100} planes is higher in comparison to the other crystallographic directions and it is considered as easy growth direction [39]. There are three [100] directions in the unit cell of the FCC structure and due to their relative direction with respect to the heat flow direction one mode would be activated in growing grain. Grains which are more aligned with the heat flow direction will grow faster and will block the grains which their easy growth direction is less aligned with the heat flow [40]. In Figure 14a grain number 3 is blocked by grain number 2. Due to change in the curvature of the melt pool

different solidification modes maybe be activated from one single grain beneath the melt pool (Figure 14b).

(a)   (b)
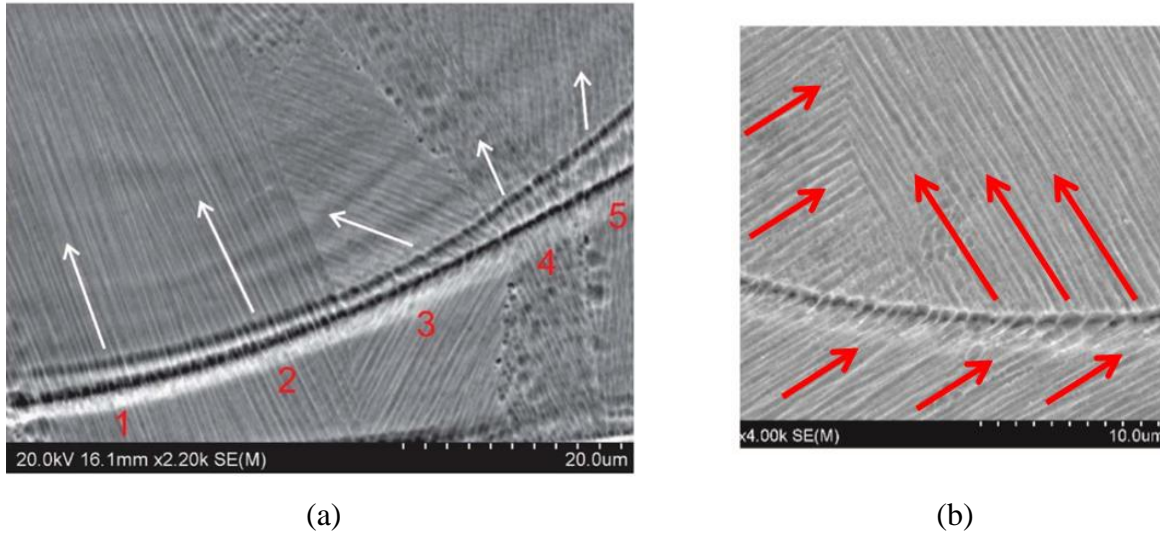
Figure 14 (a) Competitive growth and blocking by adjacent fast moving grains, (b) Activation of different modes from one single grain [34]

Due to the building condition and lack of possibility to online monitoring of the melt pool in LPBF because of the surrounding powders and build chamber space limitation temperature profile, heating and cooling cycles were estimated by simulations. Complex physical phenomena such as high thermal cycles, melt hydrodynamics, evaporation and powder melt pool interaction force the researchers to simplify the real condition for their models, therefore the results of the simulations do not show the practical conditions and can be used as primary approximations. There two approaches to calculate the cooling rate during solidification based on cell size. Theoretical approach which is based on the work of Kurz and Fisher is relating the cell size to the temperature gradient and solidification velocity by the Equation 1 [34]:

$$\lambda_1 = 4.3 \left(\frac{\Delta T_0 . D_L . \Gamma}{k} \right)^{0.25} . R^{-0.25} . G^{-0.5} \qquad \text{Equation 1}$$

Where λ_1 is primary arm spacing or cell size and $\Delta T_0, D_L, \Gamma$ and k are solidification range, liquid diffusion coefficient, Gibbs-Thomson coefficient and partition ratio respectively. G and R as defined previously are thermal gradient in front of solidification front and solidification velocity respectively and thereby cooling rate can be calculated as $\dot{T} = G \times R$ and R is related to the laser

scanning velocity. In the empirical approach the cooling rate and cell size are related with Equation 2 [34]:

$$\lambda_1 = c\dot{T}^n$$

Where c and n are materials constants. Darvish et al. [34] have calculated the temperature gradient and cooling rates based on the available literature for LPBF process as shown in Table 2. As shown the calculated values are in the range of $10^7 K/m$ for G and $10^6 K/s$ for cooling rate. These high cooling rates which are not observed in conventional manufacturing processes [18] are the main reason for specific fine cellular microstructure of the as-built printed parts. It should be mentioned that the solidification mode is determined by the ratio of temperature gradient (G) and growth rate (R) or G/R, and the size of the solidification structures (cells or dendrites) is a function of the cooling rate (G×R).

Table 2 Maximum temperature gradient and cooling rate values for various published work of LPBF. Note: np stands for "not provided" [34]

Material	Method	G, 10^7 K/m	$\dot{T}$, 10^6 K/s	Reference
Inconel 718	Simulation	0.8–1.8	0.7–0.9	Lee & Zhang et al. [14]
Ni-4%Nb alloy	Simulation	0.6–2.2	–	Keller et al. [12]
316L stainless steel	Measured $\lambda_1 = 80\dot{T}^{-0.33}$	np	0.2–4.8	Sun et al. [17]
Ni alloy	Measured $\lambda_1 = 97\dot{T}^{-0.36}$	np	0.2–0.4	Harrison et al. [31]
Ni CM247LC	Measured $\lambda_1 = 97\dot{T}^{-0.36}$	np	0.9	Wang et al. [15]
Inconel 625	Measured $\lambda_1 = 50\dot{T}^{-0.33}$	np	0.1–15	Li et al. [11]
AlSi10Mg	Measured $\lambda_1 = 43\dot{T}^{-0.32}$	np	0.3–16	Tang et al. [24]
Co-29Cr-6Mo	Measured $\lambda_1 = \frac{1.6 \times 10^{-3}}{R^{0.25}G^{0.5}}$	1.8	2.2	This work

2.3.2 Grain Morphology

Grain structure of metallic parts affects mechanical properties. Grains' sizes and morphology could be responsible for anisotropic behaviour. Due to the similar packing density of the {100} planes of the FCC microstructure with the melt packing density, these planes would have higher

accommodation factor [38]. Hence, the solidification speed for <100> direction which is perpendicular to {100} planes is higher in comparison to the other crystallographic directions and it is considered as easy growth direction [39]. Directional heat flow and epitaxial growth in easy growth directions in FCC crystal structures will result in columnar elongated grains parallel to the build direction. It should be noted that each grain consists of fine cellular structures inside it and the cell size are in the submicron range but the average grain size is 150 µm in length and 20 µm in width [23]. Elongated columnar grains are visible in the parallel cross section and they are highly oriented and textured but in the transverse cross section as is obvious in the pole figure the texture is more diffused (Figure 15b).
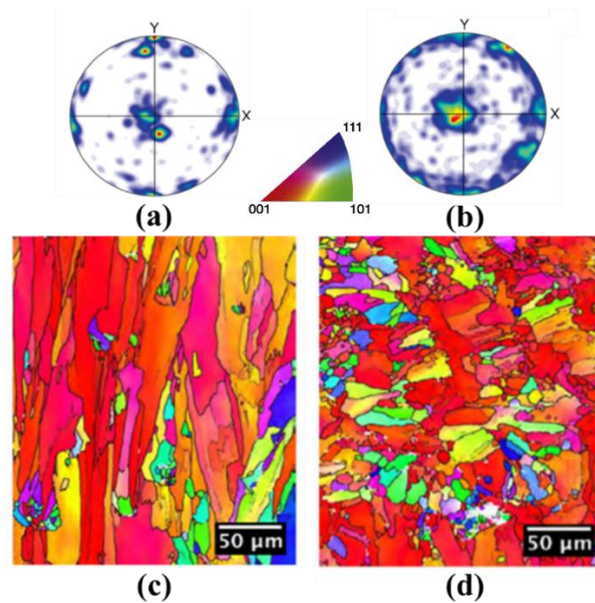
Figure 15 (a) and (b) {001} pole figures in the longitudinal and transverse cross sections respectively, (c) and (d) EBSD maps for longitudinal and transverse cross sections respectively for CM247LC in the as-built condition [22]

TEM bright field images of the both transverse and parallel cross sections of the printed parts show a high dislocation density in the as-built samples (Figure 16). Dislocations are more populated in the cell walls and the center of the cells contains fewer numbers of dislocations.
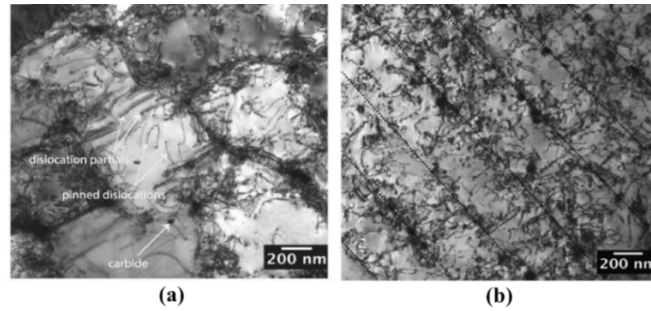
Figure 16 TEM bright field image of (a) Transverse, (b) Longitudinal cross sections [22]

There are two different explanations for this high dislocation density. As described by Diviya et al. [22] the high dislocation density in the as-built condition is due to the misorientation between the cells and these dislocations are formed to match this difference in orientation of the adjacent cells. Diffraction pattern of a selected area indicate double spots which are from adjacent cells and the misorientation between them is calculated to be $7°$, which is less than the grain boundaries misorientation. Both cell walls and grain boundaries contain large number of dislocations and to differentiate between them the best way is using spot patterns. As shown in Figure 17a the spot pattern between the adjacent cells shows double spots but the spot pattern on the two adjacent grains does not contain this feature and the misorientation between them is much bigger than that of adjacent cells (Figure 17b). Finer scale EBSD map of a grain in transverse cross section (Figure 17c) shows gradual change in grain orientation from one boundary to another. Therefore, the cells within a grain should have slightly different orientation to accommodate the overall grain orientation change and to solve this change in adjacent cells orientations dislocations should be present in the cell walls.

(a)   (b)

(c)
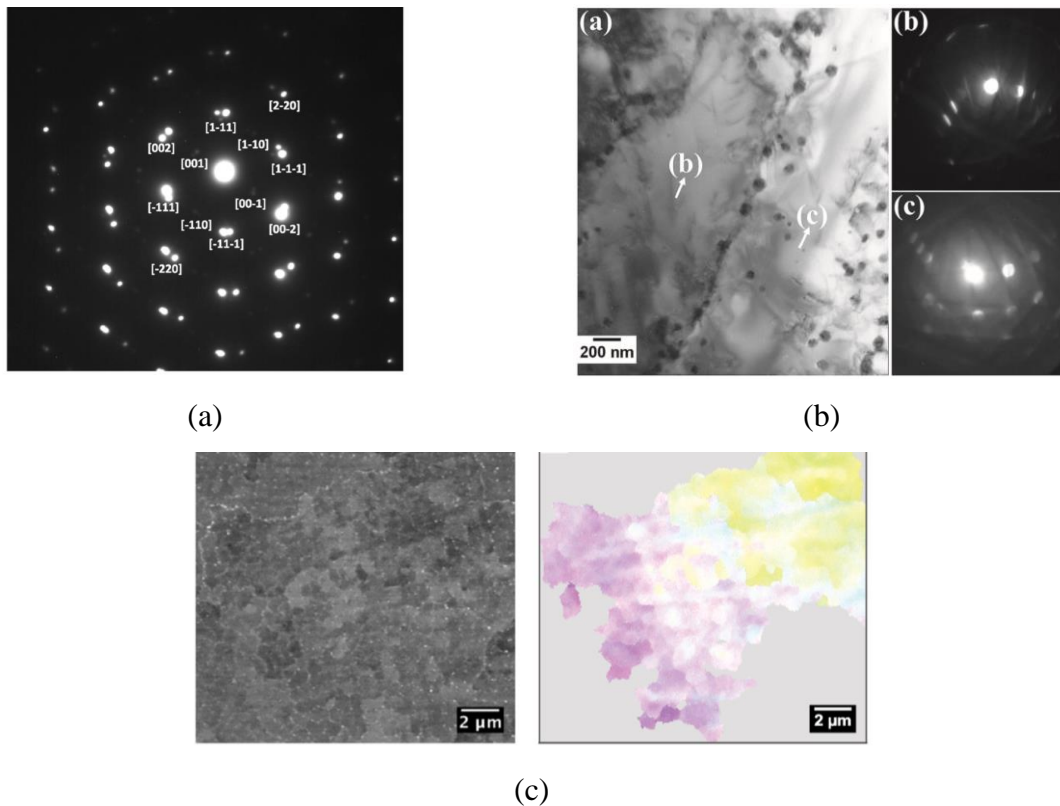
Figure 17 (a) Spot patterns showing low misorientation between adjacent cells [22], (b) Spot patterns of two adjacent grains [41] and (c) The gradual change in cell orientations inside a grain in transverse cross sections [22]

In the second approach Wang et al. [41] believe that the high dislocation density at cell walls is due to the presence of the second phases at cell walls which make barrier for dislocation motion. TEM EDS maps of alloying elements distribution are shown in Figure 18 [41]. Obviously, at cell walls there are some regions with concentrated amount of specific elements such as Hf, Ti and C. Presence of these elements shows micro segregation at cell walls during solidification which were not detected by EDS in SEM which is related to smaller interaction volume in TEM in comparison to SEM due to sample thickness. It should be noted that distribution of segregated elements is diffused even inside the cells with lower concentration which means that solute trapping has occurred in some extent during solidification which is related to the fast moving solidification front due to high cooling rates and large temperature gradient inside melt pool.
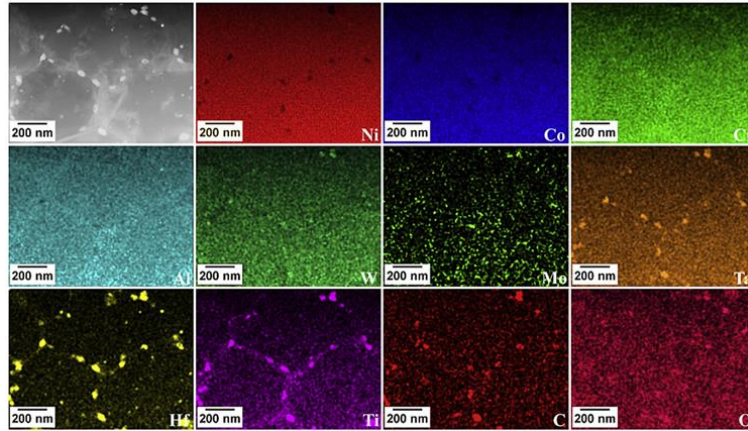
(a)
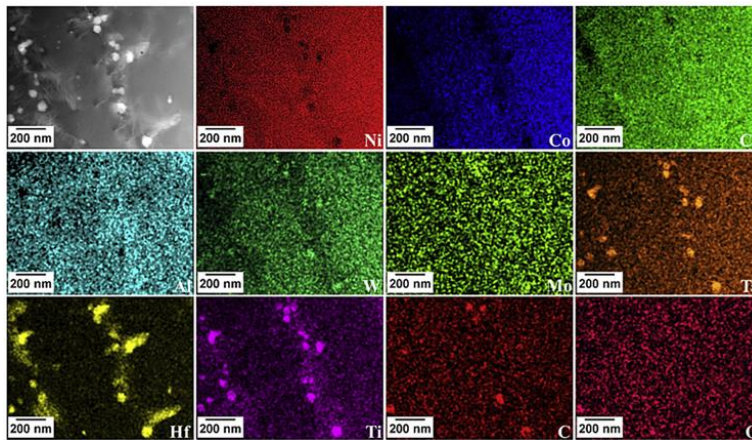
(b)

Figure 18 TEM EDS elemental map for CM247LC in (a) Transverse and (b) Longitudinal cross sections [41]

Highly localized heat source and high cooling rates will cause a considerable amount of residual stress in the as-built condition. This high residual stress could cause localized plastic strains, distortion and cracking which are common in LPBF produced parts. TEM images show pair dislocations in the as-built condition (as arrowed in Figure 19b) the main reason for the presence of the pair dislocations is dislocation movement in an ordered structure.
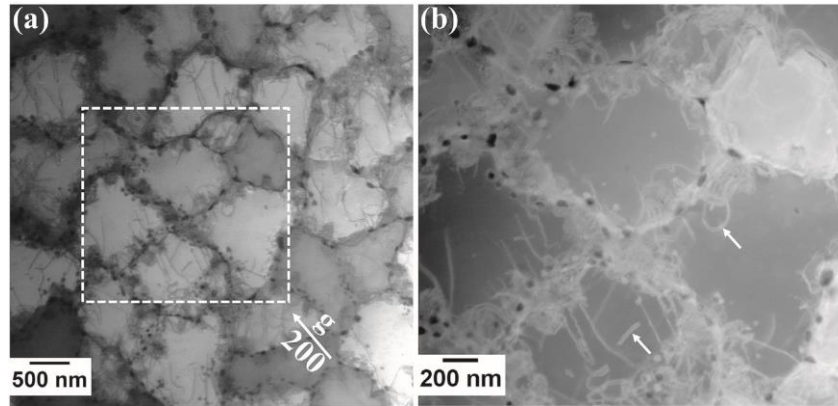
Figure 19 (a) Dislocation structure of the CM247LC in the as-built condition and (b) arrowed pair dislocations [41]

TEM images of the as-built CM247LC shows fine precipitates in Figure 20. Bimodal precipitate distribution is observed inside the cells the precipitates are finer in the order of 5 nm and at cell walls they are bigger in the order of 50 nm. Larger precipitate at cell walls could be related to the higher amount of precipitate former elements like Ti at cell walls and higher amount of dislocations at the cell walls which act as high diffusivity paths [42] and make the diffusion more easily. Pair dislocations are indication of dislocation movement in solid state due to residual stresses and higher amount of dislocations at the cell walls are related to the dislocation barriers such as carbides and larger precipitates at the cell walls.
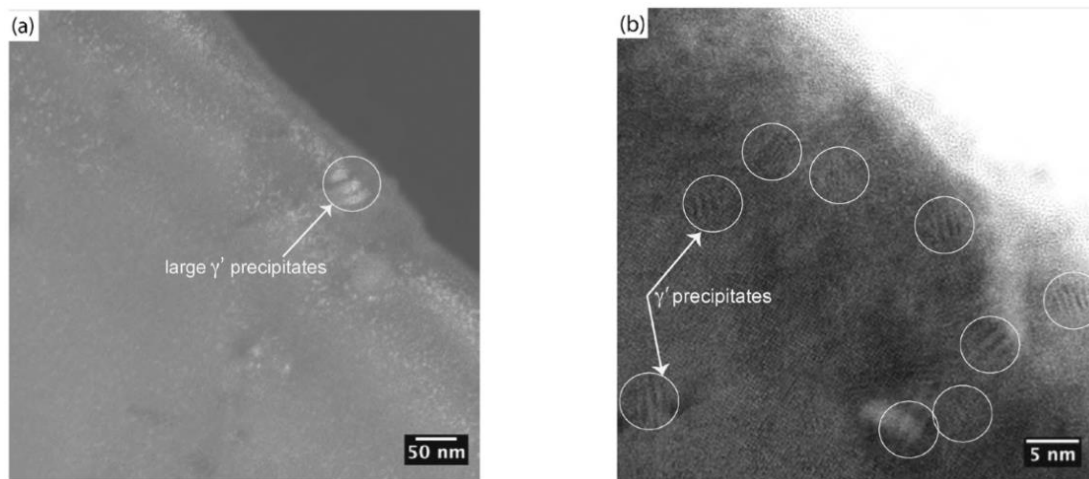
Figure 20 Bimodal distribution of the precipitates in the as-built condition of CM247LC (a) Larger precipitates at cell walls and (b) smaller preciptates inside the cells [22]

It seems that both approaches are correct and they can explain the dislocation distribution based on the alloy chemistry. Each of them which have been resulted to the same dislocation structures

and distribution are responsible for part of this high dislocation density. It should be considered that these explanations will depend on the alloy chemistry and the effect and portion of each mechanism would be related to the chemical composition of the alloy.

2.4   Mechanical Properties of LPBF Samples

2.4.1   Quasi-Static Response of LPBF Samples

Performance of the AM parts under mechanical loads is of the most important criterion which must be met before utilizing these parts in real application. Figure 21 shows the yield strength, UTS and ductility of the as-built condition, cast and heat treated and LPBFed and heat treated for CM247LC [41]. The strength of the as-built samples is in same range of cast and heat treated specimens. It should be noted that the high strength of the cast sample after heat treatment is due to uniform distribution of precipitates with suitable size but due to their small size (less than 50 nm) the precipitates in the as-built condition could not be considered as the main contributor to high as-built strength. As mentioned previously there are two features in the as-built condition which could be considered as the main reasons for high as-built strength.
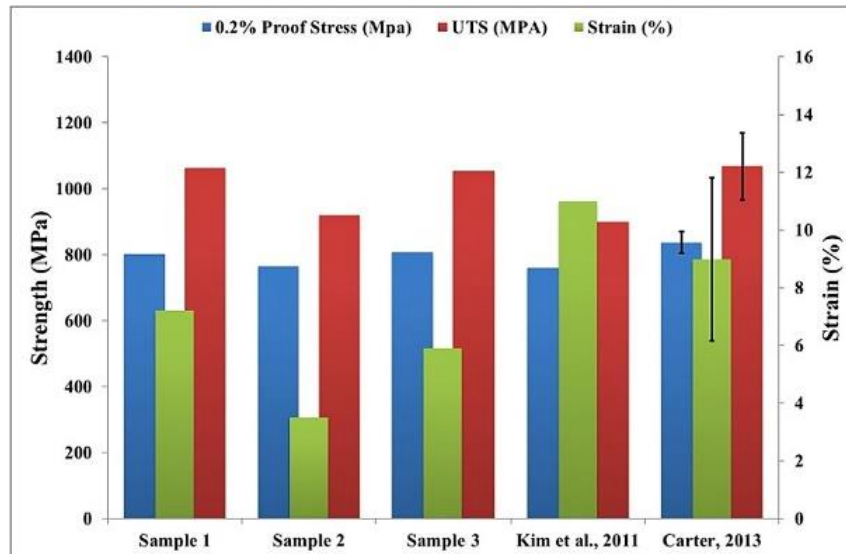

Figure 21 As-built mechanical properties in comparison to the cast and HIP samples for CM247LC. Note: Samples 1, sample2 and sample 3 are 3 as-built samples [41]

Firstly, high dislocation density of the as-built condition and fine cellular structure could increase the strength of the printed parts. Secondly, in the as-built condition, significant amount of

supersaturated alloying elements is present in the matrix; strengthen the alloy by solid solution strengthening.

The difference in mechanical properties of the vertical and horizontal samples has been shown in Figure 22a. Figure 22b shows the fracture surface of HX samples in different conditions. For vertically built samples the elongated grains are parallel to the loading directions and grains have deformed uniformly and finally necking has separated the grains and it seems that individual grains have necked and inside the grains the fracture surface is covered with dimples which are signs of ductile fracture. On the other hand, for horizontally built samples grains boundaries are perpendicular to the loading direction and the fracture surface shows cleavage surfaces inside grains and grain boundaries are visible in the SEM micrograph [17].
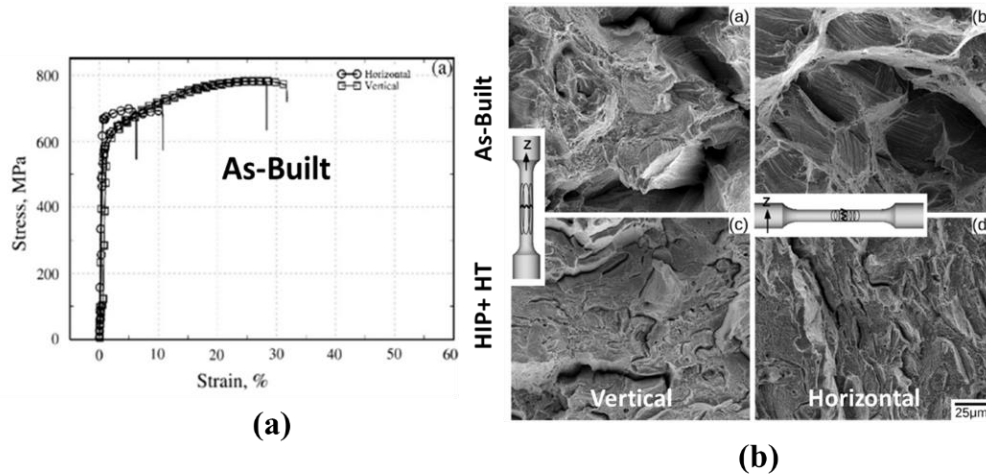
Figure 22 Fracture surface of HX samples in different conditions [17]

2.4.2 Fatigue Response of LPBF Parts

Fatigue is the main reason for 90% of service failures due to mechanical causes [43]. Although the quasi-static response of LPBFed samples is superior to the conventionally manufactured ones due to the specific microstructural features, their performance under cyclic loading suffers form the inherent characteristics of the production method. Poor surface finish and as-manufactured defects are the main weak points of the samples produced by LPBF [14]. Due to presence of small porosities and defects the AM samples generally do not show fatigue limit and by increasing the life the stress will decrease as well and a plateau is not present in the stress-life curve (Figure 23).

25

Figure 23 Fatigue response of AM Ti-64 samples in comparison with the conventional samples [14]

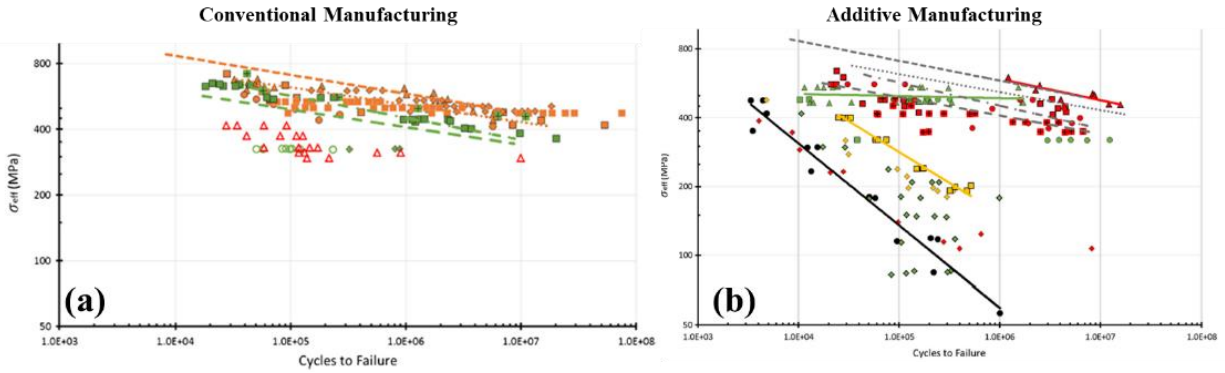It has been shown that there is a direct correlation between the surface roughness and the fatigue life of samples. Particles adhesion from the adjacent powder bed is the main reason for poor surface finish for the side walls of the samples [44]. Due to larger powder size and layer thickness which are used for EBM process the surface roughness of the EBM samples are higher than the LPBF samples and these rough surfaces is related to the higher stress concentration factor near the surface and will lead to lower fatigue life (Figure 24). Further, post surface treatments such as EDM, electro-polishing and shot peening has been shown to be effective ways for improving the fatigue performance of the AM samples [45].
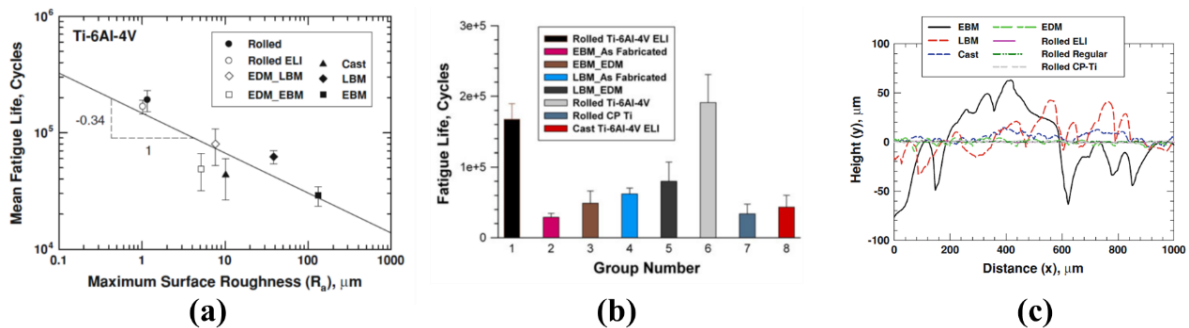
Figure 24 Effect of surface roughness and surface treatments on the fatigue life (a) showing the decrease in fatigue life by increasing the surface roughness, (b) worse performance of AM samples in comparison to cast and forged samples and (c) surface roughness profile of different manufacturing routes [45]

There would be out of access surfaces in the complex parts, which will make the post surface treatments more difficult. This will include cooling channels of the blades for example (Figure 25a). In this conditions testing the as-built surface finish of the samples under cyclic loading would be helpful for understanding their performance under this situation [46].

Figure 25 (a) Parts with internal channels and (b) Samples with different surface finish [46]

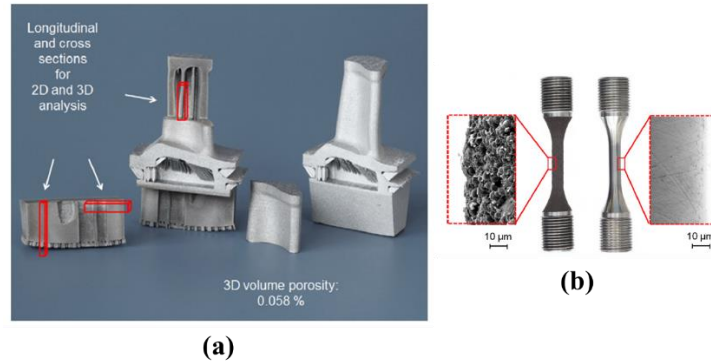Shot peening is able to induce compressive residual stress and fine deformed microstructure near the surface in addition to reducing the surface roughness which are important for fatigue performance [47]. Moreover, the deformation induced phase transformation results in conversion of retained austenite in the as-built condition of the 17-4 PH stainless steel to martensite and increase the strength of the materials near the surface which is the most important region of the part for fatigue analysis (Figure 26b).
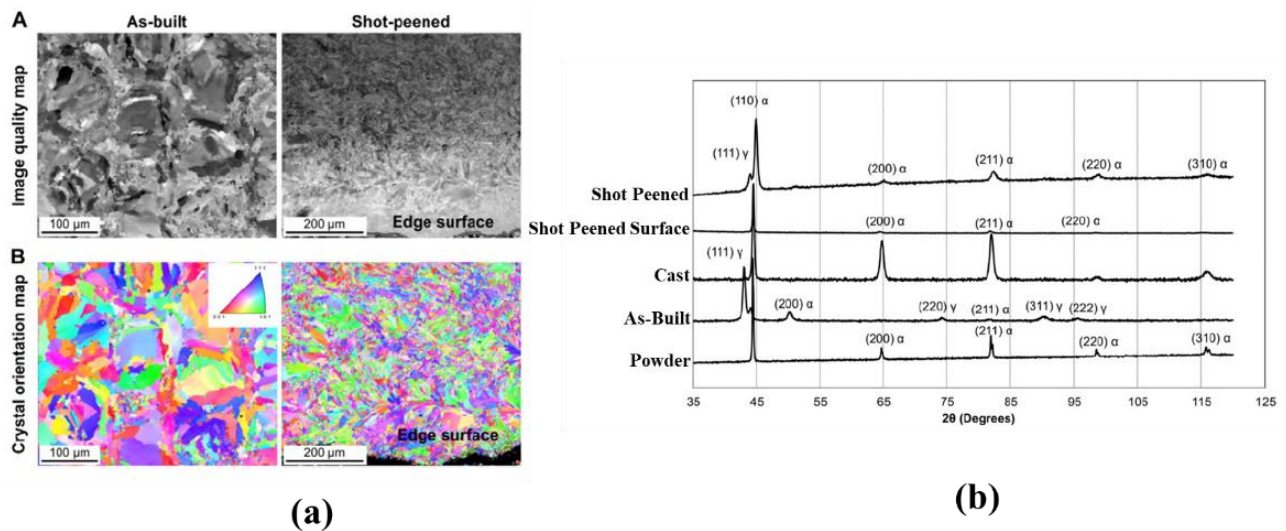
Figure 26 (a) Deformed microstructure near the surface of shot peened samples and (b) XRD patterns from different conditions [47]

Defects such as gas porosities and lack of fusions (LoF) will act as stress risers and are the main crack initiation sites on the fracture surface [15]. The best way for reducing this type of defects is optimizing the process parameters to obtain a nearly full dense part. Due to their irregular shapes LoF would reduce the fatigue response more than the spherical gas porosities [15]. As shown in

Figure 27a hot isostatic pressing (HIP) has been shown to be an effective way for closing the pores and increasing the fatigue life [48]. The effect of HIP depends on materials as well. It has been shown that HIP would increase the endurance limit in high cycle fatigue (HCF) regime for both ductile and brittle alloys. In the low cycle fatigue (LCF) regime HIP would be useful for brittle materials (Figure 27b), but for ductile alloys such as SS 316 HIP would reduce the fatigue response by decreasing the tensile properties (Figure 27c) [49].
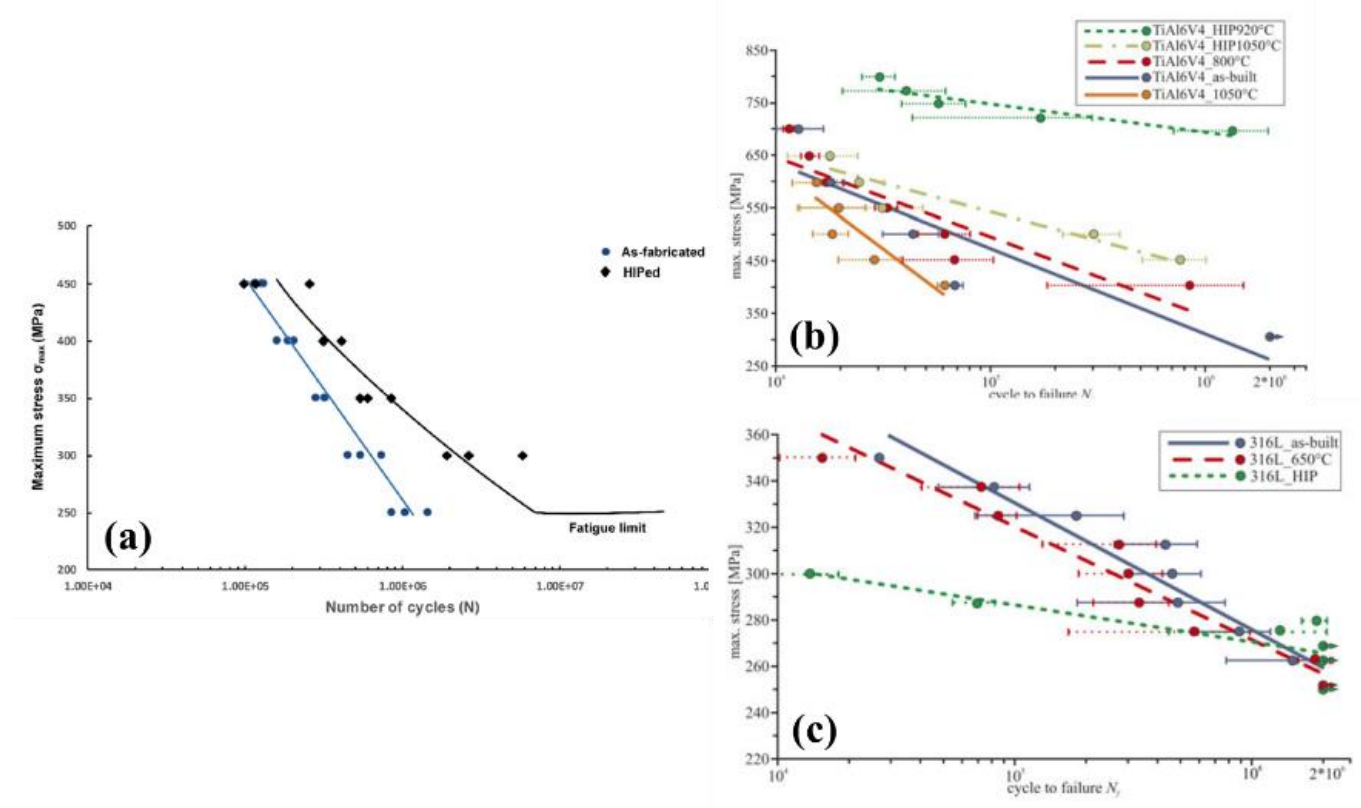

Figure 27 Effect of HIP [48] on (a) HX, (b) Ti64 and (c) SS 316 [49]

High thermal gradients during manufacturing induces high residual stresses in the part. It has been shown that residual stress would increase the fatigue crack growth (FCG) rates in the Ti64 (Figure 28a) but it does not change the FCG rates in the SS 316 samples (Figure 28b) [50,51].
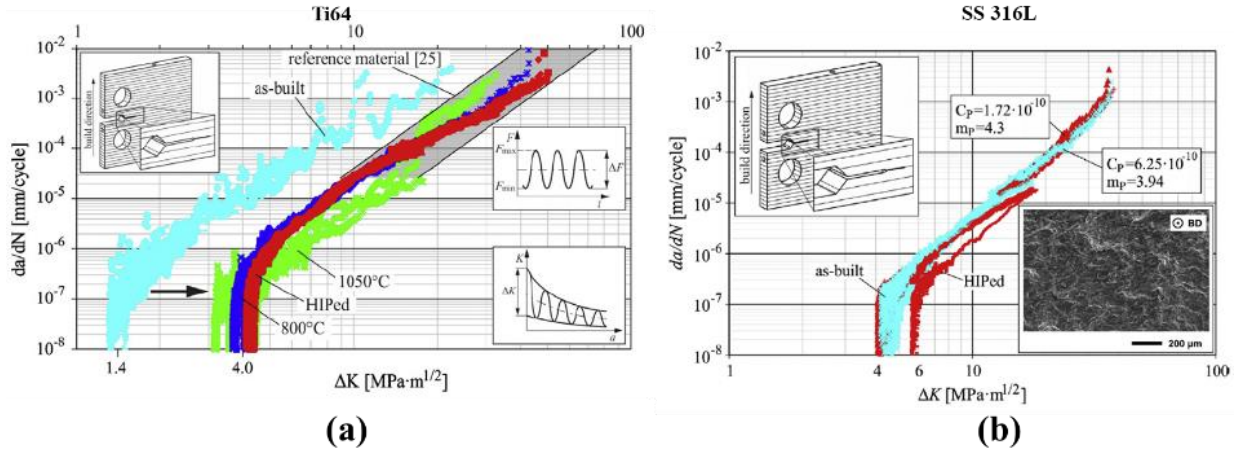
Figure 28 Effect of residual stress on FCG behaviour of (a) Ti64 [50] and (b) SS 316 [51]

2.4.2.1 Fatigue Modelling

The mentioned findings were phenomenological aspects of analysing the fatigue experiments, fatigue life prediction is an important part of these experiments. The successful design of load-bearing components necessitates developing a fatigue model that can predict the life accurately. The main basic fatigue modelling approaches include: stress- strain and energy-based and fracture mechanics. The stress approach is based on Basquin's relation who first observed that stress-life (S-N) could be linearly related on a log-log scale (Equation 3).

$$\frac{\Delta\sigma}{2} = \sigma_f'(2N_f)^b$$
Equation 3

Where $\frac{\Delta\sigma}{2}$ is true stress amplitude, $2N_f$ is reversals to failure, σ_f' is fatigue strength coefficient and b is fatigue strength exponent or Basquin's exponent. Strain base fatigue models are based on materials response at the hot spots which are important for fatigue life predictions, a very common method is the Coffin-Manson-Basquin [52] relationship, by assuming that the total strain amplitude is the sum of the elastic and plastic strain (Equation 4):

$$\frac{\Delta\varepsilon}{2} = \frac{\Delta\varepsilon_e}{2} + \frac{\Delta\varepsilon_p}{2}$$
Equation 4

And writing the elastic using Hooke's law and replacing the stress amplitude by the Basquin's relation:

$$\frac{\Delta\varepsilon_e}{2} = \frac{\Delta\sigma}{2E} = \frac{\sigma_f'}{2E}(2N_f)^b$$
Equation 5

29

Coffin and Manson in 1950s independently found that plastic strain-life ($\varepsilon_p - N$) data can be linearized in log-log coordinates as well. Hence, the plastic strain can be related to the life by power law function:

$$\frac{\Delta\varepsilon_p}{2} = \varepsilon_f'(2N_f)^c \qquad\qquad \text{Equation 6}$$

Where $\frac{\Delta\varepsilon_p}{2}$ is plastic strain amplitude, $2N_f$ is reversals to failure, ε_f' is fatigue ductility coefficient and c is fatigue ductility exponent. Now the total strain can be related to the life by substituting the elastic and plastic strain amplitudes form Basquin and Coffin-Manson relations as shown in Equation 7:

$$\frac{\Delta\varepsilon}{2} = \frac{\Delta\varepsilon_e}{2} + \frac{\Delta\varepsilon_p}{2} = \frac{\sigma_f'}{E}(2N_f)^b + \varepsilon_f'(2N_f)^c \qquad\qquad \text{Equation 7}$$

In which the $\sigma_f', b, \varepsilon_f', c$ are the fatigue properties of the material. This Equation is termed as the strain-life relation or Coffin-Manson-Basquin relation. At short lives or high strain amplitudes, plastic strain is predominant, while at longer lives and lower strain amplitude, elastic strain is the leading component. Figure 29a illustrates the strain-life approach graphically.
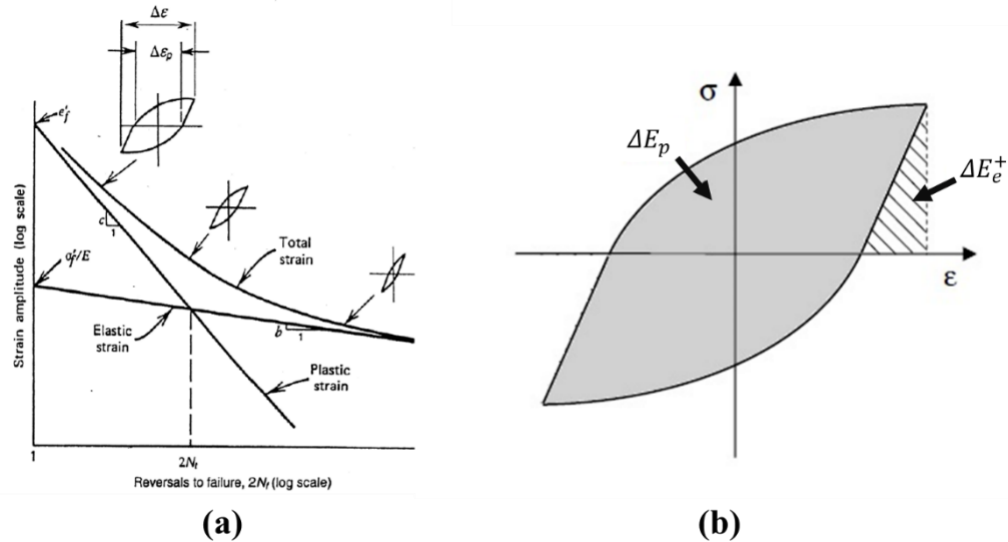

Figure 29 (a) Strain-Life curve showing total, elastic, and plastic strains [53] and (b) Hysteresis and elastic and plastic strain energies [54]

30

Energy-based approach considers the dissipated energy in each cycle for fatigue life perdiction which is a combination of stresses and strains. On microscopic level, irreversible nature of the micro-plastic deformation caused by each cycle of loading is associated with the dissipation of strain energy [53]. The Jahed-Varvani (JV) model [54,55] is a more recent energy-based fatigue life model. It is analogous to Coffin-Manson as it has the same mathematical form as well as a distinction between the elastic and plastic components. The total strain energy density can be defined as:

$$\Delta E_t = \Delta E_e^+ + \Delta E_p \qquad \text{Equation 8}$$

Where ΔE_e^+ and ΔE_p are the positive elastic and plastic energy densities associated with the stable hysteresis loop, respectively (Figure 29b). The elastic component of the equation (fatigue strength) comes from the relation between the positive elastic energy, calculated from maximum stress and elastic modulus, and number of reversals.

$$\Delta E_e^+ = \int \sigma d\varepsilon_e = \frac{1}{2} \sigma_{max} \Delta \varepsilon_e = \frac{\sigma_{max}^2}{2E} \qquad \text{Equation 9}$$

The plastic component of the equation (fatigue toughness) comes from the relation between the plastic strain energy, which is equal to the area within the hysteresis loop (the gray area in Figure 29b), and number of reversals.

$$\Delta E_p = \oint \sigma d\varepsilon_p \qquad \text{Equation 10}$$

The plastic strain energy density per cycle ΔE_p has the advantage of being almost constant during the life under strain-controlled conditions [53]. According to JV formulation the total strain energy density is related to the fatigue life by the following relationship:

$$\Delta E_t = E_e'(2N_f)^B + E_f'(2N_f)^C \qquad \text{Equation 11}$$

Where the E_e' and B are the fatigue strength coefficient and exponent respectively and are found by the best fit of the elastic energy of the experimental data, Moreover, E_f' and C are the fatigue toughness coefficient and exponent respectively are found based on the best fit for the plastic energy and life curve of the experimental data.

In fracture mechanics the stress intensity factor which is a function of stress and crack/defect length would be considered as the damage parameter and its value can be related to the crack growth rate or fatigue life [53]. This research is focused on the strain- and energy-based approaches.

Different modelling approaches has been used for additively manufactured parts and due to different crack initiation from the surface or process induced defects a general framework has not been stablished yet in the literature. Most of the published studies has performed stress-controlled experiments and made a comparison between the as-manufactured and HIPed or surface treated samples. Basquin's parameters has been evaluated for these conditions but the stress-based approach is limited to HCF range and full fatigue properties would not be captured in such experiments.
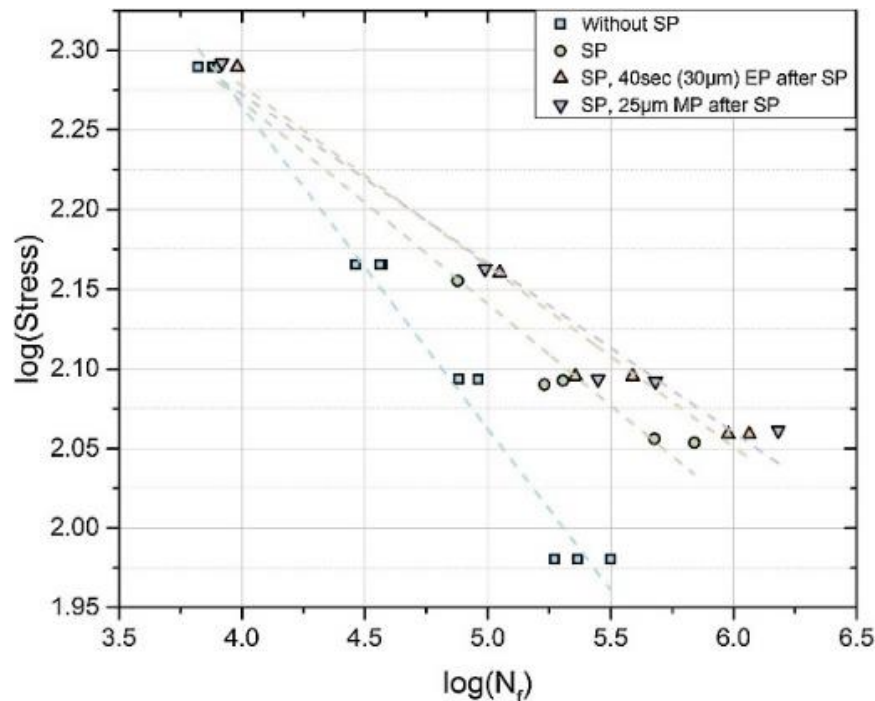

Figure 30 Effect of post treatments (shot peening) on Basquin's curves for AlSi10Mg showing decrease in slope after shot peening (SP) which indicates the fatigue performance improvement [56]

As shown in Figure 30 shot peening has reduced the slope or fatigue strength exponent of AlSi10Mg which indicates improvement of fatigue performance. The inherent drawback of the stress-based approaches is that they can not be used for the LCF region because of introduction of plasticity and uncertainty with the definition stress in this region.

To overcome the aforementioned problem associated with the stress-based models, strain-based modelling has been used for SS 17-4 LPBFed samples [15]. It has been seen that plastic strains are orders-of-magnitude smaller than elastic strains for both as-built and heat treated conditions – independent of building orientation; hence, even at high strain amplitudes, the total strain–life curves follow the elastic strain–life curves (Figure 31). Due to presence of defects and low ductility of the samples this conclusion seems reasonable but can not be generalized to all AMed materials.

Vertical AB

$$\varepsilon_a = 0.011(2N_f)^{-0.15} + 1.8(2N_f)^{-0.53}$$

Vertical HT

$$\varepsilon_a = 0.037(2N_f)^{-0.26} + 3.4(2N_f)^{-0.6}$$

Horizontal AB

$$\varepsilon_a = 0.011(2N_f)^{-0.13} + 2.7(2N_f)^{-0.54}$$

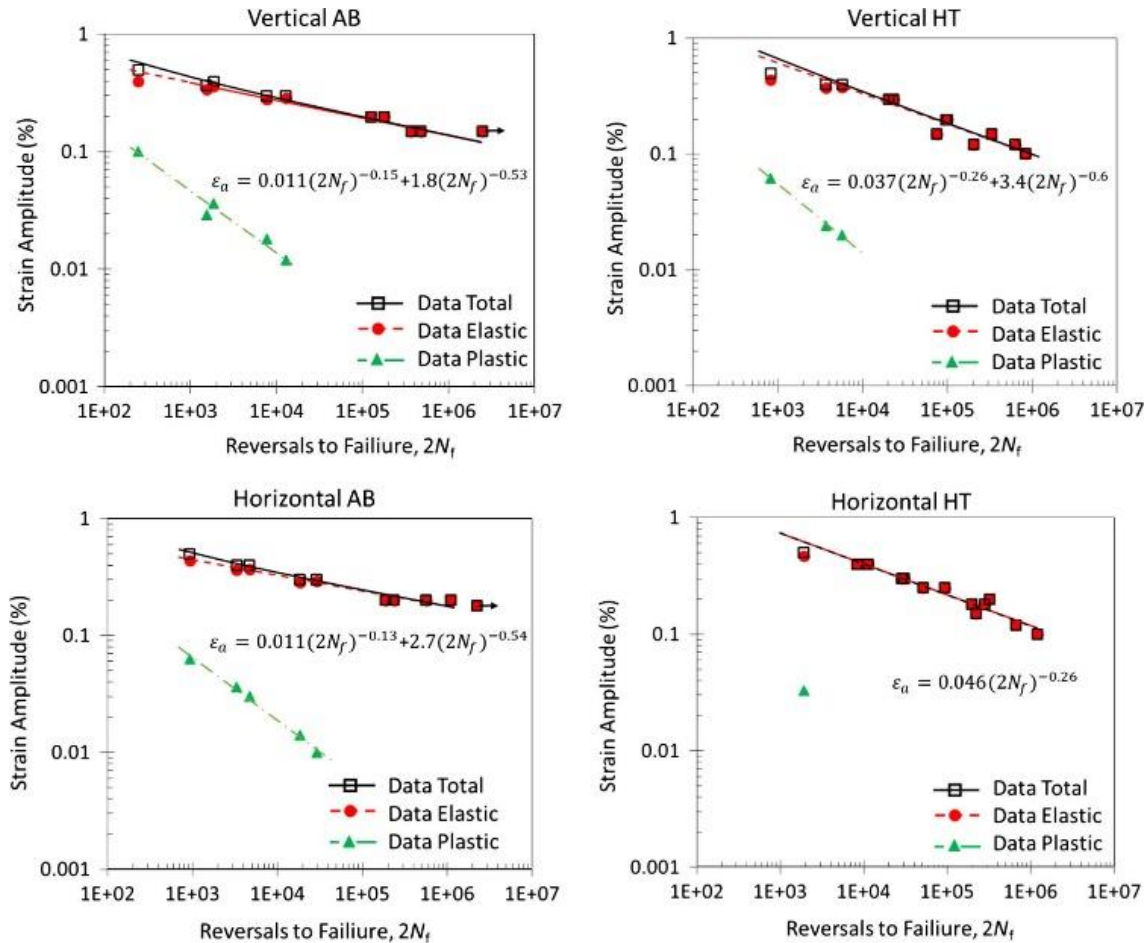**Horizontal HT**

$$\varepsilon_a = 0.046(2N_f)^{-0.26}$$

Figure 31 Strain–life curves including elastic, plastic and total strain amplitudes of LPBF 17-4 PH SS in different conditions [15]

Because of the presence of defects a specific type of fracture mechanics approach (Murakami's method), which considers the effect of applied stress and size of defects has been used for Ti64 [57]. In this type of modelling fatigue life is related to the stress intensity factor which is defined as:

$$\Delta K = C \times \Delta\sigma \sqrt{\pi\sqrt{area}}$$ Equation 12

where ΔK is the stress intensity factor (SIF) range, Δσ the applied stress range, $\sqrt{area}$ the square root of the projected area of the pore, and parameter C is 0.5 for internal defects and 0.65 for surface defects [57].
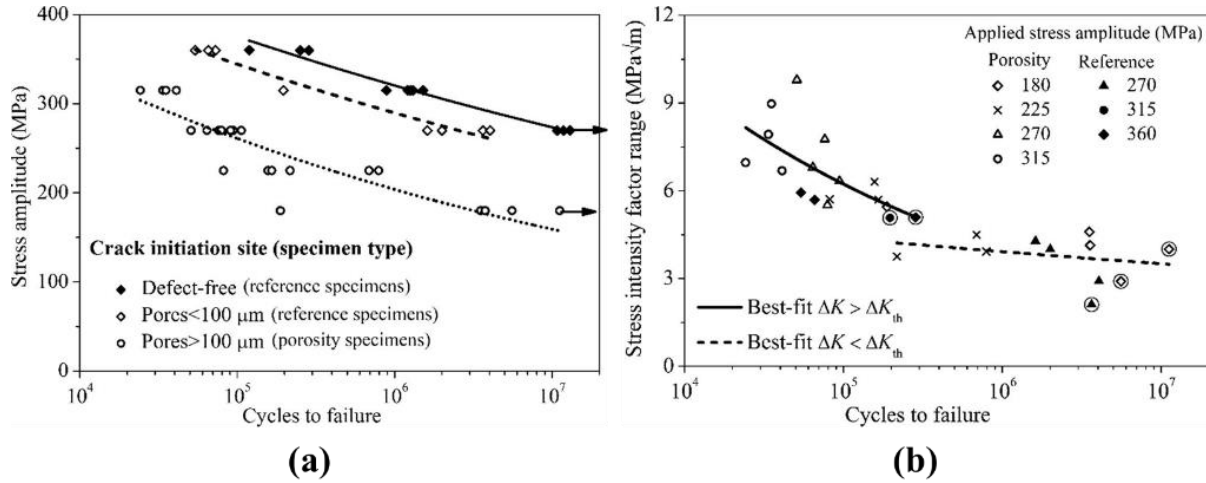

Figure 32 Comparison of the Basquin's (a) and Murakami's (b) methods for Ti64 [57].

For the Basquin's stress-based modelling different curves are needed for different combinations of the stress and porosities, as shown in Figure 32a, but for the Murakami's method one curve would describe the fatigue behaviour by combining the stress and sizes of defects in one parameter. Although the Murakami's approach can predict the fatigue life better in this case but optimising the AM process parameters to produce full dense parts would be the prior step and finding the $\sqrt{area}$ needs advancedimaging techniques such as computed tomography (CT) which are not widely available in the routine fatigue lab equipment.

Based on the published studies, energy based models such as JV has not been yet widely used for AM samples and comparison between the accuracy of different models has not been considered yet. One of the objectives of the proposed research is to study and compare the energy- and strain-based fatigue modelling approaches for the additively manufactured Hastelloy X.

2.5 Summary

The fast development and industry's interest in using AM as an alternative manufacturing process prevented a detailed characterization of AM and specifically LPBF parts. In addition to lack of a detailed optimization of manufacturing conditions of LPBF-HX parts, the mechanical responses of optimized parts under quasi-static and cyclic loading need a delicate attention, which is crucially helpful later in applying the proper prediction models for life estimation. The ultimate goal of this research is to identify the role of additive manufacturing process parameters on the mechanical performance of the samples. After optimizing the parts location, laser scanning speed as an important process parameter has been selected for such a goal. The effect of laser scanning speed on the quasi-static response will be evaluated first. An optimum processing window would be determined for the minimum porosity population or maximum density and maximum tensile strength. Samples within the optimum window will be printed for evaluating the fatigue performance. Based on the published studies, energy-based models such as JV has not been used for AM samples and comparison between the accuracy of different models has not been considered yet. A comparative study will be performed on the energy- and strain-based fatigue modelling approaches for the additively manufactured Hastelloy X.

Chapter 3

3 On the Effect of Spatter Particles Distribution on the Quality of Hastelloy X Parts Made by Laser Powder-Bed Fusion Additive Manufacturing

3.1 Introduction

Producing complex geometries [1,2], multi-material/functionally graded materials and composites [3–7,58] are some of the benefits of Additive Manufacturing (AM) over traditional manufacturing techniques. Among different AM methods for metallic materials, laser powder-bed fusion (LPBF) has become more common in industry while being used to produce functional parts [9–11]. In LPBF, a thin layer of powder is spread over the work area followed by the laser irradiation on the selected area to melt particles based on a sliced CAD model.

Repeatability is one of the main concerns for additively manufactured parts due to changes in powder-bed compaction density, effective layer thickness etc.[59–61]. LPBF-made parts may not be replicated with the same process parameters due to the randomly distributed defects [62,63] formed during the process. These defects are formed mainly due to the disturbances stemmed from variability in the powder distribution, non-identical laser intensity across the bed, etc. causing anisotropic properties in mechanical behaviour [50] and roughness [64] of the produced parts. Mechanical strengths of LPBF-made parts can be related to the density and surface roughness. Density is a direct measure of porosity while surface roughness plays an important role in the fatigue life [14]. Mumtaz et al. [64] found that reducing the scanning speed reduces the top surface roughness but increases the side surface roughness of Inconel 625. In another study, Abele et al. [65] showed that the contour track can reduce the roughness significantly thus it should be done after printing the core of the part to avoid collision with recoater in the following recoating step and other factors such as part distortion should be considered as well. Wang et al. [66] also studied surface roughness and have concluded that the re-melting of surface layers improves the surface finish of LPBF-made samples.

The inherent layer melting of the powder bed during LPBF is considered as the main reason for high side surface roughness in LPBF parts [67,68]. Ejection of large spatters from the melt pool

contaminate the powder bed where they would adhere to the adjacent particles and borders of the melt pool leading to rough side surfaces [69]. Based on the experimental observations of the interaction between the laser beam and metallic powders, formation of metallic vapor in LPBF seems to be inevitable [70]. This vapor formation has different outcomes with different chamber pressures. For a low pressure or vacuum situation, the metallic vapor formation may be beneficial and may reduce particle adhesion because of the denudation of the melt pool from the surrounding powder particles. However, this denudation creates a powder free region near the free surface of the part thus decreasing the side surface roughness [71]. On the other hand, for high chamber pressure, which are common in LPBF, powder particles adjacent to the melt track would be either attracted to the melt pool through direct contact due to capillary forces or ejected due to the impulse applied through the highly circulated convective melt pool. Some of these powder particles adhere to the borders of the current layer of the part cross-section and hence result in an increased side surface roughness in LPBF-made parts [71–73].

The interaction of highly circulated melt pool with the surrounding particles may create forcing impulses pushing the particles to eject from the zone. However, it is claimed in the literature that the presence of vapor pressure is also the main cause of spatter ejection from the melt pool area [74]. According to Ly et al. [70] spatters can be classified into three main categories: melt pool splashes, hot and cold ejections. Melt pool splashes are formed when the elongated necked region of the melt pool thins out enough to overcome the surface tension by its kinetic energy. It should be noted that the main reason for the formation of the elongated necked region is the depression of the melt pool caused by the recoil pressure. Hot and cold ejections are however formed by forcing impulses and when the particles in the induced gas flow reach either the laser irradiating area thus being heated to form hot ejections or just fly in the gas flow to form cold ejections. There is also another by-product of the laser powder interaction which is called "condensate" and is formed due to the condensation of the metallic plume above the melt pool [75]. In this work, all of these ejections from the melt pool are simply called spatters.

Simonelli [76] studied the formation of spatters for different materials and showed that they are different from virgin powders in terms of the surface oxide layer and microstructure. Andani et al. [77] studied the effect of laser power and scanning speed on the spatter formation and showed that it increases by an increase in the laser input energy, i.e., increasing the power and/or reducing the

speed. Moreover, their results indicate that the effect of scanning speed is more prominent than the laser power for spatter generation. Similarly, Anwar and Pham [78,79] have studied the effect of gas flow direction on the spatter distribution in the powder-bed for AlSi10Mg. Their results show that the spatter particles accumulated in the direction of the gas flow and effected the mechanical properties of printed parts.

The literature lacks detailed studies on the effects of spatters on the quality of the printed parts. However, there are several published papers that study the effect of recycled powders on LPBF-made parts [80,81]. As recycled powders contain spatters, they can be used to study the effect of spatter on the LPBF-made samples. In contrast to LPBF parts with virgin (fresh) powder, Liu et al. [82] showed that the use of contaminated (recycled) powders may degrade tensile mechanical properties of AISI 316L. In contradiction, Asgari et al. [83] found that the use of recycled powders does not affect mechanical properties of AlSi10Mg printed specimens. However, they have not considered the surface roughness of LPBF-made parts.

In this paper, a comparative study is conducted on the virgin and spatter powders of Hastelloy X to study the effect of spatter formation on the quality of produced samples. Chemical composition, phases, microstructure, morphology and thermal behaviour of virgin and spatter powders are analyzed followed by the measurement of the surface roughness of the printed parts by non-contact laser profilometry. It was found that the argon gas flow and the recoater motion direction synergistically change the powder distribution and produce a spatter rich region at the end side of the built plate due to accumulated spatters and the parts top surface roughness (S_a) has been increased from 14.4 to 28 µm in this region.

3.2 Experimental Procedure

3.2.1 Process and Materials

In this work, 16 LPBF-made cubic parts (10x15x30 mm) were manufactured using an EOS M290 (EOS GmbH, Krailling, Germany) equipped with an Ytterbium fiber laser (IPG Photonics, Oxford, Massachusetts, USA). Commercially available Hastelloy X powder from EOS with an average powder size of 30 µm and particle size distribution of D10 < 15.5 µm, D50 < 29.3 µm and D90 < 46.4 µm were used to manufacture the LPBF parts. All samples were made with similar processing parameters (laser power of 200 W, laser velocity of 900 mm/s, layer thickness of 0.06 mm and

hatching spacing of 0.08 mm without pre/post exposure) using a rotated stripe scanning strategy. Build plate temperature was maintained at 80˚C during the process. After the process, spatter powders were gathered from around the build plate and above the argon blowers.

3.2.2 Characterization Methods

3.2.2.1 Microstructure and Phase Analysis

A Zeiss ULTRA plus scanning electron microscope (SEM) equipped with energy dispersive spectroscopy (EDS) detector was used to study the morphology and chemical composition of both the virgin and spatter powders. To compare the crystallographic phases of the powders X-ray diffraction (XRD) was performed by Bruker-D8 Discover in the 2θ range from 25˚ to 120˚. Microstructural studies were conducted through polishing the cross section of the powder particles with standard metallographic practice. The prepared surfaces were etched by Glyceregia [84] for 60 s. Differential scanning calorimetry (DSC) was performed to analyze the thermal behaviour of spatter and virgin powders using a NETZSCH-STA 449 F1 Jupiter (NETZSCH-Gerätebau GmbH, Selb, Germany) thermal analyzer from 25 °C to 1500 °C with a heating rate of 10 °C/min in an argon atmosphere.

3.2.2.2 Density Measurement

Helium pycnometry by a Quantachrome Multipycnometer (Anton Paar, Graz, Austria) was used to measure the density of the powders. Computed tomography (CT) method using a ZEISS Xradia 520 Versa (ZEISS, Oberkochen, Germany) was used to find the density and porosity of the printed parts. 3D CT scan was performed at 10 W, 160 kV with an exposure of 3 s per image for a total of 801 2D projections. The 3D images were constructed using a beam hardening constant of 0.05 and analyzed in Dragonfly 3.1 (Object Research Systems (ORS), Montreal, Canada).

3.2.2.3 Surface Roughness Measurement

Surface roughness (Sa) for the Top, Front and Side of the part as shown in Figure 33b were measured using a Keyence VK-X250 confocal laser microscope. (Keyence Corporation, Osaka, Japan). On each surface, nine areas with dimensions of 1500 µm by 1000 µm were scanned for surface roughness measurements. The variation of the surface roughness across the build plate (Figure 33a) for the Top, Front and Side surfaces (Figure 33b) was studied. Figure 33a shows a

schematic of the printed parts on the build plate, the direction of the argon flow (from Inlet to Outlet) and the starting point of moving recoater direction. Figure 33c shows one of the printed LPBF parts. It should be noted that in Figure 33b, the Top surface corresponds to the surface parallel to the build plate, whereas the Front and Side of each part correspond to the surface parallel and perpendicular to the recoater moving direction, respectively.
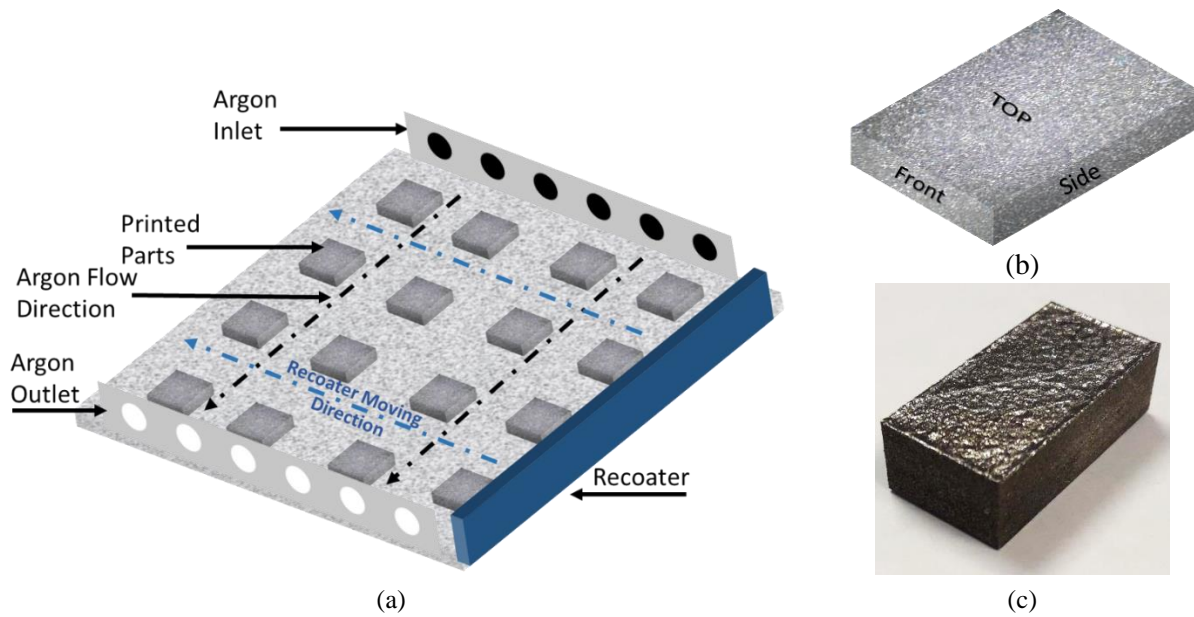
Figure 33 (a) Build plate schematic during LPBF showing argon flow, argon inlet/outlet and Recoater direction (b) Measured surfaces for roughness on the LPBF-made parts (c) Printed part

3.3   Results and Discussion

3.3.1   Powders Characterization

SEM images of virgin and spatter powders are shown in Figure 34a and b, respectively. Virgin powders are mostly spherical with satellites attached to the powder surface. Clustering and satellite formation are typical features of powders produced by gas atomization, which is the case for the current virgin powders. Similarly, the spatter powders are spherical with fewer satellites on their surfaces but have a larger average size. Figure 34b inset shows a spatter powder of ~100 µm diameter with smaller particles clustered around it. Even though spatter powders have larger size, clustering increases their size even further and changes their shape. On the other hand, virgin powders show a maximum size of around 45 µm (D90 < 46.4 µm). It has been shown that spherical

40

powders are the best choice from packing and flowability point of view [85]. Several studies in the literature have shown that the altered aspect ratio affects the flowability and packing of the powder particles drastically [86,87].

It is imperative that in this study spatter powders (Figure 34b) do not show black regions on their surfaces. This is an indication of low oxidation during LPBF [76] and higher oxidation resistance of nickel alloys. Oxides formed on the surface normally change the density of the powders. Helium pycnometry results on the virgin and spatter powders show the exact same density of 8.29 g/cm3 for both the virgin and spatter powder particles.

Based on the literature [70], larger spatter powders are splashes from the melt pool and spatter powders with the same size as of the virgin powders could be either melt pool splash or hot/cold ejections. This size difference could affect the layer thickness (60 µm in this case) irradiated by the laser. For example, a 100 µm spatter formed could increase the actual layer thickness locally from 60 µm to 160 µm. This extra material within the interaction zone results in higher the surface roughness [45,68,88].

(a)   (b)
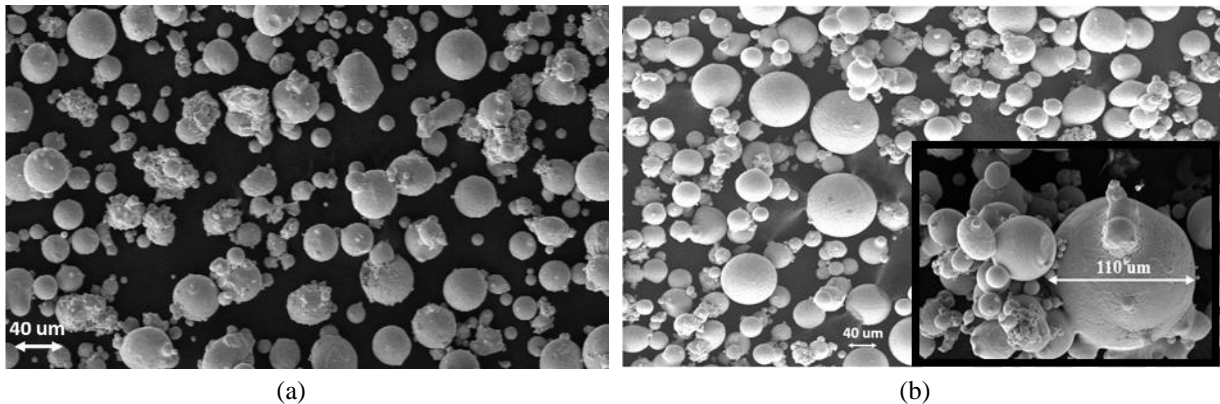
Figure 34 SEM image of (a) Virgin powder and (b) Spatter powder.

The cross-sectioned microstructure of the virgin and spatter powders are shown in Figure 35. The virgin powders show finer dendritic microstructure, which is commonly seen in the gas atomized metallic powders especially with less than 50 µm diameter [89]. Fine metallic AM powders, produced by gas atomizing, undergo high cooling rates after the gas and melt stream interaction causing dendritic solidification in a multi component alloyed metal (Figure 35a). Unlike, the spatter powders show equiaxed grains (Figure 35b). This difference in the microstructure is due to change in cooling rates, temperature gradient and interface velocity, in the gas atomized virgin

powders leading to a dendritic growth whereas changes in the solidification conditions result in an equiaxed grains for the spatter powders [33].

In the gas atomization process, a high-speed inert gas goes through the melt stream and creates turbulence in the melt stream. This process produces separated droplets, which then solidify to form powder particles. However, in LPBF, droplets, ejected from the melt pool, interact with a mild gas flow that results in a lower heat dissipating gas flow. In addition, as spatter particles have a larger size, the accumulated thermal energy in the spatter droplet (right after ejection from the melt pool) is higher than the equivalent accumulated thermal energy during the atomization of virgin particles. The combination of high accumulated heat and a lower heat extraction flow results in changes in the solidification conditions causing equiaxed microstructures in the spatter powder particles [33].

(a)   (b)
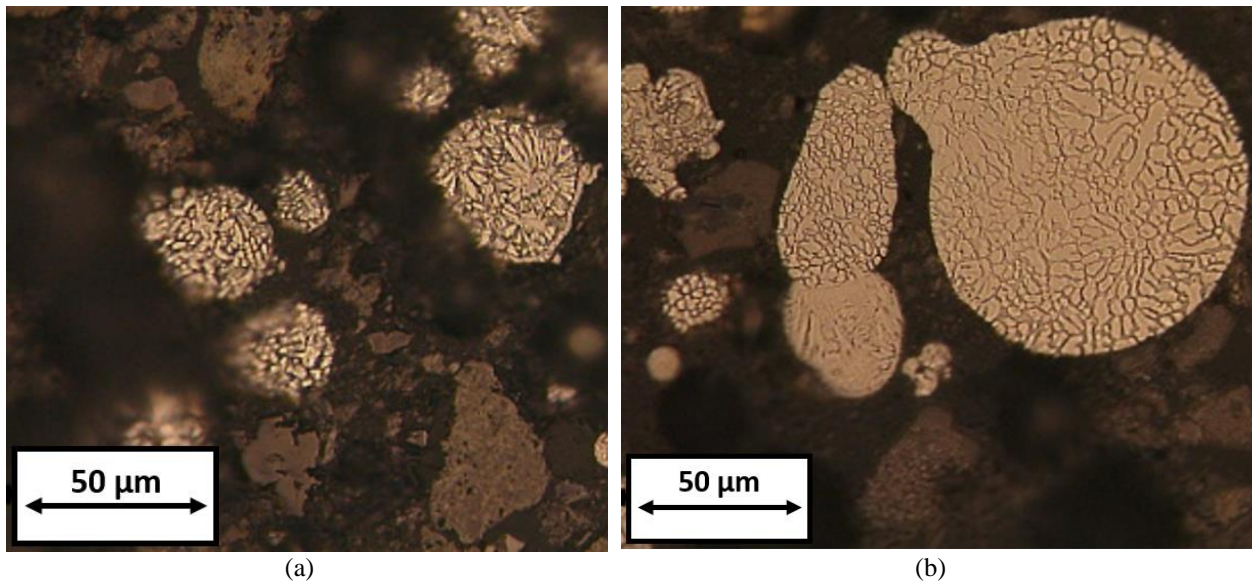
Figure 35 The microstructures of (a) virgin powder and (b) spatter powder as revealed by an optical microscope.

EDS analysis was performed on virgin (Figure 36a) and spatter (Figure 36b) powders to investigate the effect of laser exposure and remelting during the spatter particles formation on the chemical composition of the particles. As seen in Figure 36, these two powders show chemically identical results. It can be concluded that the ejection of droplets from the melt pool does not change the major alloying elements contents. This is mainly because the process is conducted in an inert environment.
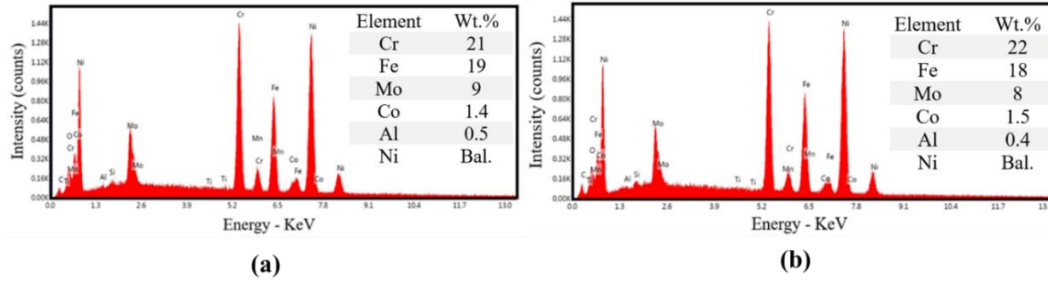
Figure 36: EDS analysis for the major alloying elements of (a) Virgin powder and, (b) Spatter powder.

Figure 37 depicts the XRD pattern of the virgin and spatter powders. Results indicate that, as also seen in the literature [90], the virgin powder contains only face centered cubic (FCC) phase. Based on the results of EDS, it can be concluded that all the alloying elements formed a uniform solid solution in Nickel during the atomization process [91]. The XRD pattern of the spatter powder (Figure 37b) is the same as that of the virgin powder, which indicates that the spatter particles formation does not introduce any change in crystallographic phases in the powder. Similar to the virgin powder, alloying elements in the spatter powder also form a solid solution. Although different solidification conditions for the virgin and spatter powders lead to different microstructures (Figure 35), it does not cause considerable segregation or formation of phases other than the FCC solid solution phase in the spatter powder.
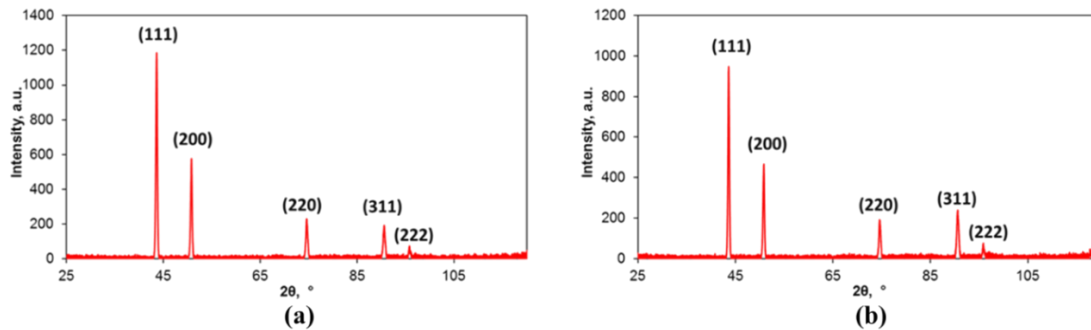
Figure 37: XRD patterns for (a) Virgin powder and (b) Spatter powder

During the LPBF process, temperature of the powder particle starts from the build plate temperature (80 °C) and reaches the melting temperature with very high heating rates [5]. Although the heating and cooling rates during the LPBF process [3] are much higher than the maximum achievable rates in DSC (50 °C/min), a comparative study on thermal behaviour of virgin and spatter powders can be performed to understand the differences, if any , between these

43

powders. The DSC results of virgin and spatter powders are shown in Figure 38. It shows that there was no considerable change in the DSC curves observed before melting for both powders. This indicates that the solid solution phase, which formed during solidification, is stable and does not go through any transformation or decomposition in continuous heating up to the melting point. Thermograms of these two powders indicate that they have the same melting range between 1350 °C and 1400 °C. In other words, the introduction of spatter powders does not change the overall thermal behaviour of the build plate. This is an important conclusion because different melting ranges of virgin and spatter powders could have caused non-uniformities in different forms such as instability in the melt pool and un-melted zones. These un-melted particles will have an effect on the mechanical and especially fatigue properties of the printed samples. The effect of un-melted particles on fatigue properties has been studied as they cause stress concentrations during loading [15,16,46,92,93]. However, as concluded, having similar thermal properties, the spatter powder will not cause the aforementioned problems for LPBF.
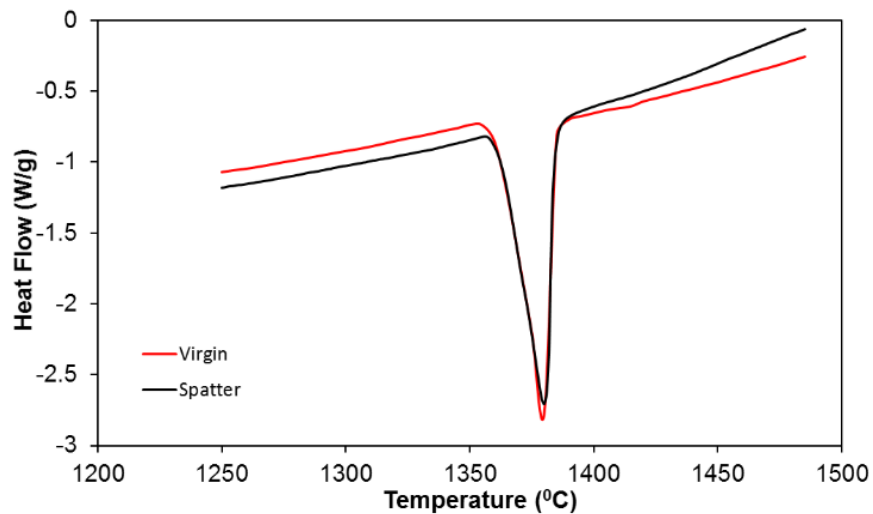
Figure 38 Thermograms of virgin and spatter powders.

Results presented in this section show that chemical composition, phases and thermal behaviour of spatter and virgin powders are similar. However, they are different in their size and microstructure.

3.3.2 Printed part properties

Figure 39a-c demonstrates the surface roughness on the Top, Side, and Front surfaces of printed parts. A detailed schematic showing the Top, Side and Front surfaces is shown in Figure 33b. Each

square in Figure 39 represents the location of the printed part on the build plate and the color represents the surface roughness on the Top, Side and Front, respectively. As seen, the best surface is observed in the middle of the build plate for all the surfaces as highlighted by the dashed lines.

Figure 39 shows that the roughness is increased in the argon flow direction and the maximum roughness is located at the last row. However, the change of roughness in the recoater moving direction is not significant except for the parts closest to the argon outlet, where an increase in the surface roughness is observed along the recoater moving direction. By comparing the roughness values for the two horizontal rows in the middle, other facts can be described better. Firstly, the middle rows have better surface finish in comparison to the last one. This might be attributed to the higher population of the spatter powder in the lowest part of the build plate (last row in Figure 39), which increase the average particles size in that region. Secondly, the effect of recoater motion is more pronounced in this region, where the recoater brushes larger particles during its motion. The roughness variation for the middle row from right to left (recoater moving direction) is not considerable, however this variation for the last row is significant, and it is increasing from 14.4 µm to 28 µm.

It is important to analyze the part consistently, as the roughest part may be defined by the worst surface roughness value across all surfaces, although, some surfaces could be more important than others due to their functionality that is required for the specific application. Our investigation reveals that the Top, Front, and Side surfaces show average roughness of 16 µm, 22 µm and 20 µm, respectively. Therefore, the Top surface shows the best surface finish across the build plate followed by the Side and Front surfaces. Further, the parts, which have high Top roughness of 28 µm, 21.2 µm and 21.6 µm (Figure 39) show similar trend of high roughness for the Front and Side surfaces.
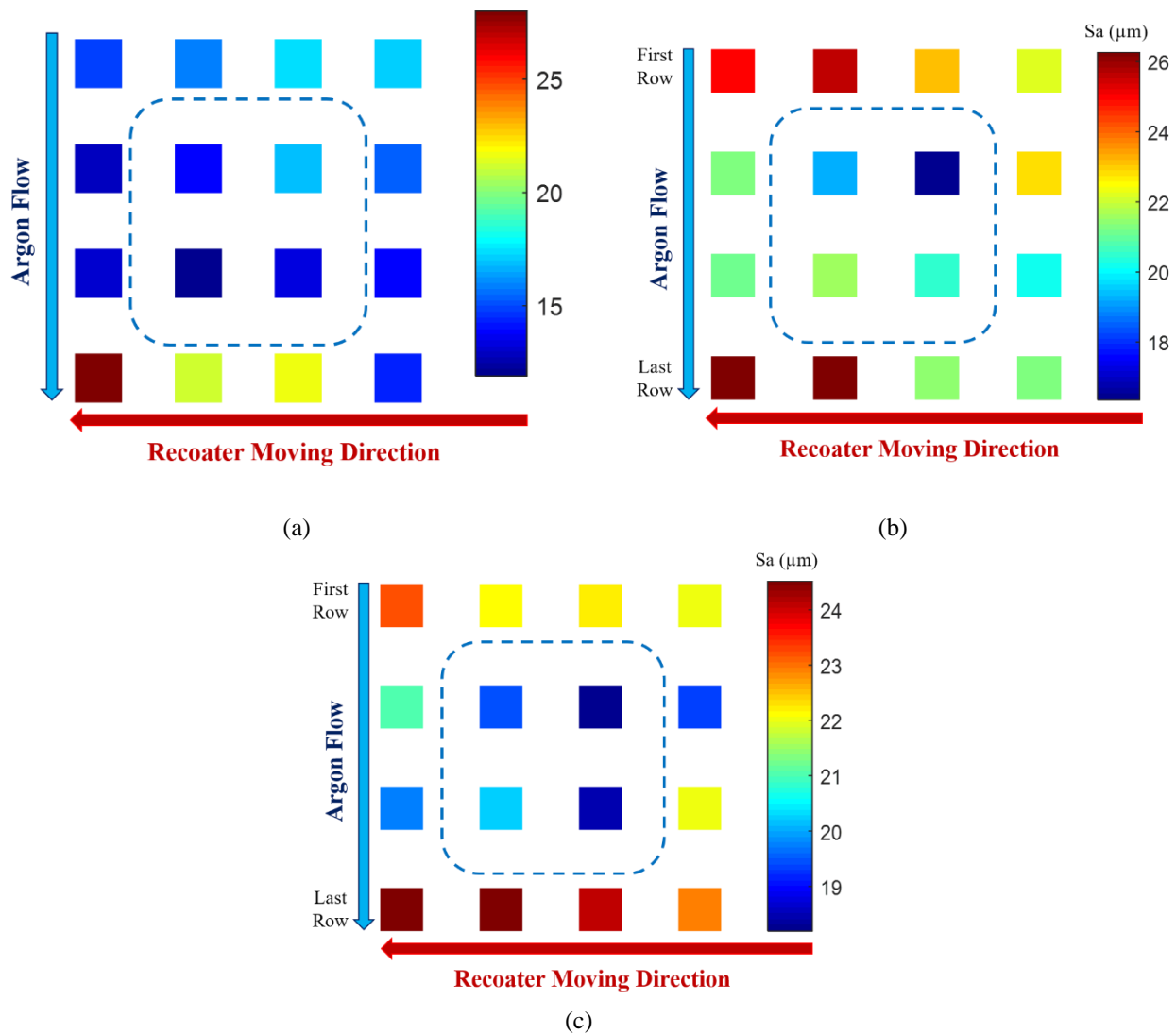
Figure 39 Surface roughness (Sa) map of the LPBF-made samples across the build plate on (a) Top (b) Side, and (c) Front surface.

Higher roughness of the parts in front of the perforated argon inlet (first row in Figure 39) may be attributed to the instabilities due to the argon flow. The next two rows represent the middle of the build plate where the argon flow reach a stable condition and hence exhibit the lowest surface roughness. The printing sequence of these parts was started from the left most part on the last row while moving in the right direction. The next row was printed in the same order until the right most part on the first row was printed. Due to this printing order, spatter ejections from all the rows are deposited on the bare surfaces of the previous rows. It should be noted that as the spatter powders eject from the melt surface they fly outward in the argon flow direction although, some particles with higher kinetic energy go against the argon flow but due to the opposing drag force, they fall

very close to the melt pool. This process is shown schematically in Figure 40. Thus, it can be concluded that most of the spatter particles accumulated near the back (last row in Figure 39) of the build plate (spatter rich region) whilst a few falls opposite to the argon flow direction.

In this study, all the surfaces undergo the same laser exposure parameters, however, different regions of the part experience different laser-powder interaction. For example, the Front and Side surfaces of the part have layer-by-layer roughness development as they are parallel to the build direction, while the Top surface is perpendicular to the build direction and part of the same layer. Side surfaces develop surface roughness due to partially melted particles or attached powders due to surface-powder interaction [45,73]. As spatter rich regions have larger powder sizes, these parts exhibit high surface roughness on Side surfaces. Several possibilities exist for the Top surfaces. Firstly, as spatter powders fall on the surface, they could stick to the surface. This would cause problems in the recoater motion and could even stop the process due to blockage of the recoater. Secondly, the spatter powder could fall but not bond to the surface. As spatter particle size is bigger than the defined layer thickness (~100 µm compared to 60 µm), they might be swept by the recoater causing local scratches on the free surface of the build bed. However, if they lay in a valley [94] on the surface, they will not be swept away and will produce an uneven particle distribution on the laser interaction area and therefore will affect the applied layer uniformity and consequently the final part properties [82,95].
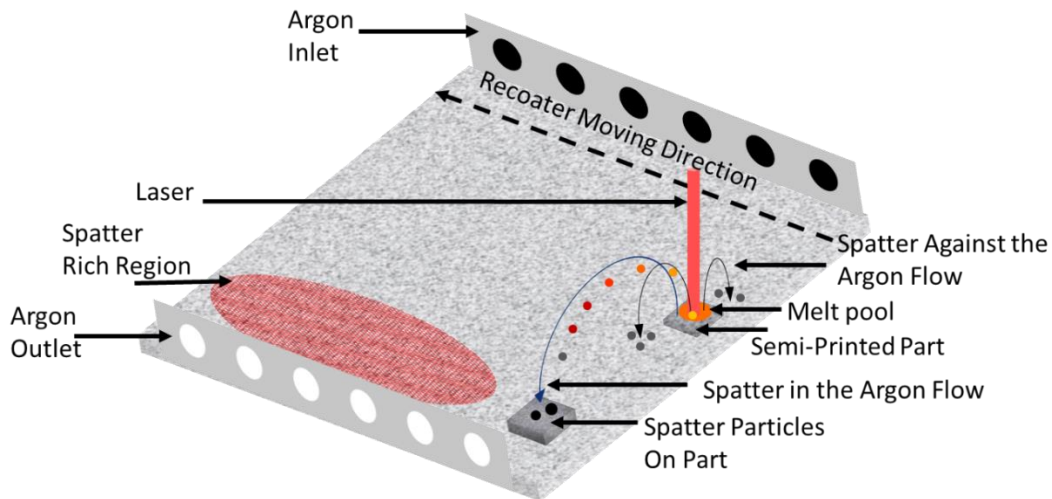
Figure 40 Schematic representation of spatter formation, types and effect on build plate, powder bed and printed parts

It is important to study the surface morphology (i.e., the distribution of peaks and valleys) on the printed parts. The sample with high peaks and similar surface roughness could affect the recoater motion as well as the part quality, whereas a sample with the same surface roughness but lower peaks may not affect the recoater motion. Figure 41 shows the surface morphology of the top surface for some of the LPBF-made samples. The dashed white circles in Figure 41 show the high peak areas on the top surface. It is observed that the surface morphology changes from a uniform distribution of low peaks in the middle of the build plate to non-uniform distribution of high peaks in the spatter rich region. This change from uniform roughness distribution (in the middle of the build) to non-uniform high peak roughness (in the spatter rich region) is due to the change in the powder bed characteristics. Accumulation of spatter particles at bottom of the build plate changes the powder size distribution and increases the average particle size thus the surface roughness of the printed parts.
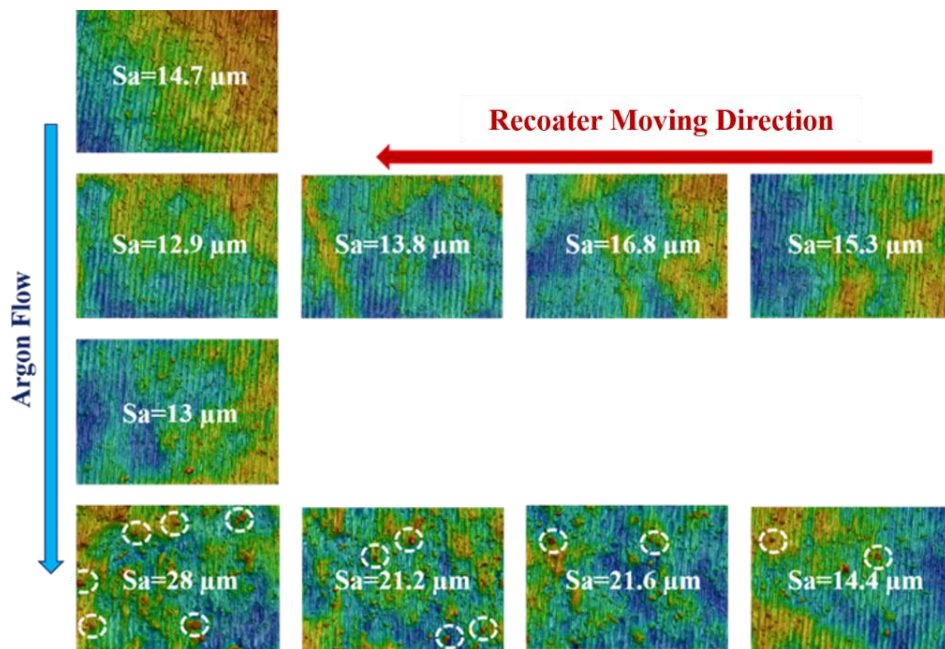
Figure 41 Surface roughness map of Top surface across the build plate

The surface morphologies of the parts are shown in a single 3D image (Figure 42). Each surface of the 3D object corresponds to a surface of the part and the colors on each surface of the object represent the heights on all surfaces. Figure 42a shows roughness on a sample in the middle of the build plate whereas Figure 42b shows a sample in the spatter rich region. It should be noted that in Figure 42 all surfaces for both samples correspond to the same legend. Results show that the sample in the middle of build plate (Figure 42a) experiences less roughness on all surfaces.

Conversely, sample in the spatter rich region (Figure 42b) experiences high roughness on all surfaces as population and probability of joining big spatter particles to the surfaces is much more than that for middle of build plate sample. It is important to mention that the Top surface for both parts show different surface morphology. The Top surface of the rougher part (Figure 42) shows high peaks, which could have formed due to big-clustered spatter particles sticking on the top surface. However, surface morphology for smoother part shows a completely different trend, where small peaks have spread uniformly across the whole surface. Although the Side surface morphologies show similar trends for both parts, the part built in the spatter rich region shows higher peaks.
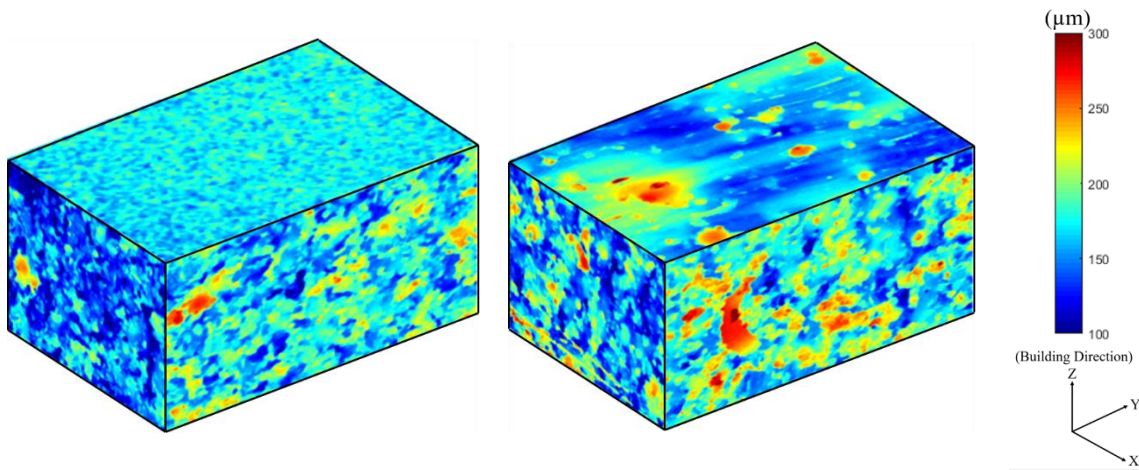
Figure 42 Surface height map on (a) Sample in the middle of the build plate (b) Sample in spatter rich region

Discussions from the previous sections show that due to the size and non-uniform distribution of spatter particles throughout the build plate, the printed parts with the same process parameters exhibit different surface roughness across build plate. The analysis presented in this study proposes that this effect is not only limited at the surface but also affects the internal part quality. As the spatter particles influence each layer, this could affect the part density as well. Simchi et al [96] and other studies [97–99] have shown that the density of printed parts is inversely proportional to the layer thickness. As spatter particles increase the overall layer thickness, it is important to investigate the effects of spatter particles on internal part properties.

To study the effect of spatter particles on part density, Nano-CT was performed on two samples, one from the middle of the build plate (Figure 43a) and the other from spatter rich region (Figure

43b). Figure 43 clearly shows that the part from the spatter rich region shows more porosity than the part from low spatter region. This proves the hypothesis mentioned earlier that spatter powders introduce irregularities in the powder layer. Thus, large spatter powders hinder the complete melting of the powder layer and consequently increase the probability of lack of fusion and pore formation. It is important to mention that CT scans of these parts shows different pore shapes. Compared to relatively spherical pores in the middle of the build plate, part printed in the spatter rich region shows elongated pores with irregular shapes. This shape difference is an indication of different pore formation mechanisms seen in these parts. Irregular and elongated pores are usually formed due to incomplete melting and fusion between layers [15]. Due to their size, presence of spatter particles discourages complete melting, thus causing elongated pores. On the other hand, spherical pores are an indication of gas pores which could be formed from the gas porosities in the powders or entrapped gas between them [15].

It is also important to discuss the pore size distribution in these samples. Figure 43 shows that the part printed in the spatter rich region shows higher pore size (23.8 µm) compared to the part printed in the middle of the build plate (19.9 µm). Several studies in the literature [14,45,50,92] have shown that pores can act as stress concentration points and affect the mechanical properties. In addition, the bigger pores have a more pronounced effect thus leading to a much lower mechanical strength [100].

| 12.2 µm | 15.0 µm | 16.9 µm | 18.6 µm | 19.9 µm |

(a)

| 14.8 µm | 15.1 µm | 20.3 µm | 22.2 µm | 23.8 µm |

(b)
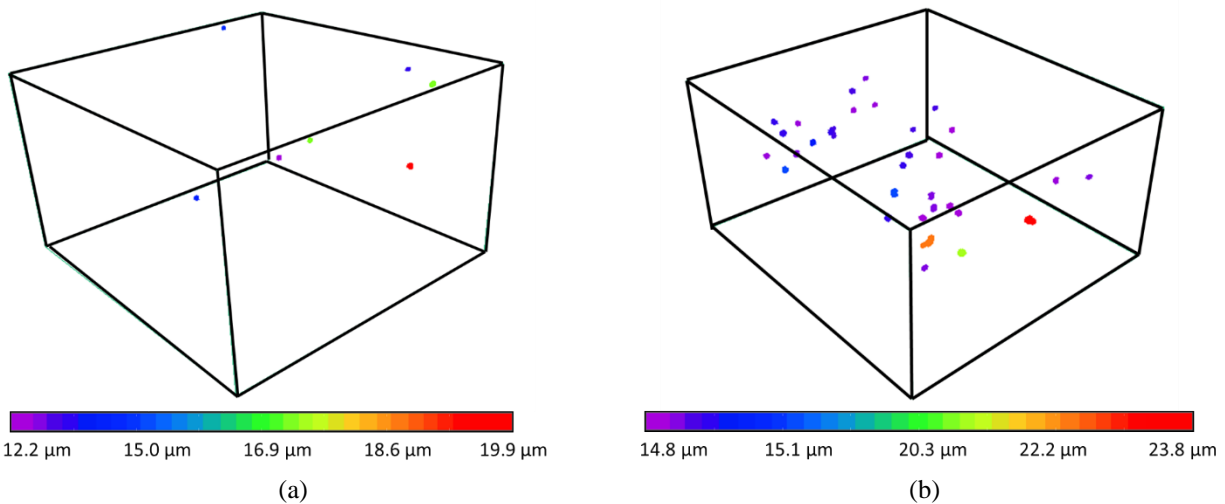
Figure 43 Computed tomography (CT) results (a) Samples in the middle of the build plate (b) Sample in the spatter rich region

3.4   Conclusions

In this work, a systematic study on the virgin and spatter powders has been conducted. In addition, the effect of spatter powder distribution on the roughness and density of printed parts was studied. Based on the observed results, the following conclusions are drawn:

1- Chemical composition, crystallographic phases and thermal behaviour of virgin and spatter powders are relatively identical.

2- Virgin and spatter powders exhibit different size distribution. Although the virgin particles diameter does not exceed 45 µm, the diameter of spatter particles and clusters exceeds 100 µm.

3- Due to the different formation processes, virgin and spatter powders show different microstructure. Solidification conditions during the atomization process result in dendritic solidification structure in the virgin powder, while changes in the temperature gradient and interface velocity in the spatter powder encourages the formation of equiaxed microstructure in the large spatter powder.

4- Argon flow entraps and transports the spatter particles, formed during LPBF, to the bottom of the build plate, which results in a spatter rich region.

5- Printed parts in the spatter rich region show higher surface roughness from 14.4 µm to 28 µm, whereas the parts printed in the middle of the build plate have a surface roughness from 12.9 µm to 16.8 µm.

6- Parts printed in spatter rich region have high porosity and therefore lower density. In addition, the maximum pore size of parts printed in the spatter rich region (23.8 µm) is larger than the maximum pore size of the parts printed in the middle of the build plate (19.9 µm).

7- Results presented in this study show the effect of spatter particles on part quality. To achieve maximum part quality, it is recommended to avoid printing in the spatter rich area (lower 15%) of the build plate. This would ensure consistent part quality and improve repeatability during LPBF. In addition, results presented in this study highlight the importance of powder sieving during repeated powder use in powder recycling and repeatability studies.

Chapter 4

4 Customizing Mechanical Properties of Additively Manufactured Hastelloy X Parts by Adjusting Laser Scanning Speed

4.1 Introduction

As a novel manufacturing process, additive manufacturing (AM) produces parts by depositing a new layer of powder material on the preceding solidified layer [6]. Laser powder-bed fusion (LPBF) is one of the main metal AM methods, which is able to produce complex metallic parts with fine features [101]. Due to the complicated physical phenomena caused during the LPBF process (laser-powder interactions) [70,72], as well as the numerous process parameters involved [60,102], fabricating a part with optimum properties is challenging. In addition, the process parameters are material dependent and therefore add to the complexity of the process optimization [103–105]. Design of experiments, can be used to reveal the interdependencies of parameters on part properties; however, it entails extensive datasets that call for many experiments [106]. An alternative approach for exploring the effect of each process parameter is to focus on a specific parameter while keeping the other parameters fixed (one-factor-at-a-time or OFAT [107]). This approach (OFAT) might not result in the optimum parameters but can be used to study the printability and quality of printed parts with a minimum amount of experiments. In addition, this approach allows the study of extreme and moderate conditions of a single parameter.

Hastelloy X (HX) is a solid solution strengthened nickel-based superalloy and is widely used in gas turbine engines and petrochemical reactors [108,109]. Because of its high work hardening capacity [90,110], machining complex parts out of this alloy is difficult [111]. Owing to the acceptable laser weldability of HX [112], LPBF, can be considered as an alternative manufacturing method for this alloy. There are several reports on different aspects of LPBF manufactured HX parts. Wang et al. [12] reported that the mechanical properties of printed HX parts under quasi-static loading are independent of the print location on the build plate. The higher strength of horizontally built samples in comparison to the vertically built sample has been reported by Tomus et al. [17]. Keshavarzkermani et al. have studied the effect of laser scanning strategies on the mechanical properties of Hastelloy X LPBF parts. Their results show that the highest strength

(UTS) was obtained in parts printed with rotation scanning strategy built horizontally [113]. These reports on LPBF-made HX show that there is variability in the reported values of mechanical properties in terms of yield strength (450 MPa [48] to 800 MPa [12]) and elongation to failure (30% [17] to 40% [48]) which could originate from the use of different manufacturing machines, starting powders, and process parameters.

Despite several reports on mechanical properties of additively manufactured Ni-based superalloys and specifically HX, there is no systematic study on the tensile response of the as-built parts with different manufacturing conditions. Knowing that the laser scanning speed (LSS) is one of the most significant process parameters involved in LPBF, the aim of this study is to explore the effect of LSS (550 to 2050 mm/s) on the tensile behaviour of LPBF-made HX samples. Therefore, printed LPBF parts from a wide range of LSS are used to explore the effects of LSS on the part density, macro and microstructure and corresponding mechanical properties. Results show the effect of keyhole and lack of fusion porosities on the mechanical response of printed parts at low and high LSS, respectively. In addition, moderate LSSs (850 to 1300 mm/s) result in high dense parts with varying mechanical properties due to the microstructural features observed in these samples.

4.2   Experimental Methods

EOS M290 equipped with a Ytterbium fiber was used for manufacturing the tensile samples (Figure 44) with three repetitions for each laser scanning speed from Hastelloy X powder supplied by EOS with powder size of D50 < 30 µm [61]. All samples were manufactured vertically with a laser power of 195 W, the layer thickness of 0.04 mm, hatching spacing of 0.09 mm, 5 mm stripe width with rotating scanning vectors (67°) in each successive layer, and the build plate temperature of 80˚C. After printing, the samples were cleaned and the 5 mm support structures were removed. Laser scanning speed was altered from 550 to 2050 mm/s to study its effect on the quasi-static tensile behaviour of as-built parts.
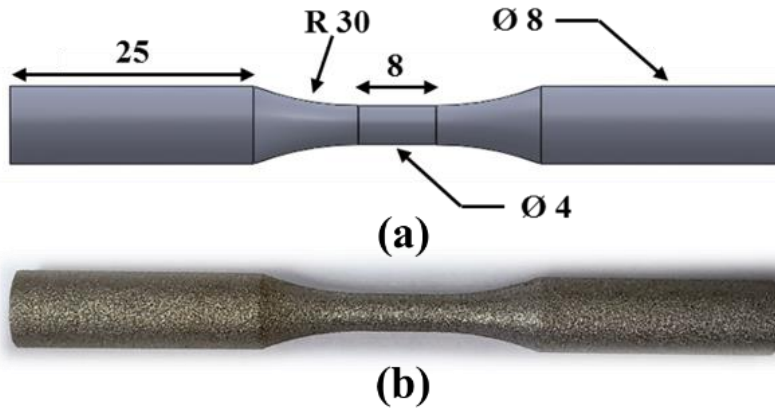
Figure 44 (a) CAD model of tensile sample geometry with dimensions in mm, (b) a typical printed sample

Instron 8872 servo-hydraulic machine with a load capacity of ±25 kN was used for quasi-static tensile testing under standard laboratory conditions. The tests were performed according to ASTM E8 standard [114] in the displacement control mode at the rate of 0.45 mm/min. An Instron 2630-120 extensometer with 8 mm gauge length and ±4 mm travel was used.

ZEISS Xradia 520 Versa X-ray computed tomography (CT) was used to find the defects distribution in the additively manufactured samples. CT scan of 801 2D projections was performed at 10 W, 160 kV with an exposure time of 1 s per image. A beam hardening constant of 0.05 was used for re-construction and the 3D images were analysed in Dragonfly 3.1.

Keyence VK-X250 confocal laser microscope was used for optical microscopy. In this work, BD (Building Direction) cross-section is perpendicular to the building direction and ND (Normal Direction) cross-section is parallel to the building direction. SiC grinding papers from 320 to 4000 grit sizes were used progressively for grinding and polishing of the cross-sections followed by polishing with 1 to 0.05 µm alumina slurry. The prepared surfaces were etched by Glyceregia [84] for 40 seconds. For the EBSD analysis, the final surface preparation was done with alumina slurry and colloidal silica suspension in the vibratory polisher. JEOL7000F scanning electron microscope (SEM) equipped with an Oxford EBSD detector was used to study the grain structure and crystallographic texture of the manufactured parts with different laser scanning speeds. AZtecHKL was used for EBSD data collection and all post processing was performed with HKL Channel 5. Zeiss 1550 field-emission scanning electron microscope (FE-SEM) was utilized to analyze the fracture surface.

4.3   Results and Discussions

4.3.1   Macrostructure and Defects

Optical images of the polished cross-section of fabricated samples at different LSS in BD and ND cross-sections are displayed in Figure 45. Samples produced with the lowest LSS (550 mm/s-Figure 45 (a)), shows spherical pores while defects with irregular shapes are present in the highest speed (2050 mm/s) samples (Figure 45 (e)). On the other hand, samples printed with 850 mm/s and 1150 mm/s do not show any significant porosities. Different defect shapes indicate different formation mechanisms for these defects [115,116]. Spherical pores are gas pores which are mainly produced through the formation of keyhole shaped melt pool [85,117]. Balling effect and instability in the melt pool may also originate such spherical defects. By decreasing the LSS, a deeper melt pool forms, where a higher input laser energy is used and a higher recoil pressure exists, hence, the melting mode may change from conduction to keyhole mode [118,119]. On the other hand, at the high LSS, the amount of available laser energy for the melt pool formation decreases significantly. Hence, with the decrease in the melt pool size and keeping the same hatching distance and layer thickness, the probability of having lack of fusion (LoF) will increase [119,120]. As indicated by yellow arrows in Figure 45(d), irregular-shaped porosities due to the LoF are observed at 1300 mm/s. By increasing the speed, the reduction in the laser input energy results in a narrower melt pool. This narrower melt pool can result in insufficient overlap as the hatching distance is kept unchanged. As indicated by red arrows in Figure 45 (e), due to the lower energy input, some un-melted powder particles are trapped inside the irregular lack of fusion porosities which were not observed with lower LSS. It should be noted that while the LoF defects have started to form at the speed of 1300 mm/s, the observed YS and UTS is higher than all the samples studied in this work.

In summary, the gradual increase in the mechanical strength, observed in the 850, 1150 and 1300 samples might be related to the microstructure difference and will be discussed in the next section.
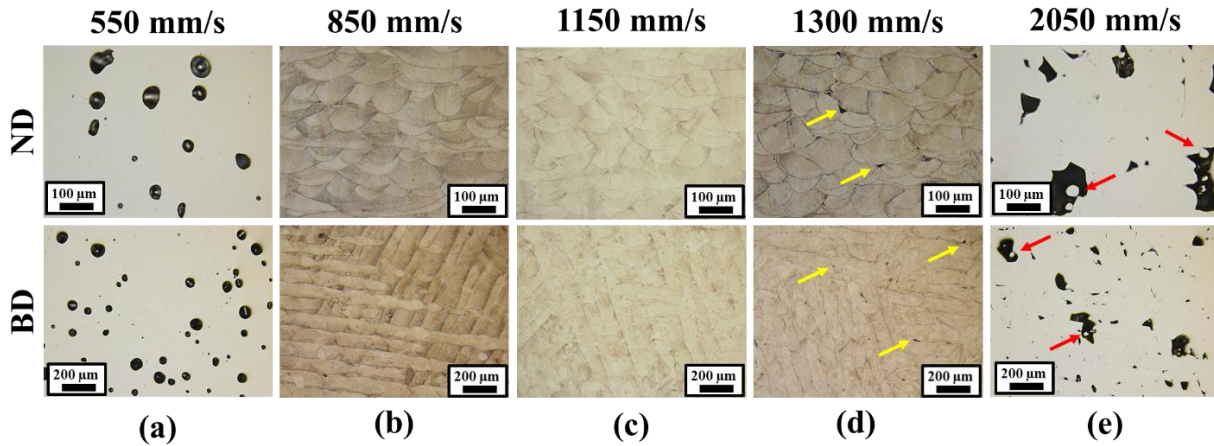
Figure 45 Macrostructure of BD and ND cross-sections of the samples manufactured with different laser scanning speed; (a) spherical keyhole gas pores, (b & c) close to fully dense condition, (d) sharp end porosities shown by yellow arrows, (e) LoF and unmelted shown by red arrows

A wide region X-ray CT analysis was also performed to study the defect morphology and distributions as shown in Figure 46a-b for samples manufactured with the LSS of 550 mm/s and 2050 mm/s respectively. The relative calculated densities from CT measurements were 98% and 96% for the 550 mm/s and 2050 mm/s samples, respectively. To visualize the difference between the size and shapes of the defects, only those defects that are larger than 60% of the maximum defect size are shown in the 3D reconstructed CT images. As the size of the keyhole pores is restricted by the melt pool size (~100 µm), LoF defects could have a much larger size. It should be noted that the LoF defects (in the range of 110 to 190 µm) observed in this work do have a much bigger size in comparison with the keyhole porosities (in the range of 50 to 80 µm). Due to the difference in pore size, keyhole and LoF porosities present different effective cross-sectional areas under tensile loading. This difference in load bearing cross-sectional area in these samples could affect the tensile response of these samples and is discussed below. Each pore and defect reduces the effective cross-section and increase the local stress in comparison to the nominal engineering stress, which is calculated based on the defect free cross-section assumption [15]. Moreover, the shape of these defects will directly influence the stress concentration. The keyhole porosities and irregular LoF defects in this study are similar to circular holes and sharp notches inside an infinite plate, respectively. In an elastic body, the stress concentration factor for circular holes is three and for sharp tip notches inside an infinite plate is infinite [43,121]. Stress concentration at the root and constrained deformation around it results in stress triaxiality and high local stresses near the defects, causing high local deformation in these areas [121,122].

Consequently void growths and coalescences will be accelerated [123]. Therefore, the existence of keyhole and LoF defects should result in overall reduced ductility [124].
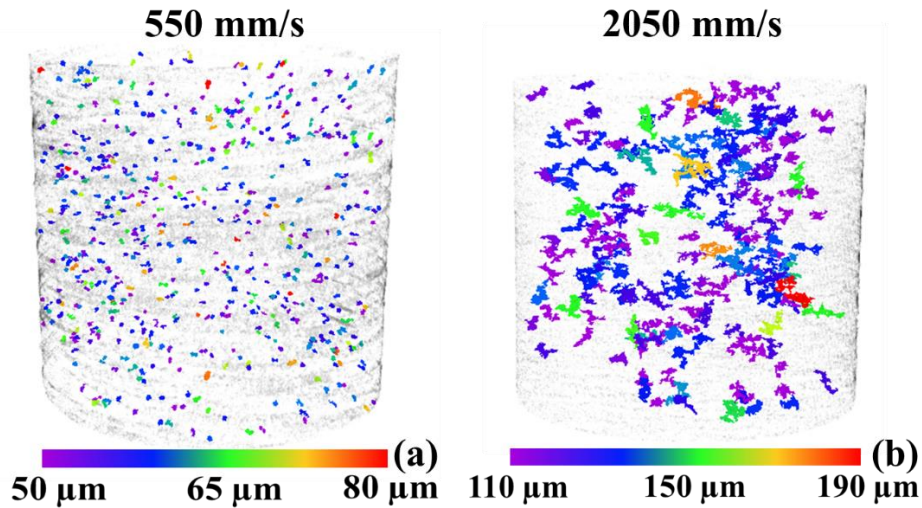
Figure 46 CT images of the samples manufactured with the extreme laser scanning speeds showing the process-induced defects. For clarity, only defects larger than 60% of the largest defect are shown in each case.

4.3.2 Microstructural Characterization

To investigate the effects of microstructure and separate it form the effects of defects the microstructural analysis was only performed on the low porosity samples printed with the LSS of 850, 1150 and 1300 mm/s. EBSD inverse pole figure (IPF) maps on the BD and ND cross-sections are shown in Figure 47. As illustrated in Figure 47 (a), (d) and (g), the morphology of grains in the ND cross-section is columnar for all three velocities. Columnar morphology is due to the epitaxial grain growth and directional heat transfer through the previously printed solid substrate and is widely observed for several printed LPBF materials [17,32,40,125]. These columnar grains are filled with a fine cellular structure for Hastelloy X due to the high solidification and cooling rates involved in the LPBF process [17]. On the other hand, the IPF map for the BD cross-section shows almost equiaxed grain morphology without having any unique preferred growth orientation in different successive layers (Figure 47 (c), (f) and (i)). This is attributed to the rotating main heat flow direction. IPF maps in Figure 47 show that the grain size is decreasing by increasing the LSS. A more detailed analysis on the effect of grain size is presented below.

Pole-figures from ND cross-sections are shown in Figure 47 (b), (e) and (h) for 850, 1150 and 1300 mm/s LSS, respectively. By increasing the LSS, the number of mapped grains increases because of the smaller grain size, which shows the presence of a more uniform texture, i.e. lower multiple of random distribution (MRD) values, in comparison with the samples produced with the lower LSS, i.e., Figure 47 (b) vs. Figure 47 (h). The lack of specific crystallographic texture is related to the rotation of laser scanning vectors by 67° in each successive layer, which disturbs the in-plane heat flow directions preventing the formation of strong textures in the as-built condition. Similar findings are reported for Hastelloy X and other Ni-based superalloys printed by LPBF [17].
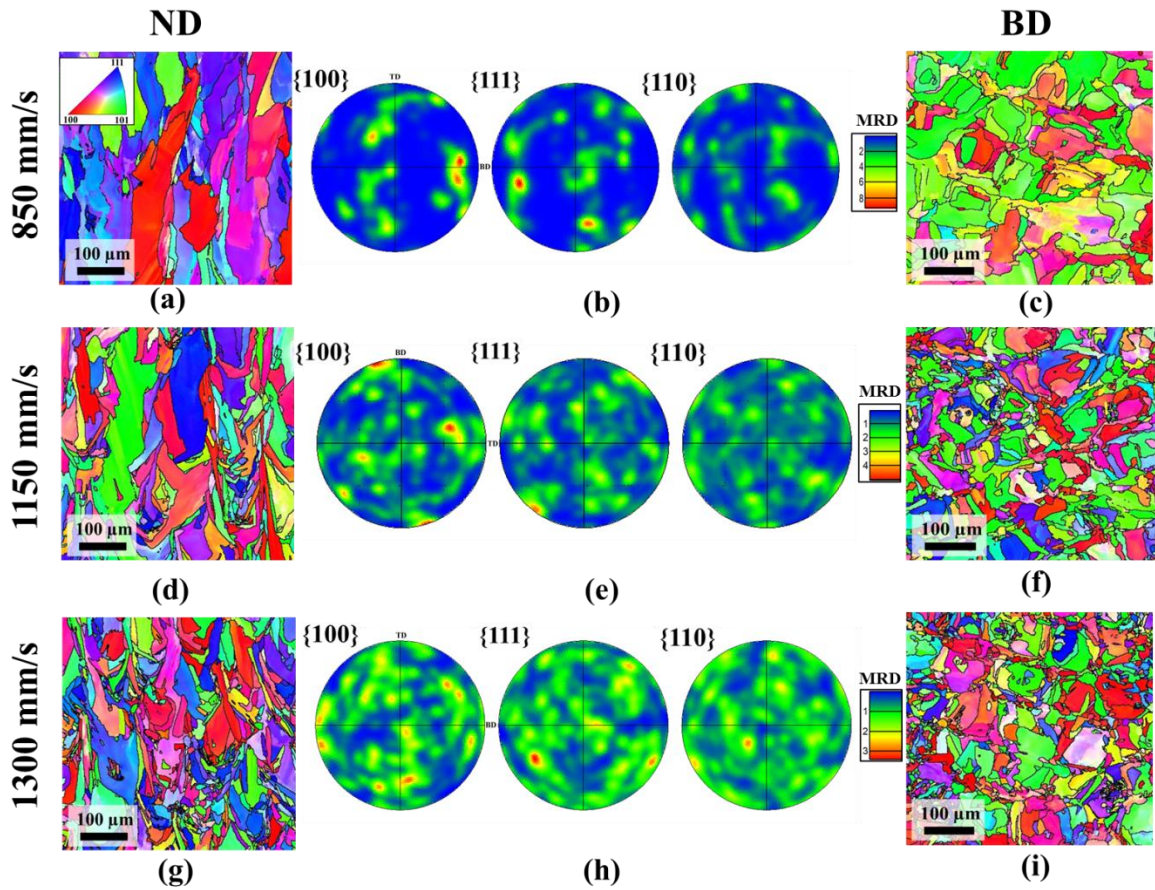
Figure 47 EBSD IPF maps including grain boundaries for ND, BD samples manufactured with laser scanning speed of (a), (c) 850; (d), (f) 1150; and (g), (i) 1300 mm/s showing the grain refinement as a function of LSS. Also, pole figures displayed from ND cross-sections of samples manufactured with (b) 850, (e) 1150, (h) 1300 mm/s showing random texture of the as-built material.

4.3.3 Quasi-Static Behaviour

Figure 48 (a) demonstrates the typical engineering stress-strain curves which are obtained from quasi-static uniaxial tensile tests for the as-built samples manufactured with different laser scanning speeds. The Young's modulus was found to be 153 ± 5.5 GPa and is independent of the LSS. The results in Figure 48 demonstrate that the mechanical properties of the additively manufactured parts is strongly influenced by the process parameters. Starting from the minimum LSS of 550 mm/s, by increasing the LSS, the yield strength (YS), ultimate tensile strength (UTS), and percentage elongation at the fracture or fracture strain (FS) go through an increase followed by a decrease as shown in Figure 48 (b). The maximum ductility, i.e., the fracture strain of 65% corresponds to the samples produced by scanning speed of 850 mm/s. The highest strength is related to the samples produced at 1300 mm/s with YS and UTS values of 489 and 706 MPa, respectively. High fracture strain values except for the samples printed with high speeds reveals ductile behaviour which has been reported in previous studies [17,48]. Moreover, results presented in Figure 48 suggest that it is possible to produce additively manufactured parts possessing desired and/or designed mechanical properties. Controlling the mechanical properties of LPBF parts has been studied previously for build orientation [50,126,127], scanning strategy [128,129], layer thickness [126], hatch spacing [105], and laser speed [130]. The results of this study (Figure 48) also show that tensile properties in terms of strength and ductility could be greatly affected by the LSS. This will help designers and manufacturers to produce a part not only based on the structural requirements, but also the desired microstructure as well.
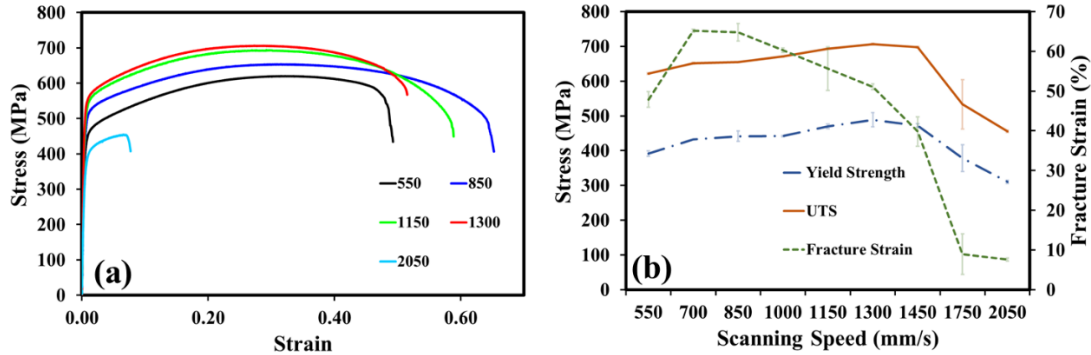
Figure 48 (a) Engineering stress–strain curves, (b) Variation of the yield strength (YS), UTS, and Fracture Strain of LPBF processed Hastelloy X samples at the laser power of 195 W with different laser scanning speed.

4.3.4   Grain Refinement Mechanism and Hall-Petch Relationship

By reducing the input energy via increasing the LSS, the size of the melt pool decreases that eventually results in lack of fusion. The melt pool size reduction means that there is less volume available for grains to grow, hence the grain size reduction is expected to occur. Further analysis of the grain morphologies, as shown in Figure 49, reveals that the melt pool size reduction is not the only possible mechanism for finer grains at the higher LSS. The random color mapping images of the detected grains form EBSD analysis in the ND cross-sections are shown in Figure 49 (a)-(c). As shown by dashed white circles, there are specific regions in the microstructure, which the columnar grain morphology is disturbed and changed toward the equiaxed microstructure. By increasing the LSS, the number of agglomerated equiaxed grain structure, denoted by the dashed circles, have increased significantly. This change in columnar grain morphology is related to the cease of epitaxial grain growth under the high LSS condition. By increasing the LSS, the heat input for melting of the powder-bed and re-melting the previous printed layer is decreased and the chance of entrapment of partially melted particles (PMP) in the melt pool increases [131]. These PMPs will act as inoculants inside the melt pool, introducing random grain orientations to the microstructure. Therefore, a significant grain refinement may happen due to nucleation and introduction of new grains. Moreover, the introduction of these new grains explains the random textures observed in the as-built condition. Previously, Cunningham et al. [119] has reported that this partially melted particle at the wake of the melt track are the main sources for small gas porosities in the as-built additively manufactured parts.
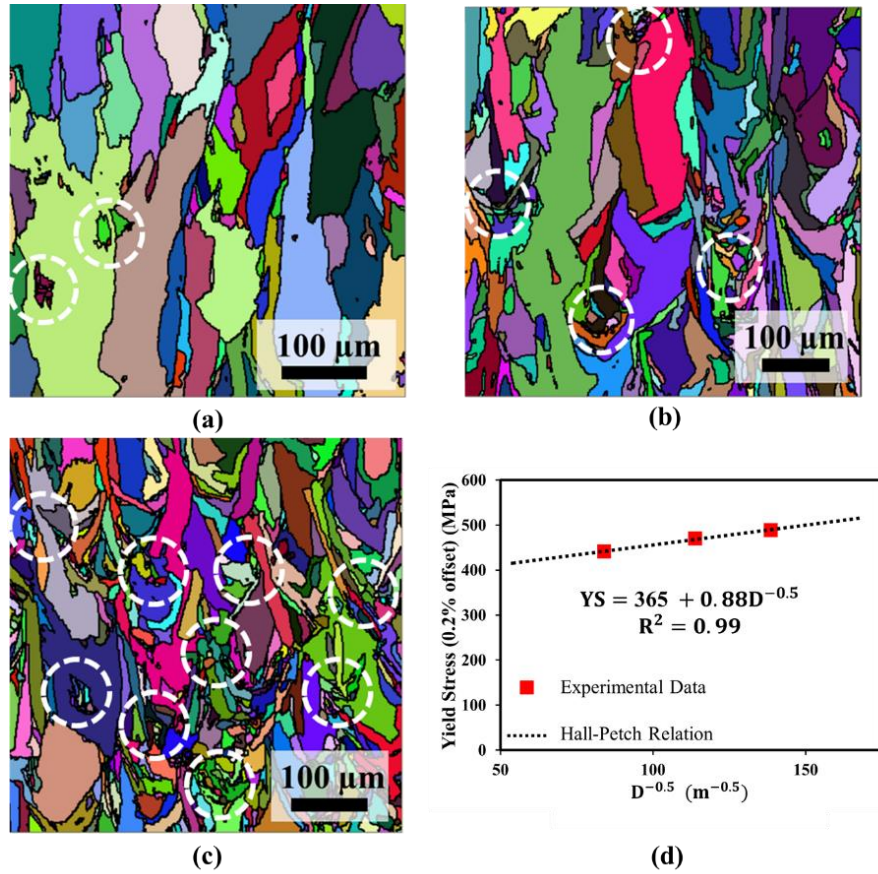
Figure 49 Random color mapping of ND cross-section grains for samples manufactured with the speed of (a) 850, (b) 1150, (c) 1300 mm/s and (d) yield stress (0.2% offset) vs. the reciprocal square root of the grain diameter. Dashed white circles show the PMP which act as nucleation sites for new grains.

To study the validity of the Hall-Petch relationship for the LPBF-made samples, the grains size analysis has been performed on the IPF maps. To measure the grain size, ECD (equivalent circle diameter) has been calculated for each sample in the ND and BD cross-sections (Table 3). Based on ASTM E-112 [132], the average grains size for an elongated grain morphology (such as the columnar grain morphology observed in LPBF parts), can be calculated from the geometric average of the grain sizes in three perpendicular planes. In this study, due to the rotational scanning strategy, all planes parallel to the building directions (ND planes) are assumed to show similar microstructures, hence, ND cross-section has been used for two of the three perpendicular planes. Therefore, the average grains size ($D_{Average}$) was calculated according to:

$$D_{Average} = (D_{ND} \times D_{ND} \times D_{BD})^{1/3}$$

where D_{BD} and D_{ND} are the grain sizes in the BD and ND cross-sections, respectively. It is observed (Table 1) that by increasing the LSS, the average grain size decreases from 136 µm for the samples printed with 850 mm/s LSS to 51 µm for the samples manufactured with the LSS of 1300 mm/s.

Table 3 Diameter of grains at ND and BD cross-sections, and average grain diameter at different LSS values

Laser scanning Speed (mm/s)	D_{ND} (µm)	D_{BD} (µm)	$D_{Average}$ (µm)
850	169.5	87	136
1150	95.2	41.5	72
1300	59.1	38	51

Yield strength (YS) and other mechanical properties could be related to the grain size via Hall-Petch relationship:

$$YS = \sigma_i + kD^{-0.5}$$

where σ_i is friction stress which represents the overall resistance of the crystal lattice to movement of dislocations and is related to the strengthening mechanisms such as solid solution strengthening and precipitation hardening, k is the locking parameter which demonstrates the relative hardening influence of grain boundaries and D is average grain diameter [43]. The results of fitting Hall-Petch relationship to the observed experimental values of the current study are shown in Figure 49 (d). For pure nickel, the friction stress and locking parameters have been reported to be 20 MPa and 0.16 MPa.m0.5, respectively [133,134], which are significantly lower than the parameters calculated in this study, i.e., 365 MPa for σ_i and 0.88 MPa.m0.5 for k. Higher Hall-Petch coefficients of HX in comparison to pure nickel is obviously related to the effect of alloying elements. In other words, there are two important facts, which need to be taken into consideration here. Firstly, higher values of friction stress (σ_i) for the LPBF-made Hastelloy X parts is related

to the super-saturated Ni-base γ matrix generated by solute trapping of alloying elements during rapid solidification of the LPBF process [36,37,135]. A higher friction stress shows that solid solution strengthening is the major strengthening mechanism in the LPBF-made HX parts. On the other hand, the locking parameter of the alloy is higher than the pure nickel, which shows the effectiveness of grain boundaries in making dislocations movements more difficult and its additional increase of strength in comparison to the solid solution strengthening. Moreover, the locking parameter is higher than the severely deformed C-2000 Nickel alloy [134], which means that in as-built samples fine cellular structure and high dislocation density or high residual stress are acting synergistically to yield at high strength. Secondly, it could be concluded that the match with Hall-Petch relationship ($R^2 = 0.99$) is an indicator that the major strengthening mechanisms are solid solution strengthening and the grain boundary effect. It is more validated by the fact that other common strengthening mechanisms such as precipitation hardening are not present in Hastelloy X due to lack of precipitate forming elements such as Al and Ti [21,24,25]. It should be noted that the effect of solid solution strengthening is similar in the samples tested in the low porosity range and the main difference between these samples is the grains size. Moreover, this match could be due to a low number of data points, which have been used for fitting the Hall-Petch to the grain sizes of this study. Similar results have been obtained for pure iron samples produced by LPBF [130], where the effect of grains size was more significant than other strengthening mechanisms.

4.3.5 Fracture Surface

Figure 50 shows the fracture surface of the as-built samples manufactured with different LSS after tensile tests. The fracture surface of the samples fabricated by LSS of 550 mm/s shows keyhole porosities (Figure 50 (a), (b)). Insert of Figure 50 (a) shows the fracture surface of the sample at a higher magnification displaying pores coalescence. This phenomenon will increase the rate of cross-section reduction and local stresses simultaneously. Both of these effects will lead to a low ductility and low strength at the speed of 550 mm/s, since strength is calculated based on the assumption of defect free cross-section. The stress concentration near the pores and thin walls between them will result in stress triaxiality [43,121] and severe local deformation (Figure 50 (b)). Therefore, a premature necking or low elongation occurs at very high or low LSS values as shown in Figure 48.
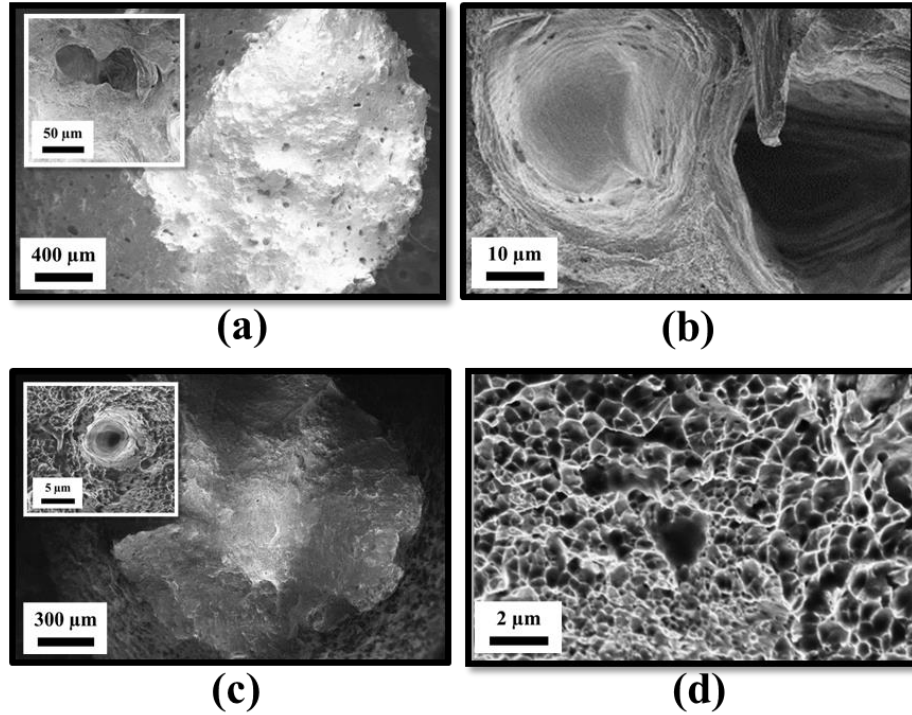
Figure 50 Fracture surface of the tensile samples manufactured with (a), (b) 550 showing the keyhole porosities and void coalescence; and (c), (d) 850mm/s showing a gas porosity surrounded by dimple (c) and dimple-like fracture surface morphology of ductile fracture (d).

High elongation to fracture in nearly full dense parts (produced by 850, 1150 and 1300 mm/s) was found to be associated with the necking behaviour and cup and cone fracture. The observed fracture surface for all three samples was covered with dimples, an attribute of ductile fracture (Figure 50 (d)). The insert of Figure 50 (c) shows a gas porosity surrounded by a dimpled fracture surface. The size of the dimples, which are formed due to micro-void coalescence, is less than 2 µm, while the gas pores are around 8 µm in the sample produced by LSS of 850 mm/s; both of which are far away in size from 50-70 µm keyhole pores in fracture surface of the 550 mm/s sample.

The fracture surface of the 1150 mm/s sample, Figure 51 (a), is similar to the 850 mm/s sample with larger size pores as shown in Figure 51 (a) insert. Figure 51 (b) shows the fracture surface of the 1300 mm/s sample, where the small LoFs and unmelted particles are highlighted by blue arrows in the insert. Due to the excessive LoF, 2050 mm/s samples show unmelted particles and unmelted regions (as shown in the insert) at the fracture surface (Figure 51 (c)). These unmelted regions are formed due to insufficient heat flux for remelting of the previous layer and indicate that the

successive layers are not well-bonded to the prior ones, leading to the reduced load-bearing capacity observed in the uniaxial tensile results (Figure 51 (c)). In addition to that, the irregular shape and large size of LoF defects increases the stress concentration factor and the premature failure, which result in a sharp decrease in the fracture strain and UTS (Figure 48).
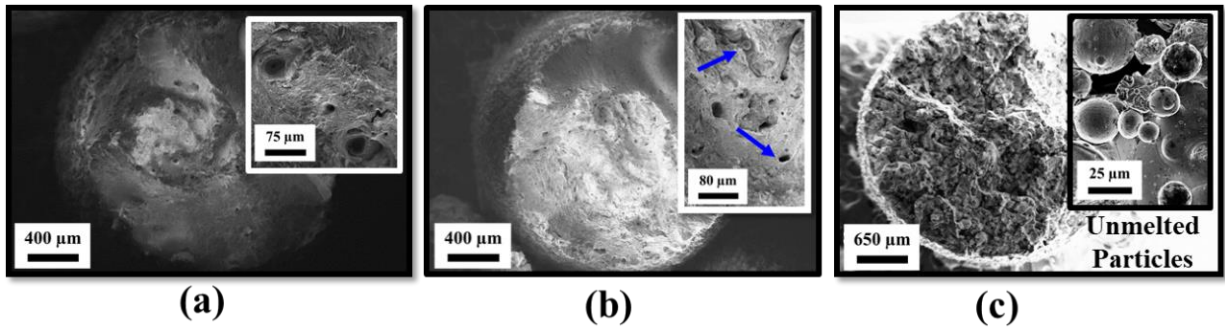
Figure 51 Fracture surface of the tensile samples manufactured with (a) 1150, showing similar morphology to 850; (b) 1300 showing presence of unmelted particles and small Lof depicted by blue arrows; and (c) 2050 mm/s showing excessive Lof and unmelted particles on the fracture surface.

4.4 Conclusion

In this study, the effects of laser scanning speed (LSS) on the microstructure and quasi-static uniaxial tensile properties of Hastelloy X samples manufactured by LPBF were investigated. The important conclusions are as follows:

1- No major porosities were observed in the 850, 1150 and 1300 samples while keyhole and lack of fusion porosities were observed in the 550 mm/s and 2050 mm/s samples, respectively. Compared to samples with highest strength (1300 mm/s) presence of keyhole (550 mm/s) and lack of fusion (2050 mm/s) resulted in reduction of UTS by 12% and 35% respectively. Similarly, compared to the sample with highest ductility (850 mm/s), 550 and 2050 mm/s samples show a reduction of 26% and 88% respectively.

2- A decrease in the average grain size from 136 to 51 µm is observed in the samples printed with the LSS of 850 mm/s and 1300 mm/s respectively. This resulted in an increase in mechanical strength due to grain refinement caused by smaller melt pools and an increase in partially melted particles (PMP).

3- Analysis of pole figures obtained from the ND cross-section of 850, 1150 and 1300 mm/s samples shows random texture due to the rotation of laser scanning vectors and presence of PMPs. Rotation of laser scanning vectors results in the change of in-plane heat flow direction in each successive layer while PMP particles introduced new random orientations during solidification.

4- Grain size results show that the yield strength can be predicted as a function of the grain size by using the Hall-Petch relationship. This is due to the solid solution strengthening and grain refinement observed in the as-built LPBF-made HX samples. However, this is not applicable for samples with keyhole and lack of fusion defects.

Chapter 5

5 On the Effect of Laser Powder-Bed Fusion Process Parameters on Quasi-Static and Fatigue Behaviour of Hastelloy X: A Microstructure/Defect Interaction Study

5.1 Introduction

Additive manufacturing (AM) provides a unique design freedom for engineers and material scientists [6,136]. In the laser powder-bed fusion (LPBF) process the fast heating and cooling rates result in non-equilibrium microstructure and control the local and global texture and grain structure of the sample [32,131,137]. However, LPBF parts may be susceptible to manufacturing defects [61,115,138,139] where these defects can drastically affect the part performance under real-life applications [140,141]. The defects can be controlled and minimized by process parameter optimization to achieve defect-free parts [142,143]. Furthermore, the process parameter optimization can facilitate the fabrication of defect-free parts with anisotropic mechanical responses [144,145]. Hence, a thorough investigation of mechanical properties is indispensable before adapting LPBF parts for real-life load carrying applications.

LPBF samples exhibit superior quasi-static strength compared to the conventionally manufactured (CM) samples that could be attributed to the non-equilibrium resultant microstructure [146,147]. High dislocation density and fine cellular solidification structure of as-built LPBF samples are the main reasons for higher yield strength compared to CM samples under quasi-static loading [41,148]. Moreover, Montero-Sistiaga et al. [149] observed a significant reduction in elongation due to carbide formation while testing LPBF-HX at 750 $^{\circ}$C and the effect of heat treatment on the decreasing the decay of the high temperature elongation. Tomus et al. [150] reported that the cracking propensity of the LPBF-HX is indeendant of the Mn concentration while the cracking propensity could be decreased by lowering the percentage of Si and C. It should be mentioned that the cracking in the as-built samples is highly dependent on the powder supplier (powder chemistry), the equipment used, and the selection of the process parameters. However, the manufacturing defects (relatively high surface roughness and porosities) can affect the tensile behaviour. Rosenthal et al. [151] have shown that a high surface roughness will not change the

strength, however, it can reduce the fracture strain whereas the uniform elongation remains unchanged. A similar effect has been reported by Fadida [152,153] indicating that the source of such anomaly is internal porosities with different sizes. Also, the anisotropic properties of the samples printed in different orientation are inherent to the LPBF process and is a direct result of directionally built microstructure [145,154]. Resultant anisotropy is a major challenge while dealing with complex parts where the local mechanical properties would be different. Although the quasi-static performance of the LPBF-made coupons shows promising results, most of the mechanical failures in components and structures are due to fatigue [155]. Therefore, investigating the part performance under fluctuating loads is a crucial step before the wide acceptance of LPBF-made parts in industrial applications.

The literature on fatigue performance of LPBF samples covers various aspects, e.g. effects of porosities, surface roughness, part orientation, and heat treatment [156–159]. Significant features of these samples affecting the fatigue response are distinct in high cycle fatigue (HCF) and low cycle fatigue (LCF) regions [14,46,160]. In the LCF regions, plasticity and induced damage due to cyclic hysteresis play an important role. Leuders et al. reported that heat treatment reduces LCF response by reduction of the material's strength and increasing the induced plasticity [49]. On the other hand, defects such as porosities and surface roughness due to their stress riser effects are dominant in HCF [161–163]. It has been shown by Ellyson et al. [164] that hot isostatic pressing (HIP) increases the HCF life significantly due to pores elimination. There have been some investigations on the fatigue behaviour of LPBF-HX. Wang et al. [12,165] studied the effect of part orientation on the four-point bending fatigue tests and observed similar behaviour in vertical and horizontal samples. Han et al. [48] investigated the effect of hot isostatic pressing (HIP) on the room temperature fatigue behaviour of HX after machining. They reported that HIPed samples have superior fatigue performance compared to the as-built samples, due to the closure of internal porosities and residual stress relief. Montero-Sistiaga et al. [166] tested the micro-crack free Hastelloy X flat machined samples under reverse loading condition and observed a large scatter in the experimental fatigue lives due to presence of lack of fusion defects.

Lack of systematic analysis on the fatigue response of as-fabricated LPBF parts with different manufacturing parameters in the optimized process window has led to the current investigation. Most of the fatigue studies on LPBF-made samples have been performed under a single set of

processing conditions [16,167] or in a way, in which sample internal/external defects are not comparable [46,168]. This study aims to investigate the effect of process parameters on fatigue behaviour of as-built Hastelloy X (HX) LPBF-made parts without any post-processing (surface or heat treatment). Two LPBF conditions with high and low laser scanning speeds are selected in the optimum process window based on a previous study by the authors [144]. These process parameters resulted in samples with the same porosity level (nearly full-dense parts) but a distinct tensile response which is due to the difference in the microstructure. Stress-controlled fatigue tests under axial load have been performed on the samples at various stress levels to cover both HCF and LCF regions. Stress-strain response was measured throughout the tests to obtain transient and stabilized behaviour. Also, microstructural and fracture surface investigations, as well as porosity and surface profile measurements, were made to characterize the failures in LCF and HCF regions. Finally, a correlation between the process parameters and the fatigue life is established that can be utilized for AM design.

5.2   Material and Experimental Procedure

5.2.1   Sample Fabrication

EOS Hastelloy X gas-atomized powder (Table 4 [131]) with a $D_{10,}$ $D_{50,}$ and D_{90} of 15.5 µm, 30 µm and 46.4 µm respectively was used with EOS M290 laser powder-bed fusion system to fabricate test samples under argon atmosphere with the build plate temperature of $80^{o}C$.

Table 4 Nominal chemical composition (in wt.%) of Hastelloy X gas-atomized powder used for LPBF.

Ti	Al	Cu	Mn	Si	C	Co	W	Mo	Fe	Cr	Ni
<0.15	<0.5	<0.5	<1	<1	<0.1	1.5 ± 1	0.6 ± 0.4	9 ± 1	18.5 ± 1.5	21.75 ± 1.25	balance

Samples with the same geometries were used for both tensile and fatigue testing (Figure 52a). Process parameters were selected based on the authors' previous study [144] and are shown in Table 5. Samples were manufactured vertically where the loading direction in mechanical testing was the same as the building direction. Samples with higher LSS are called H-LSS and the other samples are called L-LSS, hereafter.

Table 5 LPBF process parameters used for printing tensile and fatigue samples.

Parameter	Sample ID	
	L-LSS	H-LSS
Laser Power (W)	195	195
Laser Scanning Speed (mm/s)	850	1150
Hatching Distance (mm)	0.09	0.09
Layer Thickness (mm)	0.04	0.04
Scanning Strategy	Stripes with 67º Rotation	Stripes with 67º Rotation

5.2.2 Microstructure and Fracture Surface Characterization

Cross-sections were taken from the testing coupons before mechanical testing and cross-sections perpendicular to building direction (BD) are called BD and cross-section parallel to the BD is called normal direction (ND). Standard metallographic grinding and polishing procedures were followed using progressively SiC grinding papers from 80 to 2500 grit sizes then for the final polishing 1 to 0.05 µm alumina slurry was applied. Electron backscatter diffraction (EBSD) analysis was performed by JEOL7000F scanning electron microscope (SEM) with an Oxford EBSD detector for microstructural investigations. For EBSD data collection and post-processing AZtecHKL software and HKL Channel 5 software were used. Fracture surface investigations were performed using TESCAN VEGA3 scanning electron microscope (SEM).

5.2.3 Mechanical Testing

Quasi-static tensile and fatigue testing were performed by the Instron 8872 servo-hydraulic machine under standard laboratory conditions. Tensile tests in the displacement control mode with the cross-head speed of 0.45 mm/min were performed according to the ASTM E8 standard [114] and repeated for three samples at each manufacturing condition. For the strain measurements, Instron 2630-120 extensometer with 50% strain limit was utilized. Tension-Tension fatigue experiments were performed under stress (load)-controlled conditions with stress ratio, $R = {S_{min}}/{S_{max}} = 0.1$, where S_{min} and S_{max} are minimum and maximum stresses, respectively [169].

Randomized sample selection and testing sequence were followed to avoid bias in the experimental results. Three replicates were tested at each stress level for repeatability and statistical analysis for each manufacturing condition. Therefore, 12 samples for each LSS (total of 24 samples) were tested to obtain the finite life fatigue curve. Two stress levels, i.e. $S_{max} = 550$ and 625 MPa were selected to cover the LCF region of the stress-life (S-N) curve and two S_{max} levels below the yield stress, $S_{max} = 350$ (~75% of the YS) and 200 (~45% of the YS) MPa, were chosen to study the fatigue response in HCF region. A test frequency of 0.1 Hz was used for capturing the primary transient behaviour and then increased to 10 Hz until the final fracture. An Instron 2620-603 extensometer with 10% strain limit was used for strain measurement in fatigue tests. The Locati step-loading method with progressively-increasing loads [170,171] was used to obtain the fatigue limit. In the step-loading procedure, the specimen should not fail at 10^7 cycles for selected initial stress. After the first 10^7 cycles, stress was raised to the next level by the stress step of 20 MPa while maintaining the constant stress ratio (R). This procedure is repeated on the same specimen until failure occurs as shown in Figure 52. The step-loading test procedure was performed on five samples with test frequency of 50 Hz in each of the H-LSS and L-LSS manufacturing conditions (total of 10 samples) and the initial stress for the following samples was selected by two stress steps below the failure stress of the preceding samples. The fatigue limit at 10^7 was then determined by [172]:

$$S_e = S_0 + \Delta S \times \frac{N_{FB}}{N_R}$$

<div align="right">Equation 15</div>

where S_e is the fatigue limit (MPa), S_0 is the maximum stress of the loading block prior to the failure block, ΔS is the stress step, N_{FB} is the number of cycles in the failure block and N_R is the defined cyclic life (10^7 in the current study).
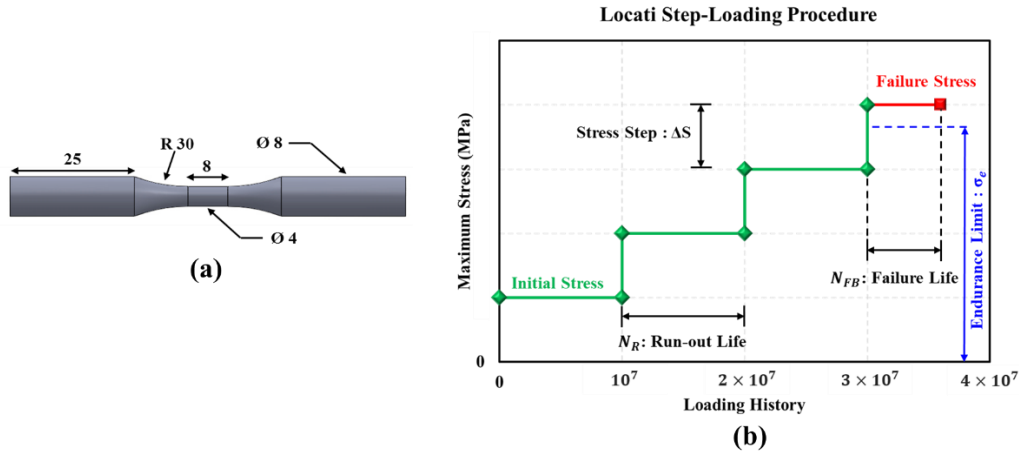
Figure 52 (a) Sample geometry used for the tensile and fatigue tests [144] (b) Schematic diagram of the Locati Step-Loading procedure.

5.2.4 Density and Surface Profilometry

The as-built cylindrical gauge length (Figure 52a) parallel to the building direction was characterized via laser confocal microscopy (Keyence VKX250). Scanning lines of ~1500 μm were scanned for every part, using a z-axis resolution of 1 μm.. The surface profile was measured at multiple sections near the middle of gauge length. The surface profile for each sample was measured at three different locations by rotating the sample by 120° to offset any effects of the surface orientation with respect to the powder recoating or gas flow directions and R_v which is the maximum profile valley depth along the sampling length was extracted for each measurement. To study the porosity distribution, ZEISS Xradia 520 Versa X-ray computed tomography (CT) was employed on the gauge length of 3 mechnical coupons at each manufacturing condition by scanning 801 2D projections at 10 W, 160 kV with an exposure time of 1 s at a resolution of 10 μm. Commercial software Dragonfly 3.1 was used for analyzing the 3D reconstructed images [115].

5.3 Results and Discussion

5.3.1 Microstructural Investigations

Rapid thermal cycles and high remelting/resolidification of previously solidified metal during depositing successive layers result in non-equilibrium microstructures in as-built LPBF structures [144,145,147,173]. As shown in Figure 53, columnar grains elongated along the building direction

are the consequences of epitaxial growth from the solidified substrate and directional heat flow because of the heat sink effect of the substrate [147]. Keshavarzkermani et al. [131] have shown that cellular solidification structures exist inside these columnar grains due to the high cooling rate. Three-dimensional representation of the microstructure reveals different grain morphologies (columnar vs. equiaxed) at different cross-sections (Figure 53). Similar grain morphology with columnar structure is observed in all the ND cross-sections due to the rotational scanning strategy. Sanchez-Mata et al. [174] have reported that the columnar grain morphology is sustained even after heat treatment at 1177 $^{\circ}$C for 1 hour. Figure 53 shows that by increasing the LSS, grain size has decreased due to the smaller melt pool size. A smaller melt pool (H-LSS: Width = 110 ± 5 µm, Depth = 60 ± 4 µm and L-LSS: Width = 127 ± 4 µm, Depth = 73 ± 3 µm [131,147]) confines the grain growth while the reduction in energy deposited at higher LSS results in a higher probability of partially melted particles (PMP) which act as inoculants during solidification resulting in a finer grain structure [131,144]. Generally, fine-grained alloys show superior performance under loading due to more restricted dislocation motion. Rotation scanning strategy alters the in-plane heat flow pattern in each successive layer. Therefore, it prevents the formation of a strong dominant crystallographic texture in the as-built condition [144].Comparing the BD and ND pole figures from the H-LSS and L-LSS samples shows lack of dominant texture component in the H-LSS sample due to the participation of more grains in pole figure construction (Figure 53).
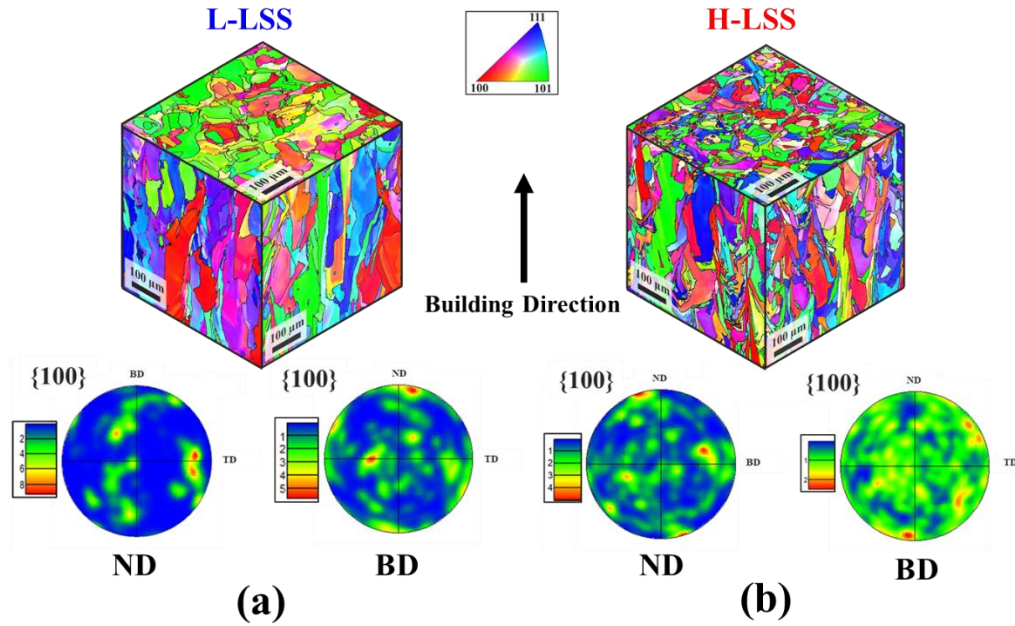
Figure 53 3D representation of the microstructure at different cross-sections and pole figures for different LSSs (a) L-LSS, (b) H-LSS showing columnar grain structure, and randomized texture.

5.3.2 Density and Surface Profilometry

Several studies have shown that the quasi-static behaviour of LPBF parts is not influenced by porosities and surface roughness (within a certain range) [153,175]. However, their effect on fatigue behaviour has been studied extensively by several researchers [158,161,162,168]. The density and roughness results of the samples manufactured with different processing conditions are shown in Figure 54. X-Ray CT results of the whole gauge length show similar porosity levels of these parts with different LSSs (Figure 54a). The pores are distributed uniformly throughout the height of the samples. Figure 54b shows the pore size distribution in the gauge length of the mechanical testing coupon. The results clearly show that altering the LSS does not result in a drastic change in overall porosities or their distribution. Therefore, any differences in the quasi-static or cyclic response observed between the H-LSS and L-LSS samples cannot be attributed to the porosity of the samples.
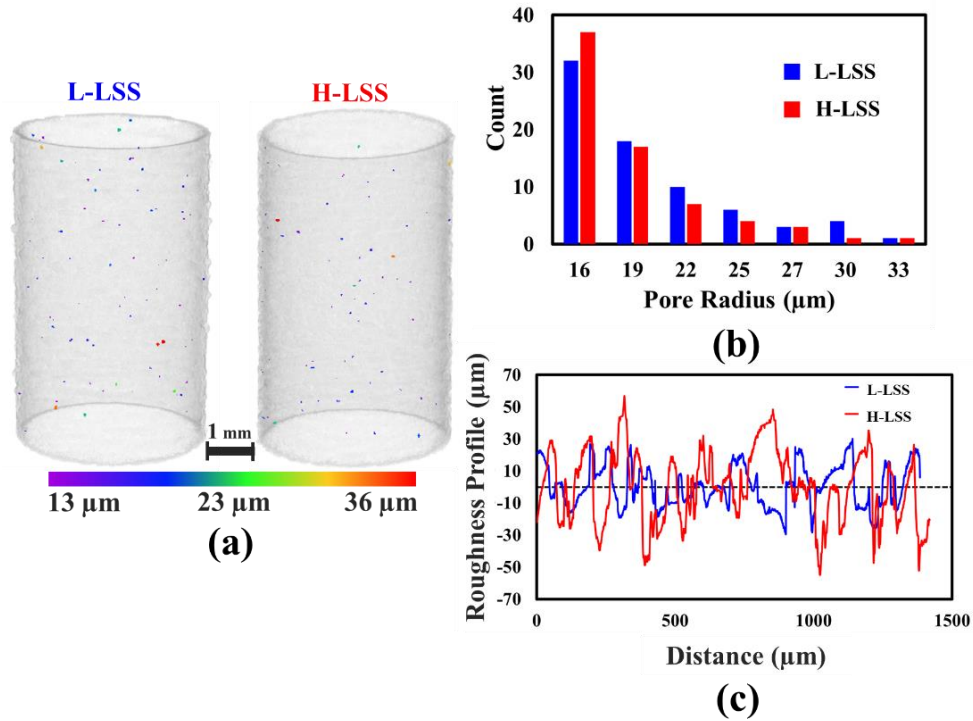
Figure 54 Porosity and surface profile measurements (a) X-Ray Computed tomography images showing pores distribution through the gauge length of the samples, (b) Pores size distribution and (c) Surface profiles of the as-built surfaces.

It is well known that surface roughness plays an important role in fatigue response, particularly in the HCF region [52]. Even starting from a smooth machined surface finish, the intrusions and extrusions can occur during cyclic loading, which leads to fatigue crack initiation due to stress concentration and excessive slip activity at their tips [121,176]. The surface finish of the LPBF parts in the as-fabricated condition is comparable to the sand cast samples and inferior to the machined and post-processed conditions [177,178]. The surface profiles of the samples printed with different LSSs are shown in Figure 54c. Powder-bed particles are carried out toward and attach to the tail of melt pools, while the part is buried in the surrounding powder-bed, by the argon flow from the inlet or by the inward gas flow associated with vapor jet due to the Bernoulli effect [115,131] and form partially fused particles (PFPs) to the surface. These PFPs attach to the surface and prevents the formation of a smooth surface finish of the LPBF parts [179]. Results in the literature show that increasing the LSS leads to higher surface roughness [180,181]. Figure 54c illustrates that the surface profile of the L-LSS sample is smoother than the H-LSS sample with shallower valleys. The waviness of the surface profile is decreased by decreasing the LSS. In

75

addition, the depth of deepest valleys, R_v, in the H-LSS and L-LSS samples was found to be 55 ± 5 µm and 30 ± 4 µm respectively. Therefore, a higher stress concentration is expected for samples printed with higher laser scanning speed due to deeper surface valleys.

5.3.3   Quasi-Static Response

The engineering stress-strain curve of the tensile coupons is shown in Figure 55a. Samples printed with H-LSS demonstrate higher yield strength (YS) and ultimate tensile strength (UTS) than the L-LSS samples. As shown in Figure 53, this difference is related to the finer grain size of the samples manufactured with the higher LSSs [40,144]. A smaller grain size due to H-LSS results in superior YS according to the Hall-Petch relationship. In other words, in solid solution strengthened alloys, such as Hastelloy X, grain boundaries can act as an extra strengthening mechanism by retarding the dislocation movement at room temperature [144]. As shown by other researchers [152,182], while investigating the samples in nearly full dense process window, the effects of defects such as porosity and surface roughness on the tensile response are negligible. It should be noted that the YS of nearly full dense LPBF samples is higher than conventionally manufactured (CM) Hastelloy X, 440 MPa for L-LSS and 470 MPa for H-LSS vs. ~350 MPa [183], respectively.
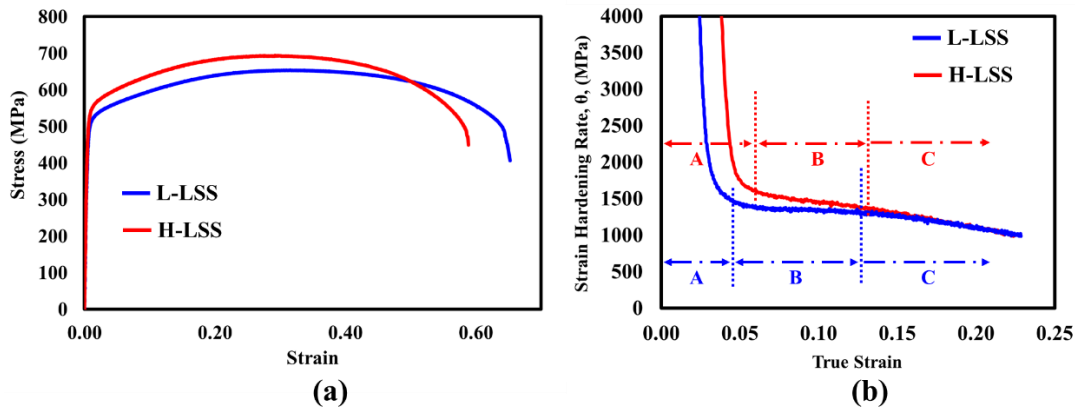
Figure 55 Quasi-static tensile response (a) Engineering stress-strain curves and (b) Strain hardening rate variation by true strain.

Figure 55b shows the corresponding strain hardening rate (θ) vs. true strain responses of the tested samples at different LSSs. For face-centered cubic (FCC) alloys with medium stacking fault energy (SFE) such as Hastelloy X and IN625, the strain rate hardening curve consists of four

different stages, i.e. A, B, C and D as discussed by Behjati [184] and captured in compression testing. In the present study (Figure 55b) stage D was not observed because of the necking in the sample and non-uniform strain distribution in the gauge length. A similar behaviour has also been observed in stainless steel 316L [185] due to twinning because of its low SFE. Cross-slip of dislocations could be the main reason for the decrease in the strain hardening rate during stage A. The initiation of stage B is the result of Lomer-Cottrell (LC) locks for medium SFE superalloys [184]. By further straining of the sample, dislocation density is increased with more possibility of formation of Lomer-Cottrell (LC) locks. These LC locks prevent the glide of mobile dislocations and this hinders the falling trend of the strain rate hardening. By receiving high enough stress at higher strains through further deformation, these partials can overcome the barriers, such as the lattice frictional stress and the LC locks, resulting in a reduction in θ (stage C).

Finer grain size, obtained at lower laser energies in the current study, lead to higher overall strain hardening rates of the H-LSS samples (Figure 55b). The commencement of stage B for H-LSS samples happens at higher θ because smaller grains increase the possibility of dislocations-dislocations and dislocations-grain boundaries interactions resulting in a higher strain hardening rate [186]. Although the strain hardening rate is not changing significantly in stage B, it is still higher for the samples with smaller grains, i.e. H-LSS. LC locks which are the main reason for stage B in HX are confined to individual grains. Hence, by reducing the grain size in H-LSS samples, the density of LC locks increases. Therefore, in stage B samples manufactured with higher LSS show higher strain hardening rates. Although grain size has a significant effect on stage A and B of strain rate hardening curves, stage C is almost independent of the grain size. When the available stress for partials is high enough to pass the obstacles (stage C), the density of these obstacles (LC locks) is not an influential factor for determining the unlocking rate and therefore the effect of grain size diminishes as seen in Figure 55b.

5.3.4 Fatigue Response

5.3.4.1 Ratcheting Behaviour

Cyclic stress-strain responses of the H-LSS and L-LSS samples are shown in Figure 56 at different stress levels. The most prominent behaviour in stress-controlled cyclic tests with tensile mean stress is cyclic creep or ratcheting [187]. The accumulation of directional progressive plastic strains while loading under primary load (mean stress) along with secondary cyclic load is called

ratcheting [188]. Based on Figure 56b & c, the difference between the cyclic transient response of the samples printed with different process parameters is negligible in the absence of macro plastic deformation, i.e., when the $S_{max} = 200\ and\ 350$ MPa is lower than the yield strength (YS). The effect of process parameters on the transient behaviour becomes prominent when the maximum stress is beyond YS. At $S_{max} = 550\ and\ 625$ MPa the ratcheting strain is higher for L-LSS due to its larger grains and lower strength (Figure 56d & e). As it is visible in Figure 55a for the same stress level above the YS, the L-LSS sample shows larger strains in comparison to H-LSS sample and this difference becomes larger when comparing 550 with 625 MPa maximum stress levels (Figure 56a). It should be noted that during the first loading reversal, the amount of induced plastic strain in the sample with larger grains (L-LSS) is larger than the H-LSS sample with finer grains; hence, during the cyclic loading the stress-strain hysteresis stabilizes at larger strains. Figure 56 also shows the hysteresis at the half-life (dashed line hysteresis) and the accumulation of strains due to cyclic loading lead to hysteresis shifts at each successive cycles while being loaded above the YS. It is evident from Figure 56b that the ratcheting rate progressively decreases, which is related to cyclic hardening as the transient cyclic response [189,190]. Both L-LSS and H-LSS samples show the cyclic hardening behaviour under the experimental conditions of the current study.
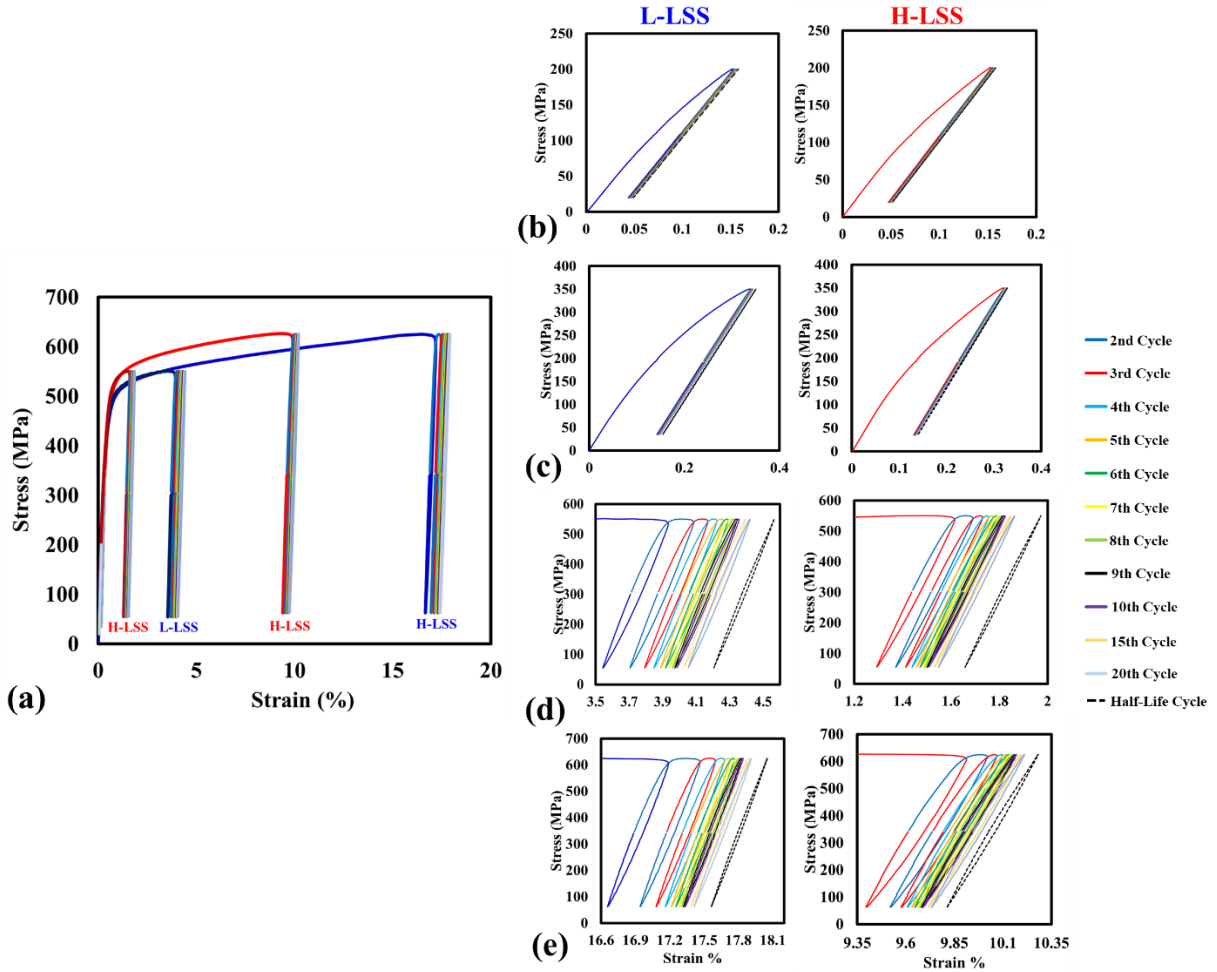
Figure 56 (a) Transient stress-strain curves for samples tested at different stress levels and LSSs for the first 20 loading cycles and Ratcheting behaviour and half-life hysteresis loops for different maximum stress (b) 200, (c) 350, (d) 550 and (e) 625 MPa.

5.3.4.2 Stress-Life (S-N) Curve

Figure 57a presents the relationship between the maximum applied stress (S_{max}) and the number of cycles to failure (N) or the S-N diagram for the H-LSS (YS = 470 MPa) and L-LSS (YS = 440 MPa) samples. Two stress levels were selected above the YS values, i.e., 550 and 625 MPa to impose plasticity in each cycle while being lower than the UTS to avoid necking in the first cycle. These high S_{max} values were expected to result in lives lower than 10^5 or be in the LCF region. The lower stress levels are selected below the YS values, i.e. 350 and 200 MPa. At these stress levels gross plastic deformation of the whole gauge length is prohibited resulting in higher cycles to failure in the HCF region.

79

As shown in Figure 57a, the H-LSS and L-LSS samples show different behaviour at high and low-stress levels. At high-stress levels (LCF), L-LSS samples show lower lives than the H-LSS samples, but at lower stress levels (HCF), L-LSS samples show higher lives. This observation demonstrates the effect of manufacturing processing conditions on the fatigue behaviour of LPBF samples. Based on the process parameters selection, the fatigue response can be altered when the superior performance of one set of process parameters, e.g., the H-LSS samples in the LCF region, does not guarantee any effective results at HCF in comparison to the other process parameters (L-LSS). On the other hand, this investigation shows the process parameters can be tuned for certain HCF or LCF applications and parameter selection should be based on application requirements and the LPBF process knowledge.

At each stress level, a single factor (LSS) analysis of variance (ANOVA) was performed with a significance level (α) of 0.05 using MATLAB$^®$ to study if the LSS affects (p-value $< \alpha$) the fatigue life. The ANOVA tables are shown in

Figure 57b where SS, df, MS, F and P are the sum of squares, degrees of freedom, mean square, F-statistic and p-value, respectively. Results from ANOVA analysis show that the p-value for 200, 350 and 625 MPa is lower than 0.05 which suggests that the LSS affects fatigue life significantly. However, at 550 MPa, a p-value > 0.05 is observed. According to Figure 56a at 625 MPa stress level, the stress-strain hysteresis is stabilized at different strain levels for the H-LSS and L-LSS samples, ~10% and ~18%, respectively. This difference between the mean strains is high enough to cause a significant change in fatigue lives in the LCF region. Also, higher strains can be interpreted as higher pre-strain damage before cyclic deformation which can decrease the fatigue lives [191]. However, at 550 MPa the difference in the pre-strain damage of L-LSS and H-LSS samples is not high enough to cause a statistically meaningful difference between the fatigue lives for L-LSS and H-LSS samples as was shown in the ANOVA analysis.

ANOVA 200

Source	SS	df	MS	F	P
Columns	2.3E+12	1	2.3E+12	56.6	0.0017
Error	1.6E+11	4	4.1E+10		
Total	2.5E+12	5			

ANOVA 350

Source	SS	df	MS	F	P
Columns	9.9E+09	1	9.9E+09	35.4	0.0039
Error	1.1E+09	4	2.7E+08		
Total	1.1E+10	5			

ANOVA 550

Source	SS	df	MS	F	P
Columns	1.1E+06	1	1.1E+06	0.12	0.75
Error	3.7E+07	4	9.2E+06		
Total	3.8+E07	5			

ANOVA 625

Source	SS	df	MS	F	P
Columns	5.7E+07	1	5.7E+07	51.8	0.0019
Error	4.4E+06	4	1.1E+06		
Total	6.2E+07	5			
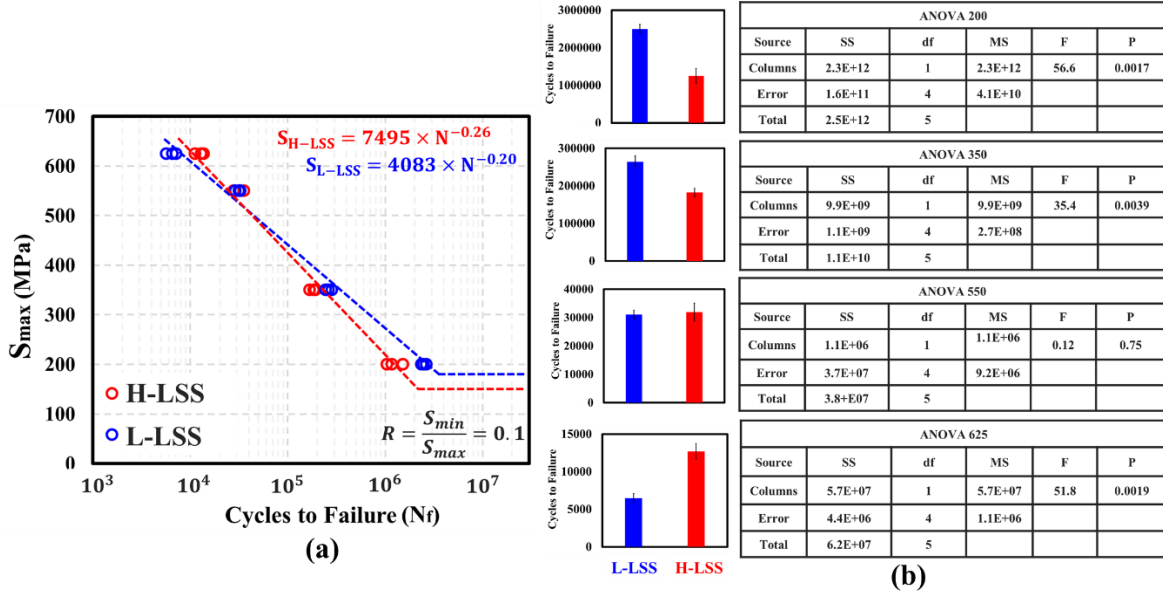
Figure 57 (a) Stress-Life curves for different manufacturing conditions and (b) Bar charts and ANOVA tables at different stress levels.

Basquin equation was fitted to S-N data excluding the run-outs ($N_f > 10^7$ cycles) to describe the stress-controlled fatigue life [192]:

$$S_{max} = \sigma_f' \times N_f^b$$

Equation 16

where N_f is the number of cycles to failure, σ_f' is the fatigue strength coefficient and b is the fatigue strength exponent. According to Equation 16, $\log(\sigma_f')$ and b are the intercept and the slope of the fitted line respectively when the S-N curve is plotted on a log-log scale. The Basquin model parameters have been summarized in Table 6. It is found that σ_f' and the slope of the H-LSS is higher than the L-LSS samples. Results in Figure 57a show a lower fatigue life for the H-LSS samples in the HCF region. This is the result of the sample surface profile as discussed in the Density and surface profilometry Section. The deeper valleys of the H-LSS ($R_v = 55 \pm 5$ µm) than the L-LSS ($R_v = 30 \pm 4$ µm) samples result in higher stress concentration values at the surface, which leads to shorter crack initiation lives for H-LSS in the LCF.

Table 6 Basquin model parameters for L-LSS and H-LSS samples for R=0.1.

Sample	Fatigue Strength Coefficient (MPa)	Fatigue Strength Exponent
L-LSS	4083	-0.20
H-LSS	7495	-0.26

5.3.4.3   *Fatigue Limit*

The 10^7 cycles fatigue limit of L-LSS and H-LSS samples were determined using Locati step-loading method [170] and the results of the testing sequence are shown in Figure 58. Application of the step-loading procedure shows consistent reliable results for the fatigue limit of superalloys due to the absence of coaxing or under-stressing effect of interstitials in these alloys [193]. The L-LSS samples show higher failure stresses. These results are in-line with the HCF results where the L-LSS samples exhibit a much better performance (Figure 57a). Lower surface asperities and the smoother surface of the L-LSS samples (Figure 54c) indicate less severe stress concentration of the surface valleys and higher fatigue life in the HCF tests.
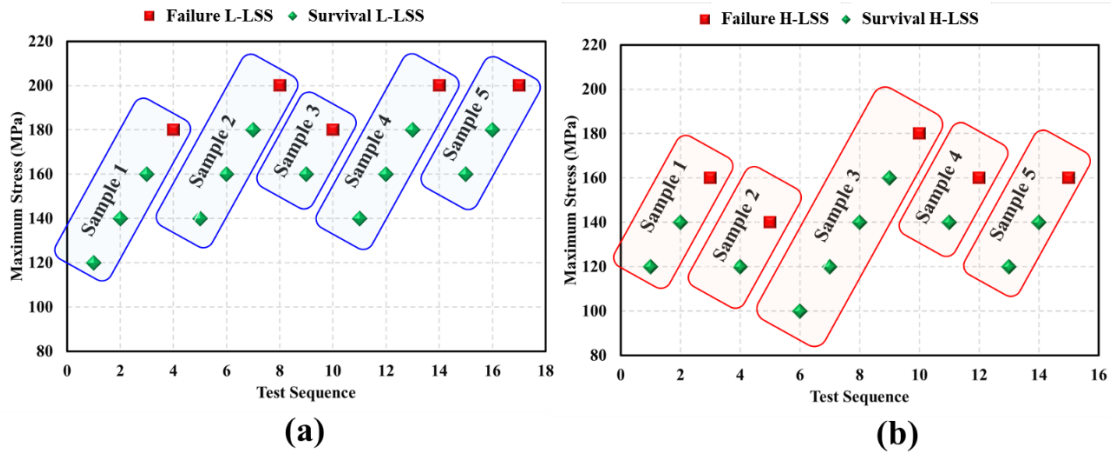
Figure 58 Step-Loading testing sequence of (a) L-LSS and (b) H-LSS samples.

Numerical results for step-loading tests are presented in Table 7. The average step-loading testing results of five samples for each of the L-LSS and H-LSS conditions are 180 ± 10 and 149 ± 11 MPa, respectively. These values have been shown by the horizontal line in

Figure 57a. As seen, the smoother surface of L-LSS samples led to ~20% increase in the fatigue limit.

Table 7 Fatigue limit step-loading results of Hastelloy X samples with different manufacturing conditions at R=0.1.

Specimen		Initial Stress (MPa)	Stress Step (MPa)	Failure Stress (MPa)	Failure Life	Fatigue Limit (MPa)
L-LSS	#1	120	20	180	6.1×10^6	172
	#2	140	20	200	2.1×10^6	184
	#3	160	20	180	4.2×10^6	168
	#4	140	20	200	8.5×10^5	182
	#5	160	20	200	6.8×10^6	194
H-LSS	#1	120	20	160	4.5×10^6	149
	#2	120	20	140	6.8×10^6	134
	#3	100	20	180	2.3×10^6	165
	#4	140	20	160	2.9×10^6	146
	#5	120	20	160	6×10^6	152

5.3.4.4 *Fracture Surface*

Figure 59 shows the fracture surfaces of the H-LSS and L-LSS fatigue samples at low magnification for different stress levels and the crack initiation, propagation and final fracture regions are shown in green, red and yellow respectively. Based on the fracture surfaces depicted in Figure 59, fatigue cracks initiate from multiple points on the surface of the samples at all stress levels. Ratchet lines (highlighted by R in Figure 59) are observed when fatigue cracks are initiated from different locations and the crack fronts meet one another. The several reports on the fracture surface of the LPBF parts have shown crack initiation from gas or lack of fusion porosities [46,50,160]. However, in the current study due to the selection of the process parameters in the nearly full dense process window, the volume fraction of porosities is minimal and the porosity effect on crack initiation is insignificant (Figure 60a). The dominant crack initiation sites are surface roughness valleys due to the stress concentration and their geometrical inhomogeneity [179]. It is well known that the final fracture occurs when the crack length reaches a critical value which is dependent on the stress intensity factor [194]:

$$K = Y\sigma\sqrt{\pi a}$$ Equation 17

where K is stress intensity factor, Y is the geometrical factor, σ is the applied nominal/remote stress and a is the crack length. During cyclic loading, as the crack propagates through the sample and reaches a critical value (a_C) the stress intensity factor also reaches a critical value (K_C) where the material does not tolerate any more crack propagation, resulting in final sudden failure. As all samples studied in this work have the same geometry, K_C and Y are considered constant. Therefore, for the same Kc and Y, it can be concluded that an increase in the applied stress would result in a reduction of the critical crack length a_C. An extreme case can be observed for the L-LSS sample at 625 MPa where virtually no crack propagation was observed and final fracture occurred right after crack initiation. This observation can be related to the different cyclic transient behaviour where the pre-strain damage in the L-LSS samples is larger than the H-LSS samples due to lower strength and larger grain size (Figure 53 and Figure 55).
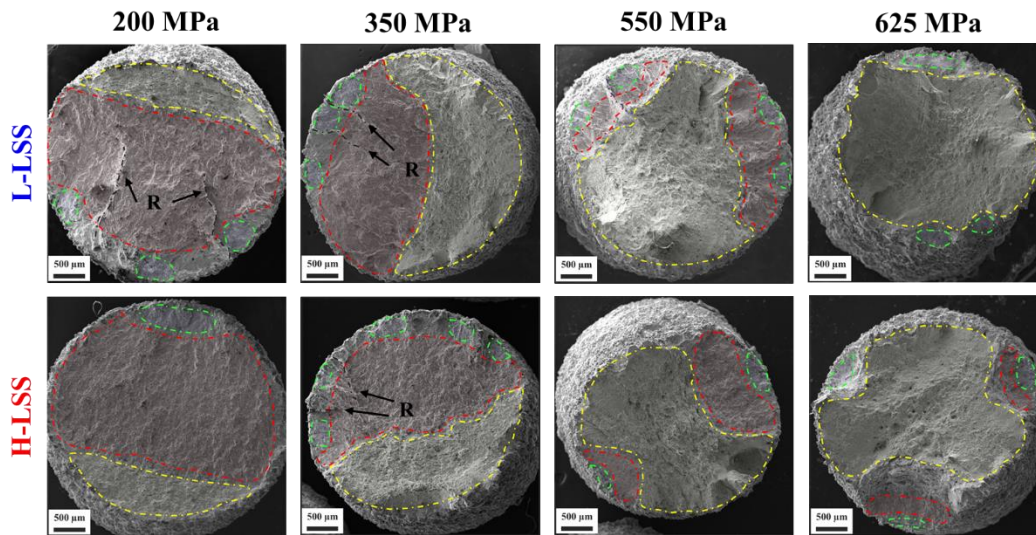
Figure 59 Fracture surface of the samples at low magnification showing different regions: Crack nucleation (green), Fatigue crack propagation (red), Final fracture (yellow), "R" denotes ratchet lines (R).

Figure 60 shows the fine features of the fracture surfaces to investigate various fatigue fracture stages and fatigue crack propagation rates. The dotted green line (Figure 60a) highlights the border between the load-carrying cross-section of the sample and surface roughness valleys at the fracture surface. Tear ridges pointing toward the crack initiation sites (blue arrows) have been highlighted by the orange arrows and show signs of excessive slip activities due to stress concentration at the root of roughness valleys which act as micro-notches. Figure 60a also demonstrates the fatigue

crack interactions with porosities (green arrows). It is observed that the fatigue crack crosses the gas porosities and did not initiate from them and/or interact with them. This observation confirms the dominant effect of surface roughness in comparison to as-built porosities in the fatigue crack initiation stage, within the scope of the current study. Striations due to fatigue crack advancement at each cycle are also observed (Figure 60b). Striation spacing is related to the applied stress range through stress intensity factor range by [121]:

$$\frac{da}{dN} \; \alpha \; \Delta K \qquad\qquad\qquad \text{Equation 18}$$

where $\frac{da}{dN}$ is crack growth rate representing striations spacing. SEM images of the fracture surface at high magnifications at the same crack length show that by increasing the applied stress (or stress intensity factor) the striation spacing is increased (Figure 60b) and this trend is similar for samples manufactured with different LSSs. Moreover, comparing the striations of the L-LSS and H-LSS samples shows that the crack growth rate is not affected by LSS and/or microstructure (Figure 60b). Various studies have shown that the effect of microstructure on fatigue crack is important when the crack length is in the range of microstructural features (grains) [195]. In the as-built surface conditions the depth of the valleys can reach up 50 µm (Figure 54c) and the resultant initiated crack can be considered as long crack where the effect of the microstructure is not dominant. Secondary cracks are initiated from the striations micro depressions where their propagation plane is normal to the fracture surface [196] as shown in Figure 60c. The final fracture region is characterized by the dimples similar to tensile samples [144].
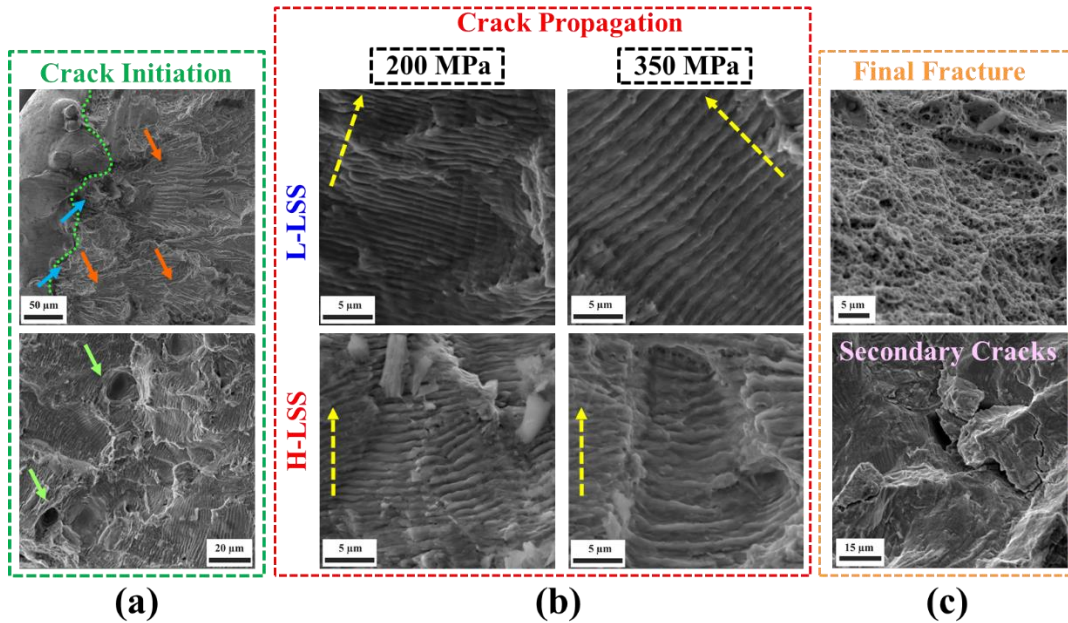
Figure 60 (a) Tear ridges (orange arrows) pointing toward crack initiation sites/surface valleys (blue arrows) and crack interaction with the porosities (green arrows), (b) Fatigue crack propagation and striations at different stress levels and LSSs (yellow arrows shows the crack propagation direction) and (c) Secondary cracks/Crack branching and final fracture region with dimples.

5.4 Conclusions

In the current work, quasi-static and fatigue responses of Hastelloy X samples manufactured by LPBF-AM were investigated and correlated to the printed samples features (microstructure and defects). The current study establishes a fatigue life – process parameter relationship for LPBF – HX. The most important conclusions are as follows:

1- LPBF manufacturing parameters directly affect the sample microstructure and defects in the nearly full dense process window. Samples produced by higher LSS, 1150 mm/s show smaller grain size and deeper surface valleys ($R_v = 55 \pm 5$ µm), in comparison to the L-LSS samples, 850 mm/s, ($R_v = 30 \pm 4$ µm) with no major difference in as-built part porosities.

2- Quasi-static tensile response of the H-LSS (YS = 470 MPa) samples is superior to the L-LSS (YS = 440 MPa) samples due to finer microstructure (with no major effect of porosity and roughness) resulting in a higher strain hardening rate (SHR) during initial loading.

3- In the LCF region, the microstructure is found to have a dominant effect. For the L-LSS samples with larger grains size, the hysteresis stabilizes at higher strains leading to higher pre-strain damage before the cyclic deformation resulting in lower fatigue lives.

4- Cyclic response of the LPBF samples in the HCF region confirms the effect of surface profile and surface valleys on the fatigue life. Deeper surface valleys in the H-LSS samples result in earlier crack initiation due to higher stress concentration. As the crack propagation rate is similar for two process parameter sets (microstructures), the earlier crack initiation leads to a lower total fatigue life of the H-LSS samples in the HCF region.

5- The Locati step-loading procedure revealed that the fatigue limit of the L-LSS sample (180 MPa) is ~20% higher than the H-LSS sample (149 MPa).

Chapter 6

6   Fatigue Characterization and Modeling of Additively Manufactured Hastelloy-X Superalloy

(Manuscript ready for submission)

6.1   Introduction

Laser powder-bed fusion (LPBF) is a class of additive manufacturing (AM) used to fabricate metallic parts where a thin layer of powder particles is spread on a substrate or powder-bed and selectively melted by a laser, based on a CAD model [6,148]. This procedure is repeated for consecutive layers until the completion of the component [60,61]. LPBFs flexibility and the large number of process parameters [142] open the possibility of part performance optimization for specific design requirements [144,197]. However, due to the rapid solidification and high temperature gradients [147,198] of the LPBF process, the material develops grains with elongated morphology in the building direction as a result of epitaxial grain growth [18,199]. This phenomenon gives rise to the anisotropic mechanical properties [145]. The high cooling rates lead to fast solidification of the molten metal and results in cellular structure inside the columnar grains [131,200].

Although AM offers the ability to fabricate highly-complicated parts [154,201–203], the uncertainty in their mechanical properties restricts the adoption of AM parts for real-life load carrying applications. Several process and design parameters involved in laser-based AM affect the part's features and performance and lead to a wide scatter and variation in their monotonic and cyclic response. Variation in these process parameters such as laser power [180], scanning speed [144], scanning strategy [145], hatching distance [142], part building orientation [161] and part location[115] result in parts with unique properties due to the as-built microstructure and defects. Defects such as gas and lack of fusion porosities [144,204], high surface roughness [115,116] and microstructural heterogeneities [145,205] also occur due to the selection of improper process parameters and affect the static and particularly the fatigue performance. Experimental investigations in the literature indicate that LPBF-HX specimens can match or surpass the mechanical properties of its wrought and cast counterparts under monotonic loading (e.g., tension, compression, hardness, etc.) due to the fine cellular solidification structure [17,151]. However,

since fatigue is the most common cause of failures in metallic components [43,206], it is crucial to study the cyclic response of LPBF specimens. Unlike sudden failure under monotonic loads, fatigue is a highly localized failure mode including crack nucleation/initiation, propagation and final fracture [121]. Various modeling approaches have been utilized for fatigue life prediction of LPBF specimens. Lee et al. [207] applied a stress-based and observed strong effect of surface roughness on the Basquin's model parameters, Romano et al. [208] used Coffin-Manson strain-based relationship and investigated the effect of process parameters on the model's coefficients and Branco et al. [209] investigated an energy-based model for fatigue life prediction of LPBF specimens using Ellyin's formulation and reported the total strain energy density yields reasonable fatigue life predictions.

A few investigations on the fatigue behavior of LPBF-HX are mostly conducted using force-controlled tests [12,48,159,165]. Wang et al. [12,165] studied the effect of part orientation on the four-point bending fatigue tests and observed similar behavior in vertical and horizontal specimens. Han et al. [48] investigated the effect of hot isostatic pressing (HIP) on HX's room temperature fatigue behavior of HX after machining. They reported that HIPed samples have superior fatigue performance compared to the as-built specimens, due to the closure of internal porosities and residual stress relief achieved through the HIP process. Recently, Lindstrom et al. [210,211] studied the strain-controlled response of LPBF-HX in order to construct a constitutive model for predicting the cyclic response. They observed that most of the fatigue life is spent in the crack nucleation and initiation in the investigated life span. The fracture surface of the horizontal specimens showed more plastic deformation compared to the vertical specimens. To the best of the authors' knowledge, there are no detailed reports and analysis on the strain-controlled low cycle fatigue (LCF) and high cycle fatigue (HCF) behavior of LPBF-HX in the literature.

In this work, the monotonic and cyclic deformation behavior of Hastelloy X (HX) manufactured by LPBF is studied followed by the fatigue modeling. The effect of loading direction on the quasi-static response was investigated under monotonic tension and compression loadings. Fatigue tests were performed under fully-reversed strain-controlled conditions, with various strain amplitudes (0.07 – 0.8 %). To characterize the material's behavior under cyclic loading, the stress-strain response was captured during the cyclic tests to analyze the transient behavior (cyclic hardening/softening). The cyclic stress-strain curve for LPBF-HX in as-built condition was

constructed based on the half-life stabilized hysteresis loops. Experimental cyclic results were used to model the fatigue response of LPBF-HX. Various fatigue modeling approaches including Basquin-Coffin-Manson (BCM), Smith-Watson-Topper (SWT), and Jahed-Varvani (JV) were calibrated and validated with experimental results. Finally, the BCM design curve was constructed with the Owen tolerance limit of 95% reliability and 90% confidence level (R95C90).

6.2 Methods and Materials

6.2.1 Specimen Fabrication

In the present study, EOS M290 laser powder-bed fusion system was employed to manufacture specimens under argon atmosphere with the build plate temperature of 80°C using EOS Hastelloy X powder with the particle size of 15-45 µm [115]. Specimens with the same geometries, shown in Figure 61(a), were used for both static tension and fatigue testing. Cylinders with 4 mm diameter and 8 mm height were used for static compression testing, Figure 61(b).
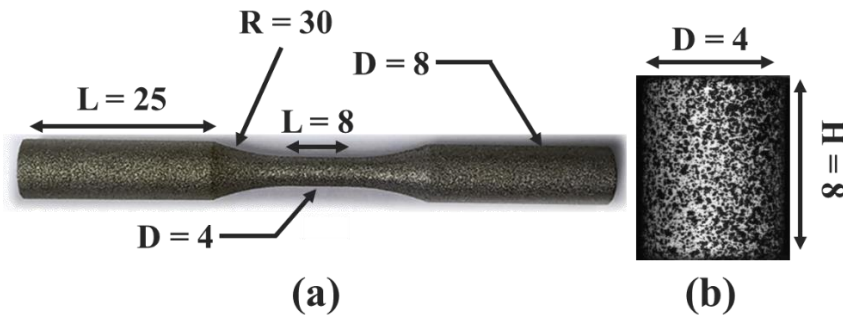
Figure 61: Specimen geometry for (a) static tension and fatigue tests, and (b) static compression tests (all dimensions in mm).

Process parameters were selected based on the authors' previous study [144] and are shown in Table 8. Specimens were manufactured vertically, using 67° rotation of the scanning vectors at each successive layer, where the loading direction in mechanical testing was the same as the building direction.

Table 8: Major LPBF process parameters used for printing tension, compression and fatigue specimens.

Laser Power (W)	Laser Scanning Speed (mm/s)	Hatching Distance (mm)	Layer Thickness (mm)
195	850	0.09	0.04

6.2.2 Mechanical Testing

Instron 8872 servo-hydraulic machine with a load capacity of ±25 KN was used for quasi-static tension and fatigue testing under standard laboratory conditions. Tension tests were performed according to the ASTM E8 standard [114] in the displacement control mode at the rate of 0.45 mm/min. An Instron 2630-120 extensometer with 8 mm gauge length and ± 4 mm travel was used for strain measurement in quasi-static tension and fatigue tests. GOM ARAMIS 3D digital image correlation (DIC) system with 5 megapixel image resolution and the maximum rate of 15 frames per second was employed for strain measurement during quasi-static compression tests. Before imaging, speckle patterns were painted on the specimens' gauge section, Figure 61b. Fully-reversed strain-controlled cyclic tests with strain ratio, $R_\varepsilon = {\varepsilon_{min}}/{\varepsilon_{max}} = -1$, as per ASTM E606 [212], were run at various frequencies between 0.2 and 2.6 Hz depending on the applied strain amplitude to keep the strain rate constant. When the maximum and minimum stress response reached stability at very low strain amplitudes, tests were switched to the load-control mode and continued at higher frequencies up to 20 Hz. Randomized specimen selection and testing sequence were followed to avoid bias in the experimental results. The run-out life was determined as 10^6 cycles. Four replicates were tested at each strain level for repeatability, statistical and reliability analyses. The fatigue failure criterion for the current study was considered the final rupture of the specimens.

Stress (load)-controlled fatigue experiments were performed in the author's previous investigation with stress ratio, $R_\sigma = {\sigma_{min}}/{\sigma_{max}} = 0.1$, where σ_{min} and σ_{max} are the minimum and maximum stresses, respectively, and further analyzed in the current study to validate the fatigue models. Three maximum stress levels (350, 550 and 625 MPa) were chosen to cover HCF and LCF responses in the presence of mean stress [213]. The stress-strain responses at the half-life cycle were utilized to calculate the fatigue damage parameters.

6.3 Results and Discussion

6.3.1 Quasi-Static Tension and Compression Response

Quasi-static tension and compression stress-strain curves of the LPBF-HX specimens are displayed in Figure 62a. This figure shows a similar elastic modulus, negligible tension-compression yield asymmetry and similar flow stress during the primary stage of the plastic deformation. Lack of ordered phases/precipitates in HX and therefore non-Schmid effects related to them could be a reason for similar yielding behavior in tension and compression [214]. The deviation from the symmetric behavior is observed at ~2-3% strain and continuously grows with an increase in strain. Rosenthal et al. [151] reported similar behavior for LPBF-HX. They explained the observed asymmetry by relating it to the weakening effect of voids/porosities under tension in comparison to compressive loading condition and the orientation of the fine cellular-dendritic microstructure. It should be noted that in strain-controlled fatigue tests conducted in this research the strain amplitudes are less than 1%; therefore the cyclic behavior is expected to be symmetric.
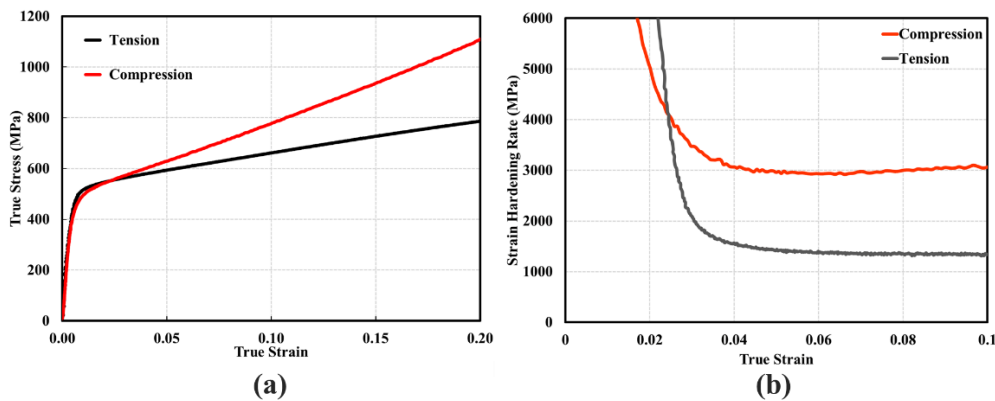
Figure 62: (a) Quasi-static stress-strain curves under tension and compression (b) Strain hardening curves for tension and compression.

The strain hardening rate response depicts higher values in compression than in tension (Figure 62b). A recent study by Chen et al. [215] has discussed the effect of residual stresses on the strain hardening rate asymmetry. It has been shown that the strain hardening rate is higher in compression than tension in the as-built condition [215]. The tension-compression asymmetry is generally associated with back stresses that stem from the heterogeneous dislocation cell structures found in

LPBF made HX [17,216] and other alloys such as Cu alloys [217], austenitic 316L stainless steel [218] and CM247LC Ni-Superalloy [219]. The heterogeneous dislocation cell structures induce intragranular internal stresses, including forward stresses in the hard cell walls with higher dislocation densities and back stresses in soft cell interiors [215]. Hence, the material shows dissimilar responses in different loading directions leading to higher strain hardening rates and flow stresses in compression. In the current study, the LPBF-HX specimens have been manufactured with minimum porosity (< 0.1%). Therefore the difference in the deformation behavior under various loading directions is believed to be attributed to the resultant heterogeneous dislocation structures and the associated internal stresses. Quasi-static material properties based on the Ramberg-Osgood equation can be expressed as [220]:

$$\varepsilon = \frac{\sigma}{E} + (\frac{\sigma}{K})^{\frac{1}{n}}$$
Equation 19

where n is the strain hardening exponent and K is the cyclic strength coefficient. The K and n values obtained for LPBF-HX are given in Table 9.

6.3.2 Cyclic Deformation Response

6.3.2.1 Transient Behavior

Figure 63 shows the variation of stress amplitude during strain-controlled fatigue tests at different strain amplitudes. Results show that the LPBF-HX specimens exhibit an increase in the stress amplitude at constant strain amplitudes commonly known as cyclic hardening, in the first few cycles of life at all strain amplitudes tested in the current investigation. Moreover, at higher strain amplitudes, i.e., ε_a =0.4% and 0.8%, the initial hardening is followed by continuous softening. Similar behavior has been reported for LPBF-HX recently [211] and conventionally manufactured HX [221]. According to Figure 63b, it is noticed that the amount of hardening is negligible at low strain amplitudes, e.g., ε_a =0.07%. Results show that the peak stress is achieved earlier with an increase in strain amplitude due to an increased dislocation activity.

The underlying mechanism for the transient cyclic hardening/softening behavior may be described according to the material and manufacturing process. In LPBF-HX, due to lack of precipitates, solid-state transformation and solidification cracks, the hardening and softening could be explained by dislocation interactions. Various transient responses of LPBF-HX observed in this

93

work could be attributed to the competition between dislocation annihilation and creation during damage accumulation. Cyclic hardening occurs when the rate of dislocation generation is greater than the rate of dislocation annihilation. On the other hand, cyclic softening occurs if the rate of annihilation is higher than the rate of dislocation creation [222]. Therefore, the initial cyclic hardening observed in LPBF-HX could be attributed to the higher rate of dislocation generation.
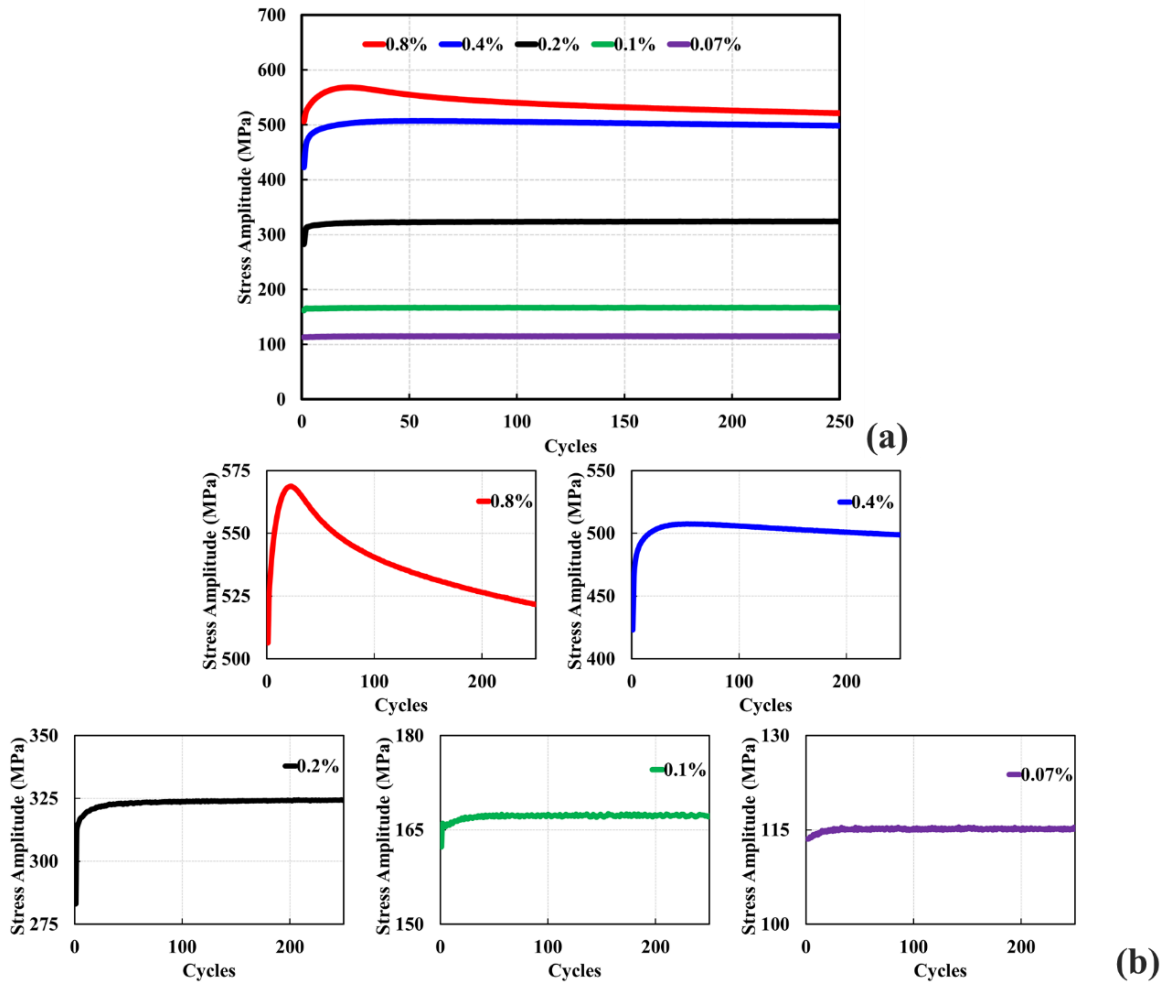
Figure 63: (a) Cyclic stress amplitude response of specimens tested at different strain levels, (b) Enlarged view of the stress response.

At higher strain amplitudes, the rate of dislocation generation is higher than the dislocation annihilation thus resulting in cyclic hardening. However, cyclic softening is observed at higher number of cycles due to a higher rate of dislocation annihilation due to forward and reverse glide

of dislocations in loading and unloading reversals of a complete fatigue loading cycle [223]. It is noted that, at lower strain amplitudes, cyclic stability is achieved within the first few cycles due to similar rates of dislocation annihilation and generation or purely elastic response. This investigation demonstrates that cyclic hardening/softening behavior of LPBF-HX not only depends on the material but also on the cyclic load level.

6.3.2.2   Stabilized Behavior

Stabilized half-life cycle stress-strain hysteresis loops are shown in Figure 64a at five different strain amplitudes. It is noted that the peak stresses and the shape of hysteresis loops are symmetric in tension and compression reversals due to the near symmetric quasi-static response at low strains (Figure 62a). This behavior shows that slip is the dominant plastic deformation mode in HX [224]. Results show a fully elastic response for strain amplitudes less than 0.4% and a significant plastic deformation at higher strain amplitudes. The stress-strain results obtained from the hysteresis loops will be used in the next sections for energy-based fatigue modeling.
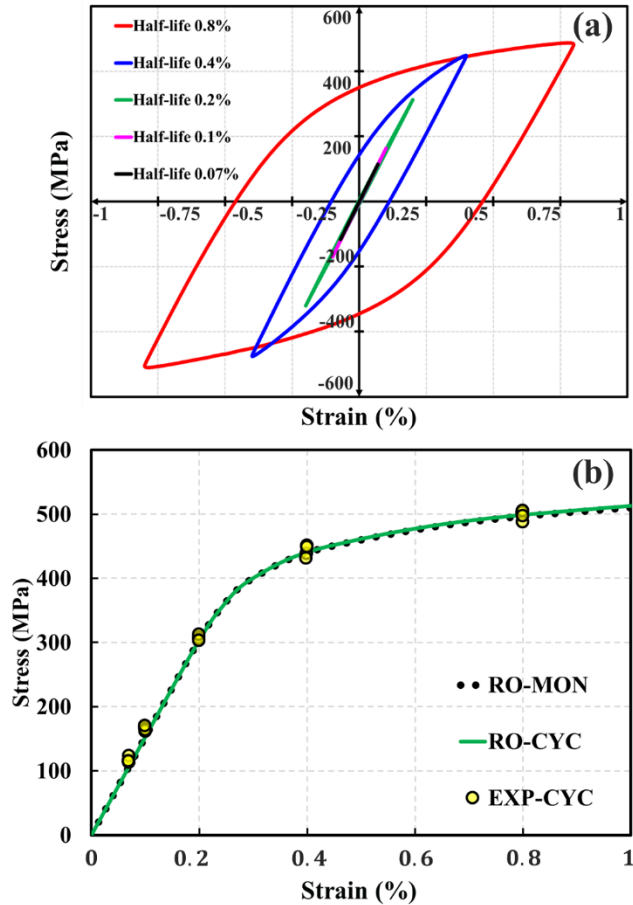
Figure 64: (a) Stabilized hysteresis at different strain amplitudes, (b) Cyclic and monotonic stress-strain curves.

The corresponding cyclic stress-strain (EXP-CYC) curve is shown in Figure 64(b). Results show a near similar behavior between the monotonic and cyclic stress-strain curves. Various stabilized behaviors of the AM specimens have been reported in the literature compared to monotonic results. Cyclic hardening was reported by Yadollahi et al. [15] in 17-4 precipitation hardening stainless steel due to martensitic transformation. On the other hand, cyclic softening has also been reported in 304L [207] and 316L [168] stainless steels. The CSS curve of LPBF-HX has not been reported previously. As observed in Figure 64b, the current study results do not show cyclic hardening or softening in half-life stress-strain response. It should be noted that the primary hardening in the first decades of cyclic loading (Figure 63) is neutralized by the followed softening during later cycles. This lack of cyclic hardening/softening has also been observed in AISI 18Ni300 maraging steel [209].

The cyclic (RO-CYC) and monotonic (RO-MON) stress-strain curves were modeled using the Ramberg-Osgood equation (Equation 2) and are also shown in Figure 64(b). It should be noted that RO-CYC was modeled using the half-life stabilized hysteresis loop. The Ramberg-Osgood equation can be written as [225]:

$$\varepsilon = \frac{\sigma}{E} + (\frac{\sigma}{K'})^{\frac{1}{n'}} \qquad\qquad \text{Equation 20}$$

where n' is the cyclic strain hardening exponent and K' is the cyclic strength coefficient. The values for K' and n' extracted in the present study for LPBF-HX are given in Table 9. Due to the similar material response under cyclic and monotonic loading (Figure 64b), the strength coefficient and hardening exponent show almost identical values under monotonic and cyclic loading.

Table 9: Monotonic and Cyclic Ramberg-Osgood (RO) Parameters.

	Strength coefficient (MPa)	Strain hardening exponent
Monotonic	783	0.085
Cyclic	795	0.087

6.4 Fatigue Behavior and Modeling

Since fatigue is the primary failure mechanism in the most engineering components and structures, accurate fatigue life prediction is crucial. Several models have been established for the fatigue life prediction based on the fatigue damage developed at each cycle [53]. Strain- and energy-based fatigue models are among the models widely used for fatigue life prediction and were used in the current research to calibrate and extract the model parameters from the experimental data. The calibrated models were tested over other strain-controlled and also several stress-controlled tests to evaluate the merits and applicability of these models in different loading conditions. Details about the different models are presented below.

Basquin-Coffin-Manson (BCM) equation is mostly used for modeling the strain-life response of metals[226]. The elastic strain and plastic strain amplitudes are related to the reversals to failure by the Basquin and Coffin-Manson equations, respectively and combined as [227]:

$$\varepsilon_a = \varepsilon_a^e + \varepsilon_a^p = \frac{\sigma_f'}{E}(2N_f)^b + \varepsilon_f'(2N_f)^c$$

where ε_a, ε_a^e and ε_a^p are the total, elastic and plastic strain amplitudes, respectively. E is the modulus of elasticity (153 GPa) [144], and N_f is the fatigue life. σ_f' and b are the fatigue strength coefficient and fatigue strength exponent, respectively, and ε_f' and c are fatigue ductility coefficient and fatigue ductility exponent, respectively. These fatigue properties were determined by applying least square regression to elastic and plastic strain amplitudes versus loading reversals according to the ASTM E739 standard [228] and are listed in Table 6. Figure 65a shows the elastic, plastic and BCM model lines and the experimental data points in $\varepsilon - N$ diagram. The experimental results show highly repeatable lives under cyclic loading at each strain amplitude.
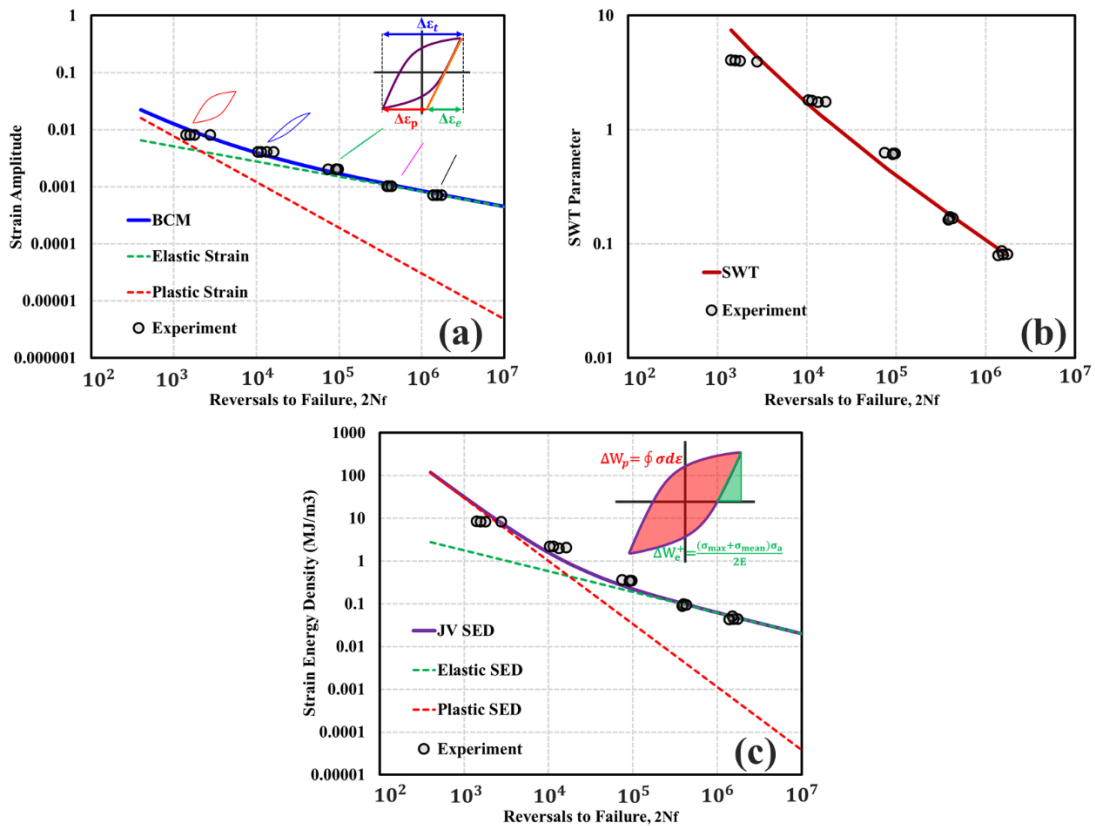
Figure 65: Fatigue modeling (a) Strain-Life and BCM (b) SWT parameter (c) Energy-Life and JV method.

The Smith-Watson-Topper (SWT) model [229] have been introduced to consider the mean stress effect on fatigue lives based on the assumption that the product between σ_{max} and ε_a is constant for a specific fatigue life in various combinations of mean stress and strain amplitude. The SWT parameter is related to fatigue life by four different constants, which are essentially the same as those for the BCM model:

$$\sigma_{max}\varepsilon_a = \frac{(\sigma_f')^2}{E}(2N_f)^{2b} + \sigma_f'\varepsilon_f'(2N_f)^{b+c} \qquad \text{Equation 22}$$

where σ_{max} is the maximum stress at the half-life cycle. Figure 65b represents the calculated SWT parameter for LPBF-HX as a function of reversals to failure.

The energy-based approach assumes that the dissipated energy density during cyclic loading has a major contribution to the fatigue damage process, especially within the LCF regime [53,209]. The Jahed-Varvani model (JV) [55,230] is another model utilized in the current investigation to predict the fatigue life of LPBF-HX. The JV model considers the strain energy density as the fatigue damage parameter, as opposed to the Basquin-Coffin-Manson model considering the life to strain amplitude. In the JV energy model, the total strain energy density is calculated by two terms: (i) the plastic strain energy density, W_p (ii) the positive elastic strain energy density, W_e^+ [74]. The elastic term accounted for the effect of mean stress and was calculated according to the revised formulation proposed in [231]. The plastic strain energy density is commonly calculated from the area inside the half-life fatigue hysteresis. Therefore, the total strain energy density is defined as [230,231]:

$$W = W_e^+ + W_p = \frac{(\sigma_{max} + \sigma_{mean})\sigma_a}{2E} + \oint \sigma d\varepsilon \qquad \text{Equation 23}$$

where σ_{max} is the maximum tensile stress, σ_{mean} is the mean stress and σ_a is the stress amplitude of the half-life hysteresis. The total strain energy density is related to the fatigue reversals by [230]:

$$W = E_e'(2N_f)^B + E_f'(2N_f)^C \qquad \text{Equation 24}$$

where E_e', B, E_f', and C are the energy-based fatigue strength coefficient, the fatigue strength exponent, the fatigue toughness coefficient, and the fatigue toughness exponent, respectively. The parameters of the JV model are calculated and listed in Table 6. The JV energy-life curve and the experimental points are shown in Figure 65c. Although plastic strain energy density has been used

previously [53] for fatigue life perditions, it was limited to the LCF region where considerable plasticity is present. The JV model produces a reasonable correlation with the fatigue lives both in the LCF and HCF region due to the consideration of elastic strain energy density in addition to the plastic strain energy density.

Table 10: BCM and JV model parameters for LPBF-HX.

BCM Parameters				JV Parameters			
σ_f' (MPa)	ε_f'	b	c	E_e' (MJ/m^3)	E_f' (MJ/m^3)	B	C
4877.36	1.93	-0.26	-0.8	50.72	773870.03	-0.49	-1.47

Figure 66 shows the correlation between the experimentally obtained fatigue life and the predicted fatigue life of LPBF-HX calculated through different modeling approaches. The experimental data from the strain-controlled fatigue tests at five strain amplitudes (0.07%, 0.1%, 0.2%, 0.4% and 0.8%) with four replicates at each strain amplitude were used for model calibration, which is shown by circles in Figure 66. The merit of the models was tested by two different sets of data. Firstly, experimental results from three additional strain amplitudes (0.09%, 0.3% and 0.6%) were validated with the selected models and are shown with triangles in Figure 66. Results show that all three models predict the fatigue lives of the calibration and validation dataset within the 2X life bands. Secondly, the stress-controlled experimental results (squares in Figure 66b and c) were also used to examine the capability of the JV and SWT model in predicting fatigue life in other loading scenarios with the presence of mean stress ($R_\sigma = 0.1$). Figure 66b and c demonstrate that both JV and SWT models offer good estimation of life. Fatigue life predictions of stress-controlled tests in the presence of mean stress show that the fatigue life predictions at high-stress levels, i.e., σ_{max} =550 and 625 MPa, are within the 2X life bands. However, at a lower stress level (σ_{max} =350 MPa) both models provide an underestimated conservative life prediction. As these models consider the elastic and plastic parts of strain or strain energy densities of fully reversed loading for calibration, utilization of these models should be taken with caution for other loading conditions, since the elastic and plastic parts of strain or strain energy densities combinations might not be the same. Moreover, in the HCF range of life the plastic strain/energy term vanishes, and the fatigue damage is estimated solely by the elastic strain/energy term. Therefore, the accuracy of the elastic term in explaining the fatigue damage becomes more important and a slight deviation in elastic term calculation may result in a significant deviation in the life prediction within the

HCF. However, these models are able to provide a preliminary life estimations and more diverse testing, including variable amplitude loading, pure cyclic shear and multi-axial testing is required for further examination of these models.
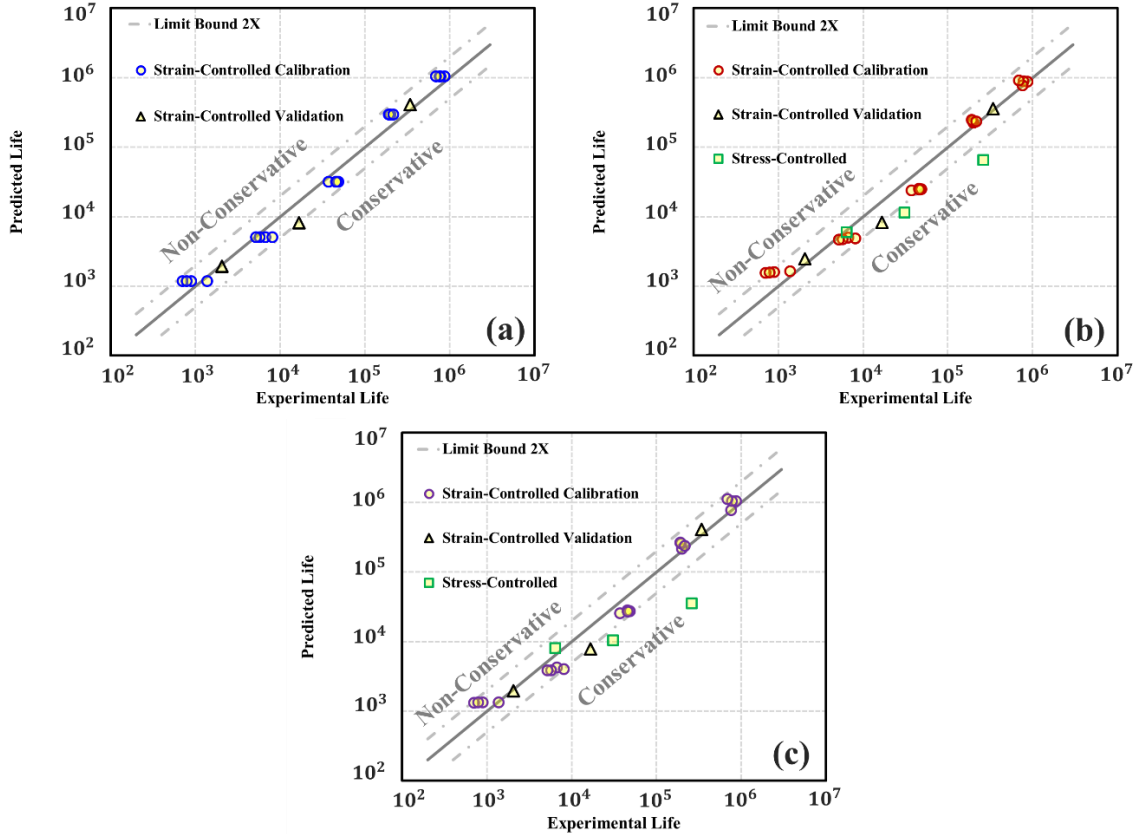
Figure 66: Predicted vs. experimental life based on different fatigue models (a) BCM, (b) SWT and (c) JV.

The prediction accuracy of the models used in the current study was quantified by the root mean square logarithmic error (RMSLE) parameter, which is defined as:

$$RMSLE = \sqrt{\frac{1}{k}\sum_{i=1}^{k}\left[log\left(\frac{N_{f,Predicted}}{N_{f,Experimental}}\right)_i\right]^2} \qquad \text{Equation 25}$$

where, $N_{f,Experimental}$, and $N_{f,Predicted}$ are the experimental and predicted lives, respectively and k is the number of experiments in each loading scenario. The calculated RMSLE values are

tabulated in Table 11, which are similar for different models in each loading condition. A preliminary conclusion from this study is that the SWT and JV models provide the same level of accuracy in the life prediction of LPBF-HX under uniaxial constant amplitude load cases. However, the prediction accuracy under variable amplitude loading and multiaxial loading conditions could be the subject of further studies.

Table 11: RMSLE Comparison of the models for different loading conditions.

Fatigue Model	Strain-controlled calibration tests	Strain-controlled validation tests	Stress-controlled validation tests
BCM	0.146	0.186	-
JV	0.178	0.193	0.580
SWT	0.181	0.182	0.515

Additively manufactured specimens are commonly associated with high scatter in the fatigue response [232,233]. This is usually due to the internal defects found in AM specimens. High scatter in experimental data affects the modeling approaches as the models cannot accurately predict the fatigue response. However, in this study, the fatigue results show minor scatter due to the optimized process parameters used to manufacture the specimens resulting in highly dense specimens. These results suggest that specimens manufactured with the optimized process parameters result in low scatter as observed with conventionally manufactured specimens. Moreover, the well-known conventional fatigue models can predict the fatigue lives without the need for any modification or utilizing defects-based models [234]. On the other hand, as long as the manufacturing conditions are not optimized various types of defects (gas porosities and lack of fusions) could be present in the specimen under investigation and it is possible for the fatigue crack to initiate from each of them. This can lead to high scatter in fatigue lives and cause misunderstanding in the interpretation of the fatigue test results. Therefore, to improve the fatigue model predictions the first attempt should be the process optimization to minimize the volume fraction of defects. If the experimental results still show a significant scatter, the next step will be adopting sophisticated fracture mechanics defect-based models.

6.5   Design Curve

The median strain-life curve, coming from the regression, is not sufficiently prudent to be readily used for the design purposes. Therefore a life curve that considers a high level of reliability and confidence is necessary. In order to guarantee that the majority of the fatigue data falls above the minimum or lower bound value the design strain-life curves are constructed. The choice of the lower bound fatigue life curve depends on industry standards and the required safety level [235]. There are different procedures for the construction of the design curve such as η-sigma Design Curve [236], ASME boiler and pressure code method [237] and ASTM method [228,238]. The η-sigma Design Curve is obtained by reducing η (usually 2 or 3) times the sample standard deviation from the median curve [236]. The ASME Boiler and Pressure code method obtains the design curve by applying safety factor of 2 on strain level and 20 on the life of the median curve [237], and the ASTM method is based on double-sided confidence interval approach [228,238]. However, all these approaches do not consider the statistical distribution of the results related to the number of samples and different reliability/confidence values. The approximate Owen tolerance limit, used in the current study, can address these shortcomings [235,236]. The R95C90 design curve ensures 95% possibility of survival (reliability) with 90% confidence level at a certain value. In this procedure, a variable Y_{RC} defined as the lower bound of $\bar{Y}$, is derived from the median regression curve, with confidence level C and reliability R at a desired strain $X_i = \log(\varepsilon_a)$ defined as:

$$Y_{RC}(X_i) = \bar{Y}(X_i) - K_{RC} \times s \hspace{3cm} \text{Equation 26}$$

where in our fatigue study the $Y_{RC} = \log(2N_{f,RC})$ which is the fatigue life associated with the strain amplitude ε_a after applying the Owen approach, $\bar{Y} = \log(2N_{f,BCM})$ and is obtained from the median BCM line (Equation 21), K_{RC} is the Owen tolerance limit and s is the sample standard deviation of $\bar{Y}$ on X_i. Substituting new expressions in Equation 26 and rearranging yields:

$$\log(2N_{f,RC}) = \log(2N_{f,BCM}) - K_{RC} \times s = \log\left(\frac{2N_{f,BCM}}{10^{K_{RC} \times s}}\right) \hspace{2cm} \text{Equation 27}$$

Equation 27 was applied separately to the elastic and plastic parts of the BCM equation to calculate the coefficients for the desired reliability and confidence level, i.e., $\sigma'_{f,RC}$ and $\varepsilon'_{f,RC}$. The Owen tolerance limit (K_{RC}) is available based on the sample size, reliability and confidence level and can be found from [238]. To account for the uncertainty in strain measurements, the threshold plastic

strain amplitude was selected as 0.0005 [235] and the corresponding K-factors for the elastic and plastic strain amplitude lines were selected as 2.292 and 2.987 [238], respectively for 95% reliability and 90% confidence level [235]. The slopes of the regression lines in the BCM model for the elastic and plastic lines (parameters b and c) are assumed to be constant, i.e., independent of the reliability and confidence level. The new R95C90 BCM design curve is expressed by:

$$\varepsilon_a = \varepsilon_a^e + \varepsilon_a^p = \frac{\sigma'_{f,R95C90}}{E}(2N_f)^b + \varepsilon'_{f,R95C90}(2N_f)^c \qquad \text{Equation 28}$$

Figure 67 (a) shows the experimental, median BCM curve (Equation 21) and R95C90 design curve normalized to the maximum strain amplitude (Figure 65a). It should be noted that the median BCM curve has a reliability of 50% or R50 while Equation 28 considers the desirable reliability and confidence level, considering that reliability = 1 - rate of failure. The same procedure can be followed to obtain the design curve corresponding to the JV model, plotted in Figure 68 (b) normalized to the maximum strain energy density (Figure 65c).
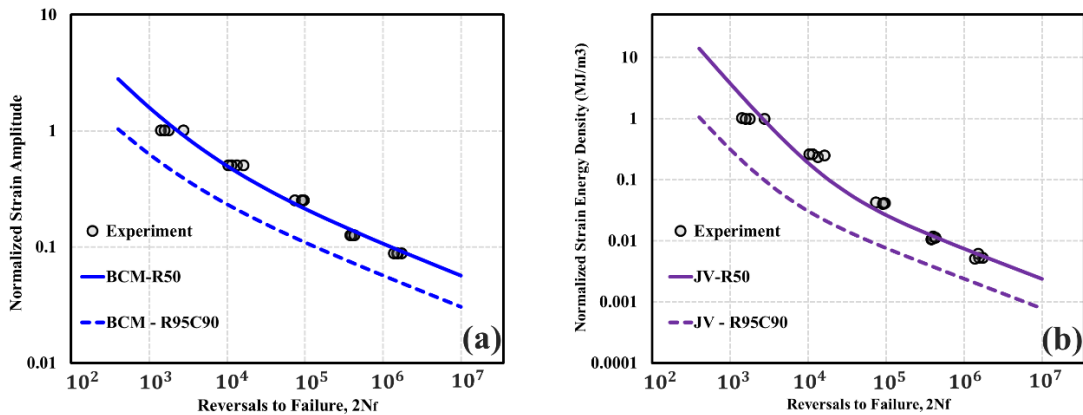
Figure 69: Normalized design curves with 95% reliability and 90% confidence for (a) BCM and (b) JV models.

The BCM and JV models parameters after applying the approximate Owen tolerance limit approach are listed in Table 12. Comparison of the R95C90 with the median values (Table 6) shows that applying the approximate Owen tolerance limit approach results in a reduction in the fatigue strength, ductility and toughness coefficients, which yields a statistically safer design.

Table 12: The R95C90 design curve parameters for the BCM and JV models.

BCM - R95C90			
$\sigma'_{f,R95C90}$ (MPa)	$\varepsilon'_{f,R95C90}$	b	c
2617.81	0.57	-0.26	-0.8
JV - R95C90			
$E'_{e,R95C90}$ (MJ/m^3)	$E'_{f,R95C90}$ (MJ/m^3)	B	C
16.65	53908.17	-0.49	-1.47

6.6 Conclusions

In the present study, the cyclic deformation and fatigue behavior of LPBF-HX was investigated at different strain amplitudes and various fatigue models were used to predict the fatigue lives. From the above results and discussion, the following conclusions are made:

1- Quasi-static tension and compression LPBF-HX depicts tension-compression symmetry in the initial yielding and small plastic strain region. As plastic strain increases to above ~2-3%, an asymmetric hardening behavior under tension and compression becomes apparent with strain rate being larger in compression.

2- LPBF-HX exhibits various cyclic hardening/softening behavior at different strain amplitudes. At high strain amplitudes, primary cyclic hardening is observed followed by a prolonged softening. However, at lower strain amplitudes only slight hardening is observed.

3- Half-life hysteresis loops from LPBF-HX show a symmetrical behavior in tension-compression reversals for all strain amplitudes. In addition, cyclic stress-strain curves do not show cyclic hardening or softening as the half-life hysteresis loops coincide with the monotonic stress-strain curve. The Ramberg-Osgood model was calibrated on the experimental half-life and monotonic results and show the same trend.

4- BCM, SWT and JV fatigue life models were calibrated, tested, and validated over the cyclic experimental data under different loading conditions and mean stresses, and the prediction results showed good agreement with the experimental data. In other words, within the limited scope of the present research, it can be concluded that the fatigue life of optimized

nearly full-dense LPBF-HX specimens can be predicted by well-known BCM and JV fatigue models without the need to use more sophisticated defect-based methods.

5- Design curves with 95% reliability and 90% confidence level have been constructed on the median BCM and JV curves using the approximate Owen tolerance limit. The new BCM and JV models parameters have been calculated and reported.

Chapter 7

7 Conclusions and Future Work

Effects of manufacturing conditions on the various aspects of samples and parts' microstructure and performance under quasi-static and cyclic loading have been pursued throughout this thesis. A comprehensive introduction that frames the context and motivation for this research work was discussed. More importantly, the research objectives were founded upon addressing the knowledge gap in the current state-of-the-art within the field and constructed to make this a novel and useful research undertaking. Secondly, an exhaustive literature review highlighting the key works surrounding the LPBF of metallic materials and superalloys was conducted and summarized. The following chapters combine the experimental investigations and phenomenological modeling to address the research objectives.

7.1 Thesis Overall Conclusions

The following conclusions can be drawn from this thesis:

1- Spatter particles ejection is an inevitable side phenomenon of melting the powder-bed by a highly localized heat source. In the case of Hastelloy X, the spatter generation process did not alter the chemical composition and crystallographic phases. However, a change in the microstructure of the powders was observed.

2- The distribution of spatter particles on the build plate is highly dependent on the machine architecture. In EOS M290, used in this research, a spatter-rich region forms at the gas outlet. Due to the size difference the spatter particles and the virgin powder the powder-bed characteristics change dynamically in the spatter-rich region. Therefore, samples' quality changes throughout the build plate with poorer quality in the spatter rich region.

3- Altering laser scanning speed (LSS) could affect parts' properties. Extremely low and high LSSs induce porosities/defects with different natures in part, while moderate laser scanning speed at medium power results in nearly full dense results. Spherical keyhole porosities may form at low LSS and lack of fusion (LoF) defects with irregular shape are induced in part due to improper melting overlaps. The presence of defects and porosities deteriorates the mechanical performance of the parts.

4- At moderate laser scanning speeds which result in nearly full dense parts, mechanical properties of the printed parts show higher strength at higher LSSs. Increasing LSS reduces grains size by decreasing the size of the melt pools and higher probability of partially melted particles. Yield strength increases by decreasing the grains size, obeying the Hall-Petch relationship.

5- Preventing similar heat flow pattern in successive layers by rotating laser scanning vectors at each layer hinders the formation of a dominant texture and helps to reduce in plane anisotropy. A random texture is observed more clearly at higher LSS because of more grain participation in pole figure formation due to smaller grains size.

6- Low- and high –cycle fatigue, LCF and HCF respectively, the performance of LPBF-HX parts depend on the manufacturing conditions and specifically LSS. In the LCF region, due to significant amount of plasticity, samples with smaller grains, i.e., higher LSS shows longer fatigue lives due to lower pre-strain damage and hysteresis stabilization at lower strains. On the other hand, at the HCF region stress concentration leading to crack initiation play significant role. Samples printed with lower LSS possess smoother surface finish and perform better when the applied stress is lower than the yield strength.

7- Cyclic deformation of LPBF-HX samples depends on the applied strain amplitudes under strain-controlled fatigue tests. At lower strain amplitudes where most of the applied strain is elastic and reversible, slight hardening observed at the beginning of cyclic loading. However, primary cyclic hardening followed by prolonged cyclic softening is happening when the portion of plastic strain is increasing at higher strain amplitudes.

8- In the nearly full dense optimized region of process parameters used in this thesis, fatigue life of LPBF-HX parts could be predicted with acceptable accuracy by well-known BCM and SWT strain-based fatigue models. Recently developed energy-based JV fatigue model is able to predict fatigue life at different fatigue loading conditions.

7.2 Recommendations and Future Work

The research work described in this thesis was intended to investigate the effect of additive manufacturing processing conditions on parts' features and properties at room temperature. To this end, specific areas in the build plate containing parts with inferior properties, spatter rich region, were identified and an optimized processing window for laser scanning speed to achieve nearly

full dense LPBF-HX parts were investigated. Moreover, parts' properties under cyclic loading and adequate fatigue life prediction methods were studied with the construction of relevant fatigue design curves. To achieve a wider understanding of parts' properties further research on the material's aspects and applications should be conducted.

1. In the current research all samples were printed with EOS M290 which is using a continuous laser. It is suggested to evaluate the effect of manufacturing machines, and using a pulsed or modulated laser beam have on the microstructure and related mechanical properties. This will help to compare the as-built microstructure of LPBF-HX manufacturing with different laser modes and investigate the advantages and disadvantages of each machine.

2. More examination of the microstructure is needed at higher magnifications using TEM to investigate the dislocation arrangement and measuring the dislocation density. It is suggested to study the interrupted fatigue samples at different stages of cyclic deformation to investigate the changes in dislocation configurations and density and correlate these changes to the observed cyclic hardening and softening.

3. A detailed study is needed to understand the textural evolution during plastic straining. Changes in the orientation and textural evolution while straining may shed light to the high fracture strain of LPBF-HX in the as-built condition.

4. The microstructural and related mechanical properties of LPBF-HX after heat treatment must be the subject of a detailed study. Since most of the parts made by AM will undergo various heat treatments before being put in service, due to high residual stress in the as-built condition. The microstructural investigation after different heat treatments across various length scales would help to understand the material's response in more details from sub-grain structures and dislocations density to grain morphology. Moreover, a design a specific heat treatment for the LPBF samples, due to difference in the starting microstructure before heat treatment, varies significantly form the conventionally made alloys.

5. In the current work monotonic and fatigue investigations were performed under uniaxial loading conditions while most of the complex engineering superalloys parts experience multi-axial loading conditions. Monotonic shear test is needed to evaluate the shear strength of the LPBF-HX and microstructural evolution during progression of shear

deformation and its comparison with the uniaxial studies would widen the knowledge about the deformation of single phase FCC alloys. Multi-axial fatigue study is crucial as the fatigue under multi-axial loading condition is the reason of most engineering failures. Moreover, more comprehensive fatigue models could be calibrated and used for real part application and the power of newly developed energy-based fatigue models can be evaluated in more depth and detail.

6. Although in the current thesis mechanical performance of LPBF-HX was investigated in detail at room temperature, superalloys are well-known for their superior performance at high temperatures. Obviously, the next phase after evaluation and selection of the best manufacturing condition for performance at room temperature, it is suggested to investigate the LPBF-HX properties at high temperatures. Hot tensile tests would show the drop the strength and/or ductility which shows the application temperature window. Hot fatigue tests are needed to calibrate fatigue model parameters for the real part application conditions and evaluate the expected life more realistically.

Letter of Copyright Permission

The necessary copyright permissions have been obtained to re-use published materials. This section provides the licenses and permissions for Chapters 3, 4 and 5 from the publishers (Elsevier). It is Elsevier's current policy that, "*as the author of the Elsevier article, you retain the right to include it in a thesis or dissertation, provided it is not published commercially. Permission is not required, but please ensure that you reference the journal as the original source.*" Proper referencing within this thesis has been done to give credit to the respective journal articles in chapters 3, 4 and 5. At the time of this writing chapter 6 has not been submitted for publication so no permissions are given. Below contains the obtained permissions for chapters 3, 4 and 5.

Permission for Chapter 3:

On the effect of spatter particles distribution on the quality of Hastelloy X parts made by laser powder-bed fusion additive manufacturing
Author: Reza Esmaeilizadeh,Usman Ali,Ali Keshavarzkermani,Yahya Mahmoodkhani,Ehsan Marzbanrad,Ehsan Toyserkani
Publication: Journal of Manufacturing Processes
Publisher: Elsevier
Date: January 2019

© 2018 Published by Elsevier Ltd on behalf of The Society of Manufacturing Engineers.

Journal Author Rights

BACK
CLOSE WINDOW

Permission for Chapter 4:

Customizing mechanical properties of additively manufactured Hastelloy X parts by adjusting laser scanning speed
Author: Reza Esmaeilizadeh,Ali Keshavarzkermani,Usman Ali,Yahya Mahmoodkhani,Behzad Behravesh,Hamid Jahed,Ali Bonakdar,Ehsan Toyserkani
Publication: Journal of Alloys and Compounds
Publisher: Elsevier
Date: 5 January 2020

© 2019 Elsevier B.V. All rights reserved.

Journal Author Rights

BACK
CLOSE WINDOW

Permission for Chapter 5:

On the effect of laser powder-bed fusion process parameters on quasi-static and fatigue behaviour of Hastelloy X: A microstructure/defect interaction study
Author: Reza Esmaeilizadeh,Ali Keshavarzkermani,Usman Ali,Behzad Behravesh,Ali Bonakdar,Hamid Jahed,Ehsan Toyserkani
Publication: Additive Manufacturing
Publisher: Elsevier
Date: February 2021

© 2020 Elsevier B.V. All rights reserved.

Journal Author Rights

BACK
CLOSE WINDOW

The necessary copyright permissions have been obtained to re-use published materials. This section provides the licenses and permissions for reproduction of figures found in various articles from various publishers found in the literature review chapter of this work (Chapter 2).

Permission for Figure 2:

Permission for Figure 3:

Permission for Figure 4:

Permission for Figure 5:

Permission for Figure 6a:

Permission for Figure 6b:

Permission for Figure 9:

Permission for Figure 10:

Permission for Figure 11a:

Order Completed

Thank you for your order.

This Agreement between Mr. Reza Esmaeilizadeh ("You") and Elsevier ("Elsevier") consists of your license details and the terms and conditions provided by Elsevier and Copyright Clearance Center.

Your confirmation email will contain your order number for future reference.

License Number	5045040705343
License date	Apr 09, 2021

🖨 Printable Details

Licensed Content

Licensed Content Publisher	Elsevier
Licensed Content Publication	Journal of Alloys and Compounds
Licensed Content Title	Direct metal laser melting of Inconel 718: Process impact on grain formation and orientation
Licensed Content Author	Ali Keshavarzkermani, Magda Sadowski, Leila Ladani
Licensed Content Date	Mar 5, 2018
Licensed Content Volume	736
Licensed Content Issue	n/a
Licensed Content Pages	9
Journal Type	S&T

Order Details

Type of Use	reuse in a thesis/dissertation
Portion	figures/tables/illustrations
Number of figures/tables/illustrations	1
Format	both print and electronic
Are you the author of this Elsevier article?	No
Will you be translating?	No

About Your Work

Title	Characterization and Modelling of Additively Manufactured Hastelloy X Parts under Quasi-Static and Cyclic Loading
Institution name	University of Waterloo
Expected presentation date	May 2021

Additional Data

Portions	Figure 3

Requestor Location

Requestor Location	Mr. Reza Esmaeilizadeh 505 Lincoln road unit 505 Waterloo, ON N2J 4N3 Canada Attn: Mr. Reza Esmaeilizadeh

Tax Details

Publisher Tax ID	GB 494 6272 12

Price

Total	0.00 CAD

Total: 0.00 CAD

CLOSE WINDOW   ORDER MORE

Permission for Figure 11b:

Order Number: 1110796
Order Date: 09 Apr 2021

Print order

Payment Information

Reza Esmaeilizadeh
reza.esmaeilizadeh@uwaterloo.ca
Payment method: Invoice

Billing Address:
Mr. Reza Esmaeilizadeh
130 Lincoln road
unit 505
Waterloo, ON N2J 4N3
Canada

+1 (519) 722-6993
reza.esmaeilizadeh@uwaterloo.ca

Customer Location:
Mr. Reza Esmaeilizadeh
130 Lincoln road
unit 505
Waterloo, ON N2J 4N3
Canada

Order Details

1. Annual review of materials research

Billing Status:
Open

Print License

Order license ID	1110796-1	Type of use	Republish in a thesis/dissert...
Order detail status	Completed	Publisher	ANNUAL REVIEWS
ISSN	1545-4118	Portion	Image/photo/illustration

0.00 CAD
Republication Permission

⊞ View Details

Total Items: 1

Subtotal: 0.00 CAD
Order Total: **0.00 CAD**

Back To Orders

Permission for Figure 12b:

Order Completed

Thank you for your order.
This Agreement between Mr. Reza Esmaeilizadeh ("You") and Elsevier ("Elsevier") consists of your license details and the terms and conditions provided by Elsevier and Copyright Clearance Center.

Your confirmation email will contain your order number for future reference.

License Number	5045050181459		Printable Details
License date	Apr 09, 2021		

Licensed Content
		Order Details	
Licensed Content Publisher	Elsevier	Type of Use	reuse in a thesis/dissertation
Licensed Content Publication	Materials Characterization	Portion	figures/tables/illustrations
Licensed Content Title	Selective laser melting of Co-29Cr-6Mo alloy with laser power 180–360W: Cellular growth, intercellular spacing and the related thermal condition	Number of figures/tables/illustrations	1
		Format	both print and electronic
Licensed Content Author	K. Darvish, Z.W. Chen, M.A.L. Phan, T. Pasang	Are you the author of this Elsevier article?	No
Licensed Content Date	Jan 1, 2018	Will you be translating?	No
Licensed Content Volume	135		
Licensed Content Issue	n/a		
Licensed Content Pages	9		
Journal Type	S&T		

About Your Work
		Additional Data	
Title	Characterization and Modelling of Additively Manufactured Hastelloy X Parts under Quasi-Static and Cyclic Loading	Portions	Figure 5
Institution name	University of Waterloo		
Expected presentation date	May 2021		

Requestor Location
		Tax Details	
Requestor Location	Mr. Reza Esmaeilizadeh 505 Lincoln road unit 505 Waterloo, ON N2J 4N3 Canada Attn: Mr. Reza Esmaeilizadeh	Publisher Tax ID	GB 494 6272 12

Price
Total	0.00 CAD

Total: 0.00 CAD

CLOSE WINDOW   ORDER MORE

Permission for Figure 13a:

Order Completed

Thank you for your order.
This Agreement between Mr. Reza Esmaeilizadeh ("You") and Elsevier ("Elsevier") consists of your license details and the terms and conditions provided by Elsevier and Copyright Clearance Center.

Your confirmation email will contain your order number for future reference.

License Number	5045050307066		Printable Details
License date	Apr 09, 2021		

Licensed Content
		Order Details	
Licensed Content Publisher	Elsevier	Type of Use	reuse in a thesis/dissertation
Licensed Content Publication	Acta Metallurgica et Materialia	Portion	figures/tables/illustrations
Licensed Content Title	The microstructure of rapidly solidified Al–Fe alloys subjected to laser surface treatment	Number of figures/tables/illustrations	1
		Format	both print and electronic
Licensed Content Author	M. Gremaud, M. Carrard, W. Kurz	Are you the author of this Elsevier article?	No
Licensed Content Date	Dec 1, 1990	Will you be translating?	No
Licensed Content Volume	38		
Licensed Content Issue	12		
Licensed Content Pages	13		
Journal Type	S&T		

About Your Work
		Additional Data	
Title	Characterization and Modelling of Additively Manufactured Hastelloy X Parts under Quasi-Static and Cyclic Loading	Portions	Figure 1
Institution name	University of Waterloo		
Expected presentation date	May 2021		

Requestor Location
		Tax Details	
Requestor Location	Mr. Reza Esmaeilizadeh 505 Lincoln road unit 505 Waterloo, ON N2J 4N3 Canada Attn: Mr. Reza Esmaeilizadeh	Publisher Tax ID	GB 494 6272 12

Price
Total	0.00 CAD

Total: 0.00 CAD

CLOSE WINDOW   ORDER MORE

Permission for Figure 14:

Order Completed

Thank you for your order.

This Agreement between Mr. Reza Esmaeilizadeh ("You") and Elsevier ("Elsevier") consists of your license details and the terms and conditions provided by Elsevier and Copyright Clearance Center.

Your confirmation email will contain your order number for future reference.

⊕ Printable Details

| License Number | 5045050525337 |
| License date | Apr 09, 2021 |

Licensed Content

Licensed Content Publisher	Elsevier
Licensed Content Publication	Materials Characterization
Licensed Content Title	Selective laser melting of Co-29Cr-6Mo alloy with laser power 180–360W: Cellular growth, intercellular spacing and the related thermal condition
Licensed Content Author	K. Darvish,Z.W. Chen,M.A.L. Phan,T. Pasang
Licensed Content Date	Jan 1, 2018
Licensed Content Volume	135
Licensed Content Issue	n/a
Licensed Content Pages	9
Journal Type	S&T

Order Details

Type of Use	reuse in a thesis/dissertation
Portion	figures/tables/illustrations
Number of figures/tables/illustrations	2
Format	both print and electronic
Are you the author of this Elsevier article?	No
Will you be translating?	No

About Your Work

Title	Characterization and Modelling of Additively Manufactured Hastelloy X Parts under Quasi Static and Cyclic Loading
Institution name	University of Waterloo
Expected presentation date	May 2021

Additional Data

| Portions | Figure 5 and Figure 6 |

Requestor Location

| Requestor Location | Mr. Reza Esmaeilizadeh
505 Lincoln road
unit 505
Waterloo, ON N2J 4N3
Canada
Attn: Mr. Reza Esmaeilizadeh |

Tax Details

| Publisher Tax ID | GB 494 6272 12 |

Price

| Total | 0.00 CAD |

CLOSE WINDOW   Total: 0.00 CAD
                                                                   ORDER MORE

Permission for Figure 15:

Order Completed

Thank you for your order.

This Agreement between Mr. Reza Esmaeilizadeh ("You") and Elsevier ("Elsevier") consists of your license details and the terms and conditions provided by Elsevier and Copyright Clearance Center.

Your confirmation email will contain your order number for future reference.

⊕ Printable Details

| License Number | 5045050671418 |
| License date | Apr 09, 2021 |

Licensed Content

Licensed Content Publisher	Elsevier
Licensed Content Publication	Materials Characterization
Licensed Content Title	Microstructure of selective laser melted CM247LC nickel-based superalloy and its evolution through heat treatment
Licensed Content Author	V.D. Divya,R. Muñoz-Moreno,O.M.D.M. Messé,J.S. Barnard,S. Baker,T. Ilkson,H.J. Stone
Licensed Content Date	Apr 1, 2016
Licensed Content Volume	114
Licensed Content Issue	n/a
Licensed Content Pages	13
Journal Type	S&T

Order Details

Type of Use	reuse in a thesis/dissertation
Portion	figures/tables/illustrations
Number of figures/tables/illustrations	2
Format	both print and electronic
Are you the author of this Elsevier article?	No
Will you be translating?	No

About Your Work

Title	Characterization and Modelling of Additively Manufactured Hastelloy X Parts under Quasi Static and Cyclic Loading
Institution name	University of Waterloo
Expected presentation date	May 2021

Additional Data

| Portions | Figure 5 and Figure 6 |

Requestor Location

| Requestor Location | Mr. Reza Esmaeilizadeh
505 Lincoln road
unit 505
Waterloo, ON N2J 4N3
Canada
Attn: Mr. Reza Esmaeilizadeh |

Tax Details

| Publisher Tax ID | GB 494 6272 12 |

Price

| Total | 0.00 CAD |

CLOSE WINDOW   Total: 0.00 CAD
                                                                   ORDER MORE

Permission for Figure 16:

Permission for Figure 17a and c:

Permission for Figure 17b:

Permission for Figure 18:

Permission for Figure 19:

License Number	5045091004837			Printable Details
License date	Apr 09, 2021			

Licensed Content

		Order Details	
Licensed Content Publisher	Elsevier	Type of Use	reuse in a thesis/dissertation
Licensed Content Publication	Acta Materialia	Portion	figures/tables/illustrations
Licensed Content Title	Microstructure and yield strength of SLM-fabricated CM247LC Ni-Superalloy	Number of figures/tables/illustrations	1
Licensed Content Author	Xiqian Wang,Luke N. Carter,Bo Pang,Moataz M. Attallah,Michael H. Loretto	Format	both print and electronic
Licensed Content Date	Apr 15, 2017	Are you the author of this Elsevier article?	No
Licensed Content Volume	128	Will you be translating?	No
Licensed Content Issue	n/a		
Licensed Content Pages	9		
Journal Type	S&T		

About Your Work

		Additional Data	
Title	Characterization and Modelling of Additively Manufactured Hastelloy X Parts under Quasi-Static and Cyclic Loading	Portions	Figure 7
Institution name	University of Waterloo		
Expected presentation date	May 2021		

Requestor Location

		Tax Details	
Requestor Location	Mr. Reza Esmaeilizadeh 505 Lincoln road unit 505 Waterloo, ON N2J 4N3 Canada Attn: Mr. Reza Esmaeilizadeh	Publisher Tax ID	GB 494 6272 12

Price

Total	0.00 CAD

Total: 0.00 CAD

CLOSE WINDOW   ORDER MORE

Permission for Figure 20:

License Number	5045091388832			Printable Details
License date	Apr 09, 2021			

Licensed Content

		Order Details	
Licensed Content Publisher	Elsevier	Type of Use	reuse in a thesis/dissertation
Licensed Content Publication	Materials Characterization	Portion	figures/tables/illustrations
Licensed Content Title	Microstructure of selective laser melted CM247LC nickel-based superalloy and its evolution through heat treatment	Number of figures/tables/illustrations	1
Licensed Content Author	V.D. Divya,R. Muñoz-Moreno,O.M.D.M. Messé,J.S. Barnard,S. Baker,T. Illston,H.J. Stone	Format	both print and electronic
Licensed Content Date	Apr 1, 2016	Are you the author of this Elsevier article?	No
Licensed Content Volume	114	Will you be translating?	No
Licensed Content Issue	n/a		
Licensed Content Pages	13		
Journal Type	S&T		

About Your Work

		Additional Data	
Title	Characterization and Modelling of Additively Manufactured Hastelloy X Parts under Quasi-Static and Cyclic Loading	Portions	Figure 9
Institution name	University of Waterloo		
Expected presentation date	May 2021		

Requestor Location

		Tax Details	
Requestor Location	Mr. Reza Esmaeilizadeh 505 Lincoln road unit 505 Waterloo, ON N2J 4N3 Canada Attn: Mr. Reza Esmaeilizadeh	Publisher Tax ID	GB 494 6272 12

Price

Total	0.00 CAD

Total: 0.00 CAD

CLOSE WINDOW   ORDER MORE

Permission for Figure 21:

Order Completed

Thank you for your order.
This Agreement between Mr. Reza Esmaeilizadeh ("You") and Elsevier ("Elsevier") consists of your license details and the terms and conditions provided by Elsevier and Copyright Clearance Center.

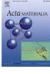Your confirmation email will contain your order number for future reference.

License Number   5045091487599
License date   Apr 09, 2021

Printable Details

Licensed Content
Licensed Content Publisher   Elsevier
Licensed Content Publication   Acta Materialia
Licensed Content Title   Microstructure and yield strength of SLM-fabricated CM247LC Ni-Superalloy
Licensed Content Author   Xiqian Wang,Luke N. Carter,Bo Pang,Moataz M. Attallah,Michael H. Loretto
Licensed Content Date   Apr 15, 2017
Licensed Content Volume   128
Licensed Content Issue   n/a
Licensed Content Pages   9
Journal Type   S&T

Order Details
Type of Use   reuse in a thesis/dissertation
Portion   figures/tables/illustrations
Number of figures/tables/Illustrations 1
Format   both print and electronic
Are you the author of this Elsevier article?   No
Will you be translating?   No

About Your Work
Title   Characterization and Modelling of Additively Manufactured Hastelloy X Parts under Quasi-Static and Cyclic Loading
Institution name   University of Waterloo
Expected presentation date   May 2021

Additional Data
Portions   Figure 12

Requestor Location
Requestor Location   Mr. Reza Esmaeilizadeh
                        505 Lincoln road
                        unit 505
                        Waterloo, ON N2J 4N3
                        Canada
                        Attn: Mr. Reza Esmaeilizadeh

Tax Details
Publisher Tax ID   GB 494 6272 12

Price
Total   0.00 CAD

Total: 0.00 CAD

CLOSE WINDOW   ORDER MORE

Permission for Figure 22:

Order Completed

Thank you for your order.
This Agreement between Mr. Reza Esmaeilizadeh ("You") and Elsevier ("Elsevier") consists of your license details and the terms and conditions provided by Elsevier and Copyright Clearance Center.

Your confirmation email will contain your order number for future reference.

License Number   5045100133338
License date   Apr 09, 2021

Printable Details

Licensed Content
Licensed Content Publisher   Elsevier
Licensed Content Publication   Materials Science and Engineering: A
Licensed Content Title   Influence of post heat treatments on anisotropy of mechanical behaviour and microstructure of Hastelloy-X parts produced by selective laser melting
Licensed Content Author   Dacian Tomus,Yang Tian,Paul A. Rometsch,Martin Heilmaier,Xinhua Wu
Licensed Content Date   Jun 14, 2016
Licensed Content Volume   667
Licensed Content Issue   n/a
Licensed Content Pages   12
Journal Type   S&T

Order Details
Type of Use   reuse in a thesis/dissertation
Portion   figures/tables/illustrations
Number of figures/tables/Illustrations 2
Format   both print and electronic
Are you the author of this Elsevier article?   No
Will you be translating?   No

About Your Work
Title   Characterization and Modelling of Additively Manufactured Hastelloy X Parts under Quasi-Static and Cyclic Loading
Institution name   University of Waterloo
Expected presentation date   May 2021

Additional Data
Portions   Figure 2 and Figure 13

Requestor Location
Requestor Location   Mr. Reza Esmaeilizadeh
                        505 Lincoln road
                        unit 505
                        Waterloo, ON N2J 4N3
                        Canada
                        Attn: Mr. Reza Esmaeilizadeh

Tax Details
Publisher Tax ID   GB 494 6272 12

Price
Total   0.00 CAD

Total: 0.00 CAD

CLOSE WINDOW   ORDER MORE

Permission for Figure 23:

Critical assessment of the fatigue performance of additively manufactured Ti–6Al–4V and perspective for future research
Author: P. Li,D.H. Warner,A. Fatemi,N. Phan
Publication: International Journal of Fatigue
Publisher: Elsevier
Date: April 2016

Order Completed

Thank you for your order.

This Agreement between Mr. Reza Esmaeilizadeh ("You") and Elsevier ("Elsevier") consists of your license details and the terms and conditions provided by Elsevier and Copyright Clearance Center.

Your confirmation email will contain your order number for future reference.

License Number	5045100280506
License date	Apr 09, 2021

Licensed Content

Licensed Content Publisher	Elsevier
Licensed Content Publication	International Journal of Fatigue
Licensed Content Title	Critical assessment of the fatigue performance of additively manufactured Ti–6Al–4V and perspective for future research
Licensed Content Author	P. Li,D.H. Warner,A. Fatemi,N. Phan
Licensed Content Date	Apr 1, 2016
Licensed Content Volume	85
Licensed Content Issue	n/a
Licensed Content Pages	14
Journal Type	S&T

Order Details

Type of Use	reuse in a thesis/dissertation
Portion	figures/tables/illustrations
Number of figures/tables/illustrations	2
Format	both print and electronic
Are you the author of this Elsevier article?	No
Will you be translating?	No

About Your Work

Title	Characterization and Modelling of Additively Manufactured Hastelloy X Parts under Quasi-Static and Cyclic Loading
Institution name	University of Waterloo
Expected presentation date	May 2021

Additional Data

Portions	Figure 1 and Figure 3

Requestor Location

Requestor Location	Mr. Reza Esmaeilizadeh 505 Lincoln road unit 505 Waterloo, ON N2J 4N3 Canada Attn: Mr. Reza Esmaeilizadeh

Tax Details

Publisher Tax ID	GB 494 6272 12

Price

Total	0.00 CAD

Total: 0.00 CAD

CLOSE WINDOW   ORDER MORE

Permission for Figure 24:

Fatigue Life of Titanium Alloys Fabricated by Additive Layer Manufacturing Techniques for Dental Implants
Author: Kwai S. Chan et al
Publication: Metallurgical and Materials Transactions A
Publisher: Springer Nature
Date: Oct 17, 2012

Order Completed

Thank you for your order.

This Agreement between Mr. Reza Esmaeilizadeh ("You") and Springer Nature ("Springer Nature") consists of your license details and the terms and conditions provided by Springer Nature and Copyright Clearance Center.

Your confirmation email will contain your order number for future reference.

License Number	5045100464224
License date	Apr 09, 2021

Licensed Content

Licensed Content Publisher	Springer Nature
Licensed Content Publication	Metallurgical and Materials Transactions A
Licensed Content Title	Fatigue Life of Titanium Alloys Fabricated by Additive Layer Manufacturing Techniques for Dental Implants
Licensed Content Author	Kwai S. Chan et al
Licensed Content Date	Oct 17, 2012

Order Details

Type of Use	Thesis/Dissertation
Requestor type	academic/university or research institute
Format	print and electronic
Portion	figures/tables/illustrations
Number of figures/tables/illustrations	3
Will you be translating?	no
Circulation/distribution	1 - 29
Author of this Springer Nature content	no

About Your Work

Title	Characterization and Modelling of Additively Manufactured Hastelloy X Parts under Quasi-Static and Cyclic Loading
Institution name	University of Waterloo
Expected presentation date	May 2021

Additional Data

Portions	Figure 4 and Figure 6 and Figure 12

Requestor Location

Requestor Location	Mr. Reza Esmaeilizadeh 505 Lincoln road unit 505 Waterloo, ON N2J 4N3 Canada Attn: Mr. Reza Esmaeilizadeh

Tax Details

Price

Total	0.00 CAD

Total: 0.00 CAD

CLOSE WINDOW   ORDER MORE

Permission for Figure 25:

Improvement of fatigue resistance and ductility of TiAl6V4 processed by selective laser melting
Author: Galina Kasperovich, Joachim Hausmann
Publication: Journal of Materials Processing Technology
Publisher: Elsevier
Date: June 2015

Order Completed

Thank you for your order.

This Agreement between Mr. Reza Esmaeilizadeh ("You") and Elsevier ("Elsevier") consists of your license details and the terms and conditions provided by Elsevier and Copyright Clearance Center.

Your confirmation email will contain your order number for future reference.

Printable Details

License Number	5045100574680		
License date	Apr 09, 2021		

Licensed Content | | **Order Details** |
|---|---|---|---|
| Licensed Content Publisher | Elsevier | Type of Use | reuse in a thesis/dissertation |
| Licensed Content Publication | Journal of Materials Processing Technology | Portion | figures/tables/illustrations |
| Licensed Content Title | Improvement of fatigue resistance and ductility of TiAl6V4 processed by selective laser melting | Number of figures/tables/illustrations | 2 |
| Licensed Content Author | Galina Kasperovich, Joachim Hausmann | Format | both print and electronic |
| Licensed Content Date | Jun 1, 2015 | Are you the author of this Elsevier article? | No |
| Licensed Content Volume | 220 | Will you be translating? | No |
| Licensed Content Issue | n/a | | |
| Licensed Content Pages | 13 | | |
| Journal Type | S&T | | |

About Your Work | | **Additional Data** |
|---|---|---|---|
| Title | Characterization and Modelling of Additively Manufactured Hastelloy X Parts under Quasi-Static and Cyclic Loading | Portions | Figure 3 and Figure 16 |
| Institution name | University of Waterloo | | |
| Expected presentation date | May 2021 | | |

Requestor Location | | **Tax Details** |
|---|---|---|---|
| Requestor Location | Mr. Reza Esmaeilizadeh 505 Lincoln road unit 505 Waterloo, ON N2J 4N3 Canada Attn: Mr. Reza Esmaeilizadeh | Publisher Tax ID | GB 494 6272 12 |

Price

Total	0.00 CAD

Total: 0.00 CAD

CLOSE WINDOW   ORDER MORE

Permission for Figure 26:

Improving the surface quality and mechanical properties by shot-peening of 17-4 stainless steel fabricated by additive manufacturing
Author: Bandar AlMangour, Jenn-Ming Yang
Publication: Materials & Design
Publisher: Elsevier
Date: 15 November 2016

Order Completed

Thank you for your order.

This Agreement between Mr. Reza Esmaeilizadeh ("You") and Elsevier ("Elsevier") consists of your license details and the terms and conditions provided by Elsevier and Copyright Clearance Center.

Your confirmation email will contain your order number for future reference.

Printable Details

License Number	5045100749385
License date	Apr 09, 2021

Licensed Content | | **Order Details** |
|---|---|---|---|
| Licensed Content Publisher | Elsevier | Type of Use | reuse in a thesis/dissertation |
| Licensed Content Publication | Materials & Design | Portion | figures/tables/illustrations |
| Licensed Content Title | Improving the surface quality and mechanical properties by shot-peening of 17-4 stainless steel fabricated by additive manufacturing | Number of figures/tables/illustrations | 2 |
| Licensed Content Author | Bandar AlMangour, Jenn-Ming Yang | Format | both print and electronic |
| Licensed Content Date | Nov 15, 2016 | Are you the author of this Elsevier article? | No |
| Licensed Content Volume | 110 | Will you be translating? | No |
| Licensed Content Issue | n/a | | |
| Licensed Content Pages | 11 | | |
| Journal Type | S&T | | |

About Your Work | | **Additional Data** |
|---|---|---|---|
| Title | Characterization and Modelling of Additively Manufactured Hastelloy X Parts under Quasi-Static and Cyclic Loading | Portions | Figure 2 and Figure 6 |
| Institution name | University of Waterloo | | |
| Expected presentation date | May 2021 | | |

Requestor Location | | **Tax Details** |
|---|---|---|---|
| Requestor Location | Mr. Reza Esmaeilizadeh 505 Lincoln road unit 505 Waterloo, ON N2J 4N3 Canada Attn: Mr. Reza Esmaeilizadeh | Publisher Tax ID | GB 494 6272 12 |

Price

Total	0.00 CAD

Total: 0.00 CAD

CLOSE WINDOW   ORDER MORE

Permission for Figure 27a:

Order Completed

Thank you for your order.
This Agreement between Mr. Reza Esmaeilizadeh ("You") and Elsevier ("Elsevier") consists of your license details and the terms and conditions provided by Elsevier and Copyright Clearance Center.

Your confirmation email will contain your order number for future reference.

License Number	5045100878146		Printable Details
License date	Apr 09, 2021		

Licensed Content

		Order Details	
Licensed Content Publisher	Elsevier	Type of Use	reuse in a thesis/dissertation
Licensed Content Publication	Materials Science and Engineering: A	Portion	figures/tables/illustrations
Licensed Content Title	Laser powder bed fusion of Hastelloy X: Effects of hot isostatic pressing and the hot cracking mechanism	Number of figures/tables/illustrations	1
Licensed Content Author	Quanquan Han,Raya Mertens,Maria L. Montero-Sistiaga,Shoufeng Yang,Rossitza Setchi,Kim Vanmeensel,Brecht Van Hooreweder,Sam L. Evans,Haiyang Fan	Format	both print and electronic
Licensed Content Date	Aug 8, 2018	Are you the author of this Elsevier article?	No
Licensed Content Volume	732	Will you be translating?	No
Licensed Content Issue	n/a		
Licensed Content Pages	12		
Journal Type	S&T		

About Your Work

		Additional Data	
Title	Characterization and Modelling of Additively Manufactured Hastelloy X Parts under Quasi-Static and Cyclic Loading	Portions	Figure 9
Institution name	University of Waterloo		
Expected presentation date	May 2021		

Requestor Location

		Tax Details	
Requestor Location	Mr. Reza Esmaeilizadeh	Publisher Tax ID	GB 494 6272 12
	505 Lincoln road		
	unit 505		
	Waterloo, ON N2J 4N3		
	Canada		
	Attn: Mr. Reza Esmaeilizadeh		

Price

Total	0.00 CAD

Total: 0.00 CAD

CLOSE WINDOW   ORDER MORE

Permission for Figure 27b and c:

Order Completed

Thank you for your order.
This Agreement between Mr. Reza Esmaeilizadeh ("You") and Springer Nature ("Springer Nature") consists of your license details and the terms and conditions provided by Springer Nature and Copyright Clearance Center.

Your confirmation email will contain your order number for future reference.

License Number	5045101018349		Printable Details
License date	Apr 09, 2021		

Licensed Content

		Order Details	
Licensed Content Publisher	Springer Nature	Type of Use	Thesis/Dissertation
Licensed Content Publication	Journal of Materials Research	Requestor type	academic/university or research institute
Licensed Content Title	On the fatigue properties of metals manufactured by selective laser melting — The role of ductility	Format	print and electronic
Licensed Content Author	Stefan Leuders et al	Portion	figures/tables/illustrations
Licensed Content Date	Sep 1, 2014	Number of figures/tables/illustrations	2
		Will you be translating?	no
		Circulation/distribution	1 - 29
		Author of this Springer Nature content	no

About Your Work

		Additional Data	
Title	Characterization and Modelling of Additively Manufactured Hastelloy X Parts under Quasi-Static and Cyclic Loading	Portions	Figure 6 and Figure 7
Institution name	University of Waterloo		
Expected presentation date	May 2021		

Requestor Location

		Tax Details	
Requestor Location	Mr. Reza Esmaeilizadeh		
	505 Lincoln road		
	unit 505		
	Waterloo, ON N2J 4N3		
	Canada		
	Attn: Mr. Reza Esmaeilizadeh		

Price

Total	0.00 CAD

Total: 0.00 CAD

CLOSE WINDOW   ORDER MORE

Permission for Figure 28a:

Permission for Figure 28b:

Permission for Figure 30:

Order Completed

Thank you for your order.

This Agreement between Mr. Reza Esmaeilizadeh ("You") and Elsevier ("Elsevier") consists of your license details and the terms and conditions provided by Elsevier and Copyright Clearance Center.

Your confirmation email will contain your order number for future reference.

License Number	5045101363871
License date	Apr 09, 2021

📄 **Licensed Content**

Licensed Content Publisher	Elsevier
Licensed Content Publication	Additive Manufacturing
Licensed Content Title	On the effect of shot-peening on fatigue resistance of AlSi10Mg specimens fabricated by additive manufacturing using selective laser melting (AM-SLM)
Licensed Content Author	Naor Elad Uuan,Shlomo Ramati,Roni Shneck,Nachum Frage,Ori Yeheskel
Licensed Content Date	May 1, 2018
Licensed Content Volume	21
Licensed Content Issue	n/a
Licensed Content Pages	7
Journal Type	S&T

📋 **Order Details**

Type of Use	reuse in a thesis/dissertation
Portion	figures/tables/illustrations
Number of figures/tables/illustrations	1
Format	both print and electronic
Are you the author of this Elsevier article?	No
Will you be translating?	No

📄 **About Your Work**

Title	Characterization and Modelling of Additively Manufactured Hastelloy X Parts under Quasi-Static and Cyclic Loading
Institution name	University of Waterloo
Expected presentation date	May 2021

🗂 **Additional Data**

Portions	Figure 12

📍 **Requestor Location**

Requestor Location	Mr. Reza Esmaeilizadeh 505 Lincoln road unit 505 Waterloo, ON N2J 4N3 Canada Attn: Mr. Reza Esmaeilizadeh

💲 **Tax Details**

Publisher Tax ID	GB 494 6272 12

💲 **Price**

Total	0.00 CAD

Total: 0.00 CAD

CLOSE WINDOW   ORDER MORE

Permission for Figure 31:

Order Completed

Thank you for your order.

This Agreement between Mr. Reza Esmaeilizadeh ("You") and Elsevier ("Elsevier") consists of your license details and the terms and conditions provided by Elsevier and Copyright Clearance Center.

Your confirmation email will contain your order number for future reference.

License Number	5045110010276
License date	Apr 09, 2021

📄 **Licensed Content**

Licensed Content Publisher	Elsevier
Licensed Content Publication	International Journal of Fatigue
Licensed Content Title	Effects of building orientation and heat treatment on fatigue behavior of selective laser melted 17-4 PH stainless steel
Licensed Content Author	Aref Yadollahi,Nima Shamsaei,Scott M. Thompson,Alaa Elwany,Linkan Bian
Licensed Content Date	Jan 1, 2017
Licensed Content Volume	94
Licensed Content Issue	n/a
Licensed Content Pages	18
Journal Type	S&T

📋 **Order Details**

Type of Use	reuse in a thesis/dissertation
Portion	figures/tables/illustrations
Number of figures/tables/illustrations	1
Format	both print and electronic
Are you the author of this Elsevier article?	No
Will you be translating?	No

📄 **About Your Work**

Title	Characterization and Modelling of Additively Manufactured Hastelloy X Parts under Quasi-Static and Cyclic Loading
Institution name	University of Waterloo
Expected presentation date	May 2021

🗂 **Additional Data**

Portions	Figure 12

📍 **Requestor Location**

Requestor Location	Mr. Reza Esmaeilizadeh 505 Lincoln road unit 505 Waterloo, ON N2J 4N3 Canada Attn: Mr. Reza Esmaeilizadeh

💲 **Tax Details**

Publisher Tax ID	GB 494 6272 12

💲 **Price**

Total	0.00 CAD

Total: 0.00 CAD

CLOSE WINDOW   ORDER MORE

Permission for Figure 32:

Criticality of porosity defects on the fatigue performance of wire + arc additive manufactured titanium alloy
Author: Romali Biswal,Xiang Zhang,Abdul Khadar Syed,Mustafa Awd,Jialuo Ding,Frank Walther,Stewart Williams
Publication: International Journal of Fatigue
Publisher: Elsevier
Date: May 2019

Order Completed

Thank you for your order.

This Agreement between Mr. Reza Esmaeilizadeh ("You") and Elsevier ("Elsevier") consists of your license details and the terms and conditions provided by Elsevier and Copyright Clearance Center.

Your confirmation email will contain your order number for future reference.

License Number   5045110115550   🖨 Printable Details

License date   Apr 09, 2021

📄 Licensed Content

Licensed Content Publisher	Elsevier
Licensed Content Publication	International Journal of Fatigue
Licensed Content Title	Criticality of porosity defects on the fatigue performance of wire + arc additive manufactured titanium alloy
Licensed Content Author	Romali Biswal,Xiang Zhang,Abdul Khadar Syed,Mustafa Awd,Jialuo Ding,Frank Walther,Stewart Williams
Licensed Content Date	May 1, 2019
Licensed Content Volume	122
Licensed Content Issue	n/a
Licensed Content Pages	10
Journal Type	S&T

📋 Order Details

Type of Use	reuse in a thesis/dissertation
Portion	figures/tables/illustrations
Number of figures/tables/illustrations	2
Format	both print and electronic
Are you the author of this Elsevier article?	No
Will you be translating?	No

📄 About Your Work

Title	Characterization and Modelling of Additively Manufactured Hastelloy X Parts under Quasi-Static and Cyclic Loading
Institution name	University of Waterloo
Expected presentation date	May 2021

📁 Additional Data

Portions	Figure 8 and Figure 12

📍 Requestor Location

Requestor Location	Mr. Reza Esmaeilizadeh 505 Lincoln road unit 505 Waterloo, ON N2J 4N3 Canada Attn: Mr. Reza Esmaeilizadeh

🧾 Tax Details

Publisher Tax ID	GB 494 6272 12

$ Price

Total	0.00 CAD

Total: 0.00 CAD

CLOSE WINDOW   ORDER MORE

References

[1]   W. Gao, Y. Zhang, D. Ramanujan, K. Ramani, Y. Chen, C.B. Williams, C.C.L. Wang, Y.C. Shin, S. Zhang, P.D. Zavattieri, The status, challenges, and future of additive manufacturing in engineering, Comput. Des. 69 (2015) 65–89. doi:10.1016/j.cad.2015.04.001.

[2]   C.Y. Lin, T. Wirtz, F. LaMarca, S.J. Hollister, Structural and mechanical evaluations of a topology optimized titanium interbody fusion cage fabricated by selective laser melting process, J. Biomed. Mater. Res. - Part A. 83 (2007) 272–279. doi:10.1002/jbm.a.31231.

[3]   D.D. Gu, W. Meiners, K. Wissenbach, R. Poprawe, Laser additive manufacturing of metallic components: materials, processes and mechanisms, Int. Mater. Rev. 57 (2012) 133–164. doi:10.1179/1743280411Y.0000000014.

[4]   T. Niendorf, S. Leuders, A. Riemer, F. Brenne, T. Tröster, H.A. Richard, D. Schwarze, Functionally graded alloys obtained by additive manufacturing, Adv. Eng. Mater. 16 (2014) 857–861. doi:10.1002/adem.201300579.

[5]   L.D. Bobbio, R.A. Otis, J.P. Borgonia, R.P. Dillon, A.A. Shapiro, Z.K. Liu, A.M. Beese, Additive manufacturing of a functionally graded material from Ti-6Al-4V to Invar: Experimental characterization and thermodynamic calculations, Acta Mater. 127 (2017) 133–142. doi:10.1016/j.actamat.2016.12.070.

[6]   H. Fayazfar, M. Salarian, A. Rogalsky, D. Sarker, P. Russo, V. Paserin, E. Toyserkani, A critical review of powder-based additive manufacturing of ferrous alloys: Process parameters, microstructure and mechanical properties, Mater. Des. (2018). doi:10.1016/j.matdes.2018.02.018.

[7]   B. AlMangour, D. Grzesiak, J. Cheng, Y. Ertas, Thermal behavior of the molten pool, microstructural evolution, and tribological performance during selective laser melting of TiC/316L stainless steel nanocomposites: Experimental and simulation methods, J. Mater. Process. Technol. 257 (2018) 288–301. doi:10.1016/j.jmatprotec.2018.01.028.

[8]   S.L. Sing, L.P. Lam, D.Q. Zhang, Z.H. Liu, C.K. Chua, Interfacial characterization of SLM parts in multi-material processing: Intermetallic phase formation between AlSi10Mg and C18400 copper alloy, Mater. Charact. 107 (2015) 220–227. doi:10.1016/j.matchar.2015.07.007.

[9]   V. Petrovic, J. Vicente Haro Gonzalez, O. Jordá Ferrando, J. Delgado Gordillo, J. Ramon Blasco Puchades, L. Portoles Grinan, Additive layered manufacturing: Sectors of industrial application shown through case studies, Int. J. Prod. Res. 49 (2011) 1061–1079.

doi:10.1080/00207540903479786.

[10] B. AlMangour, D. Grzesiak, T. Borkar, J.M. Yang, Densification behavior, microstructural evolution, and mechanical properties of TiC/316L stainless steel nanocomposites fabricated by selective laser melting, Mater. Des. 138 (2018) 119–128. doi:10.1016/j.matdes.2017.10.039.

[11] Z.H. Liu, D.Q. Zhang, S.L. Sing, C.K. Chua, L.E. Loh, Interfacial characterization of SLM parts in multi-material processing: Metallurgical diffusion between 316L stainless steel and C18400 copper alloy, Mater. Charact. 94 (2014) 116–125.

[12] F. Wang, Mechanical property study on rapid additive layer manufacture Hastelloy?? X alloy by selective laser melting technology, Int. J. Adv. Manuf. Technol. 58 (2012) 545–551. doi:10.1007/s00170-011-3423-2.

[13] B. Song, S. Dong, S. Deng, H. Liao, C. Coddet, Microstructure and tensile properties of iron parts fabricated by selective laser melting, Opt. Laser Technol. (2014). doi:10.1016/j.optlastec.2013.09.017.

[14] P. Li, D.H. Warner, A. Fatemi, N. Phan, Critical assessment of the fatigue performance of additively manufactured Ti-6Al-4V and perspective for future research, Int. J. Fatigue. 85 (2016) 130–143. doi:10.1016/j.ijfatigue.2015.12.003.

[15] A. Yadollahi, N. Shamsaei, S.M. Thompson, A. Elwany, L. Bian, Effects of building orientation and heat treatment on fatigue behavior of selective laser melted 17-4 PH stainless steel, Int. J. Fatigue. 94 (2017) 218–235. doi:10.1016/j.ijfatigue.2016.03.014.

[16] A. Fatemi, R. Molaei, S. Sharifimehr, N. Shamsaei, N. Phan, Torsional fatigue behavior of wrought and additive manufactured Ti-6Al-4V by powder bed fusion including surface finish effect, Int. J. Fatigue. 99 (2017) 187–201. doi:10.1016/j.ijfatigue.2017.03.002.

[17] D. Tomus, Y. Tian, P.A. Rometsch, M. Heilmaier, X. Wu, Influence of post heat treatments on anisotropy of mechanical behaviour and microstructure of Hastelloy-X parts produced by selective laser melting, Mater. Sci. Eng. A. 667 (2016) 42–53. doi:10.1016/j.msea.2016.04.086.

[18] T. DebRoy, H.L. Wei, J.S. Zuback, T. Mukherjee, J.W. Elmer, J.O. Milewski, A.M. Beese, A. Wilson-Heid, A. De, W. Zhang, Additive manufacturing of metallic components – Process, structure and properties, Prog. Mater. Sci. 92 (2018) 112–224. doi:10.1016/j.pmatsci.2017.10.001.

[19] A. Bandyopadhyay, B. Heer, Additive manufacturing of multi-material structures, Mater. Sci. Eng. R Reports. 129 (2018) 1–16. doi:10.1016/j.mser.2018.04.001.

[20]   S. Bremen, W. Meiners, A. Diatlov, Selective Laser Melting, Laser Tech. J. 9 (2012) 33–38. doi:10.1002/latj.201290018.

[21]   R.C. Reed, The Superalloys fundamentals and applications, 2006. doi:10.1017/CBO9780511541285.

[22]   V.D. Divya, R. Muñoz-Moreno, O.M.D.M. Messé, J.S. Barnard, S. Baker, T. Illston, H.J. Stone, Microstructure of selective laser melted CM247LC nickel-based superalloy and its evolution through heat treatment, Mater. Charact. 114 (2016) 62–74. doi:10.1016/j.matchar.2016.02.004.

[23]   Y. Tian, J.A. Muñiz-Lerma, M. Brochu, Nickel-based superalloy microstructure obtained by pulsed laser powder bed fusion, Mater. Charact. 131 (2017) 306–315. doi:10.1016/j.matchar.2017.07.024.

[24]   B. Geddes, H. Leon, X. Huang, Superalloys: alloying and performance, Asm International, 2010.

[25]   M.J. Donachie, Superalloys: A Technical Guide, 2nd Edition, America (NY). (2002) 1–409. doi:10.1361.

[26]   D.R. Askeland, P.P. Fulay, W.J. Wright, The science and engineering of materials 6th edition, Thomson Learn. Inc. (2010) 232–250.

[27]   M.A. Meyers, K.K. Chawla, Mechanical behavior of materials, Cambridge university press, 2008.

[28]   T.H. Courtney, Mechanical behavior of materials, Waveland Press, 2005.

[29]   A.H. Lefebvre, Gas turbine combustion, CRC press, 1998.

[30]   P.C. Collins, D.A. Brice, P. Samimi, I. Ghamarian, H.L. Fraser, Microstructural Control of Additively Manufactured Metallic Materials, Annu. Rev. Mater. Res. 46 (2016) 63–91. doi:10.1146/annurev-matsci-070115-031816.

[31]   A. Basak, S. Das, Epitaxy and Microstructure Evolution in Metal Additive Manufacturing, Annu. Rev. Mater. Res. 46 (2016) 125–149. doi:10.1146/annurev-matsci-070115-031728.

[32]   A. Keshavarzkermani, M. Sadowski, L. Ladani, Direct metal laser melting of Inconel 718: Process impact on grain formation and orientation, J. Alloys Compd. 736 (2018) 297–305. doi:10.1016/j.jallcom.2017.11.130.

[33]   S. Kou, Welding metallurgy, John Wiley & Sons, 2003.

[34]   K. Darvish, Z.W. Chen, M.A.L. Phan, T. Pasang, Selective laser melting of Co-29Cr-6Mo alloy

with laser power 180–360 W: Cellular growth, intercellular spacing and the related thermal condition, Mater. Charact. 135 (2018) 183–191. doi:10.1016/j.matchar.2017.11.042.

[35] M. Gremaud, M. Carrard, W. Kurz, The microstructure of rapidly solidified AlFe alloys subjected to laser surface treatment, Acta Metall. Mater. 38 (1990) 2587–2599. doi:10.1016/0956-7151(90)90271-H.

[36] N.J. Harrison, I. Todd, K. Mumtaz, Reduction of micro-cracking in nickel superalloys processed by Selective Laser Melting: A fundamental alloy design approach, Acta Mater. 94 (2015) 59–68. doi:10.1016/j.actamat.2015.04.035.

[37] W. Kurz, R. Trivedi, Rapid solidification processing and microstructure formation, Mater. Sci. Eng. A. 179–180 (1994) 46–51. doi:10.1016/0921-5093(94)90162-7.

[38] E. Robert, R. Hill, R. Abbaschian, Physical metallurgy principles, 697Y706. (1992).

[39] H. Fredriksson, U. Åkerlind, Solidification and Crystallization Processing in Metals and Alloys, 2012. doi:10.1002/9781119975540.

[40] D. Deng, R.L. Peng, H. Brodin, J. Moverare, Microstructure and mechanical properties of Inconel 718 produced by selective laser melting: Sample orientation dependence and effects of post heat treatments, Mater. Sci. Eng. A. 713 (2018) 294–306. doi:10.1016/j.msea.2017.12.043.

[41] X. Wang, L.N. Carter, B. Pang, M.M. Attallah, M.H. Loretto, Microstructure and yield strength of SLM-fabricated CM247LC Ni-Superalloy, Acta Mater. 128 (2017) 87–95. doi:10.1016/j.actamat.2017.02.007.

[42] D.A. Porter, K.. Easterling, Phase Transformation in Metals and Alloys, Chapman Hall. (2014) 1–5. doi:10.1007/s13398-014-0173-7.2.

[43] E. George, Dieter: Mechanical Metallurgy, (1988).

[44] K. Alrbaey, D. Wimpenny, R. Tosi, W. Manning, A. Moroz, On optimization of surface roughness of selective laser melted stainless steel parts: A statistical study, J. Mater. Eng. Perform. 23 (2014) 2139–2148. doi:10.1007/s11665-014-0993-9.

[45] K.S. Chan, M. Koike, R.L. Mason, T. Okabe, Fatigue life of titanium alloys fabricated by additive layer manufacturing techniques for dental implants, Metall. Mater. Trans. A Phys. Metall. Mater. Sci. 44 (2013) 1010–1022. doi:10.1007/s11661-012-1470-4.

[46] G. Kasperovich, J. Hausmann, Improvement of fatigue resistance and ductility of TiAl6V4

processed by selective laser melting, J. Mater. Process. Technol. 220 (2015) 202–214. doi:10.1016/j.jmatprotec.2015.01.025.

[47]   B. AlMangour, J.M. Yang, Improving the surface quality and mechanical properties by shot-peening of 17-4 stainless steel fabricated by additive manufacturing, Mater. Des. 110 (2016) 914–924. doi:10.1016/j.matdes.2016.08.037.

[48]   Q. Han, R. Mertens, M.L. Montero-Sistiaga, S. Yang, R. Setchi, K. Vanmeensel, B. Van Hooreweder, S.L. Evans, H. Fan, Laser powder bed fusion of Hastelloy X: Effects of hot isostatic pressing and the hot cracking mechanism, Mater. Sci. Eng. A. (2018). doi:10.1016/j.msea.2018.07.008.

[49]   S. Leuders, T. Lieneke, S. Lammers, T. Tröster, T. Niendorf, On the fatigue properties of metals manufactured by selective laser melting - The role of ductility, J. Mater. Res. 29 (2014) 1911–1919. doi:10.1557/jmr.2014.157.

[50]   S. Leuders, M. Thöne, A. Riemer, T. Niendorf, T. Tröster, H.A. Richard, H.J. Maier, On the mechanical behaviour of titanium alloy TiAl6V4 manufactured by selective laser melting: Fatigue resistance and crack growth performance, Int. J. Fatigue. 48 (2013) 300–307. doi:10.1016/j.ijfatigue.2012.11.011.

[51]   A. Riemer, S. Leuders, M. Thöne, H.A. Richard, T. Tröster, T. Niendorf, On the fatigue crack growth behavior in 316L stainless steel manufactured by selective laser melting, Eng. Fract. Mech. 120 (2014) 15–25. doi:10.1016/j.engfracmech.2014.03.008.

[52]   R.I. Stephens, A. Fatemi, R.R. Stephens, H.O. Fuchs, Metal fatigue in engineering, John Wiley & Sons, 2000.

[53]   F. Ellyin, Fatigue damage, crack growth and life prediction, Springer Science & Business Media, 2012.

[54]   H. Jahed, A. Varvani-Farahani, M. Noban, I. Khalaji, An energy-based fatigue life assessment model for various metallic materials under proportional and non-proportional loading conditions, Int. J. Fatigue. 29 (2007) 647–655. doi:10.1016/j.ijfatigue.2006.07.017.

[55]   H. Jahed, A. Varvani-farahani, Upper and lower fatigue life limits model using energy-based fatigue properties, 28 (2006) 467–473. doi:10.1016/j.ijfatigue.2005.07.039.

[56]   N.E. Uzan, S. Ramati, R. Shneck, N. Frage, O. Yeheskel, On the effect of shot-peening on fatigue resistance of AlSi10Mg specimens fabricated by additive manufacturing using selective laser

melting (AM-SLM), Addit. Manuf. 21 (2018) 458–464. doi:10.1016/j.addma.2018.03.030.

[57] R. Biswal, X. Zhang, A. Khadar Syed, M. Awd, J. Ding, F. Walther, S. Williams, Criticality of porosity defects on the fatigue performance of wire + arc additive manufactured titanium alloy, Int. J. Fatigue. (2019). doi:10.1016/j.ijfatigue.2019.01.017.

[58] S.L. Sing, L.P. Lam, D.Q. Zhang, Z.H. Liu, C.K. Chua, Interfacial characterization of SLM parts in multi-material processing: Intermetallic phase formation between AlSi10Mg and C18400 copper alloy, Mater. Charact. (2015). doi:10.1016/j.matchar.2015.07.007.

[59] B. Ferrar, L. Mullen, E. Jones, R. Stamp, C.J. Sutcliffe, Gas flow effects on selective laser melting (SLM) manufacturing performance, J. Mater. Process. Technol. 212 (2012) 355–364. doi:10.1016/j.jmatprotec.2011.09.020.

[60] Y. Mahmoodkhani, U. Ali, S. Imani Shahabad, A. Rani Kasinathan, R. Esmaeilizadeh, A. Keshavarzkermani, E. Marzbanrad, E. Toyserkani, On the measurement of effective powder layer thickness in laser powder-bed fusion additive manufacturing of metals, Prog. Addit. Manuf. Online, Available Https//Doi.Org/10.1007/S40964-018-0064-0. 0 (2018) 0. doi:10.1007/s40964-018-0064-0.

[61] U. Ali, Y. Mahmoodkhani, S. Imani Shahabad, R. Esmaeilizadeh, F. Liravi, E. Sheydaeian, K.Y. Huang, E. Marzbanrad, M. Vlasea, E. Toyserkani, On the measurement of relative powder-bed compaction density in powder-bed additive manufacturing processes, Mater. Des. 155 (2018). doi:10.1016/j.matdes.2018.06.030.

[62] H. Gong, K. Rafi, N. V. Karthik, T. Starr, B. Stucker, Defect morphology in Ti-6Al-4V parts fabricated by Selective Laser Melting and Electron Beam Melting, 24th Int. SFF Symp. - An Addit. Manuf. Conf. SFF 2013. (2013) 440–453. doi:10.1007/s11665-013-0658-0.

[63] S.L. Sing, F.E. Wiria, W.Y. Yeong, Selective laser melting of lattice structures: A statistical approach to manufacturability and mechanical behavior, Robot. Comput. Integr. Manuf. (2018). doi:10.1016/j.rcim.2017.06.006.

[64] K. Mumtaz, N. Hopkinson, Top surface and side roughness of Inconel 625 parts processed using selective laser melting, Rapid Prototyp. J. 15 (2009) 96–103. doi:10.1108/13552540910943397.

[65] E. Abele, M. Kniepkamp, Analysis and optimisation of vertical surface roughness in micro selective laser melting, Surf. Topogr. Metrol. Prop. 3 (2015). doi:10.1088/2051-672X/3/3/034007.

[66] D. Wang, Y. Liu, Y. Yang, D. Xiao, Theoretical and experimental study on surface roughness of

316L stainless steel metal parts obtained through selective laser melting, Rapid Prototyp. J. 22 (2016) 706–716. doi:10.1108/RPJ-06-2015-0078.

[67]   G. Strano, L. Hao, R.M. Everson, K.E. Evans, Surface roughness analysis, modelling and prediction in selective laser melting, J. Mater. Process. Technol. 213 (2013) 589–597. doi:10.1016/j.jmatprotec.2012.11.011.

[68]   S.A. Fatemi, J.Z. Ashany, A.J. Aghchai, A. Abolghasemi, Experimental investigation of process parameters on layer thickness and density in direct metal laser sintering: a response surface methodology approach, Virtual Phys. Prototyp. (2017). doi:10.1080/17452759.2017.1293274.

[69]   M. Jamshidinia, R. Kovacevic, The influence of heat accumulation on the surface roughness in powder-bed additive manufacturing, Surf. Topogr. Metrol. Prop. 3 (2015). doi:10.1088/2051-672X/3/1/014003.

[70]   S. Ly, A.M. Rubenchik, S.A. Khairallah, G. Guss, M.J. Matthews, Metal vapor micro-jet controls material redistribution in laser powder bed fusion additive manufacturing, Sci. Rep. 7 (2017). doi:10.1038/s41598-017-04237-z.

[71]   M.J. Matthews, G. Guss, S.A. Khairallah, A.M. Rubenchik, P.J. Depond, W.E. King, Denudation of metal powder layers in laser powder bed fusion processes, Acta Mater. 114 (2016) 33–42. doi:10.1016/j.actamat.2016.05.017.

[72]   S.A. Khairallah, A.T. Anderson, A. Rubenchik, W.E. King, Laser powder-bed fusion additive manufacturing: Physics of complex melt flow and formation mechanisms of pores, spatter, and denudation zones, Acta Mater. 108 (2016) 36–45. doi:10.1016/j.actamat.2016.02.014.

[73]   F. Calignano, Investigation of the accuracy and roughness in the laser powder bed fusion process, Virtual Phys. Prototyp. 13 (2018) 97–104. doi:10.1080/17452759.2018.1426368.

[74]   C. Qiu, C. Panwisawas, M. Ward, H.C. Basoalto, J.W. Brooks, M.M. Attallah, On the role of melt flow into the surface structure and porosity development during selective laser melting, Acta Mater. 96 (2015) 72–79. doi:10.1016/j.actamat.2015.06.004.

[75]   A.T. Sutton, C.S. Kriewall, M.C. Leu, J.W. Newkirk, Powder characterisation techniques and effects of powder characteristics on part properties in powder-bed fusion processes, Virtual Phys. Prototyp. 12 (2017) 3–29. doi:10.1080/17452759.2016.1250605.

[76]   M. Simonelli, C. Tuck, N.T. Aboulkhair, I. Maskery, I. Ashcroft, R.D. Wildman, R. Hague, A Study on the Laser Spatter and the Oxidation Reactions During Selective Laser Melting of 316L

Stainless Steel, Al-Si10-Mg, and Ti-6Al-4V, Metall. Mater. Trans. A Phys. Metall. Mater. Sci. 46 (2015) 3842–3851. doi:10.1007/s11661-015-2882-8.

[77] M. Taheri Andani, R. Dehghani, M.R. Karamooz-Ravari, R. Mirzaeifar, J. Ni, A study on the effect of energy input on spatter particles creation during selective laser melting process, Addit. Manuf. 20 (2018). doi:10.1016/j.addma.2017.12.009.

[78] A. Bin Anwar, Q.C. Pham, Study of the spatter distribution on the powder bed during selective laser melting, Addit. Manuf. (2018). doi:10.1016/j.addma.2018.04.036.

[79] A. Bin Anwar, Q.C. Pham, Selective laser melting of AlSi10Mg: Effects of scan direction, part placement and inert gas flow velocity on tensile strength, J. Mater. Process. Technol. (2017). doi:10.1016/j.jmatprotec.2016.10.015.

[80] L.C. Ardila, F. Garciandia, J.B. González-Díaz, P. Álvarez, A. Echeverria, M.M. Petite, R. Deffley, J. Ochoa, Effect of IN718 recycled powder reuse on properties of parts manufactured by means of Selective Laser Melting, in: Phys. Procedia, 2014: pp. 99–107. doi:10.1016/j.phpro.2014.08.152.

[81] A. Strondl, O. Lyckfeldt, H. Brodin, U. Ackelid, Characterization and Control of Powder Properties for Additive Manufacturing, JOM. 67 (2015) 549–554. doi:10.1007/s11837-015-1304-0.

[82] Y. Liu, Y. Yang, S. Mai, D. Wang, C. Song, Investigation into spatter behavior during selective laser melting of AISI 316L stainless steel powder, Mater. Des. 87 (2015) 797–806. doi:10.1016/j.matdes.2015.08.086.

[83] H. Asgari, C. Baxter, K. Hosseinkhani, M. Mohammadi, On microstructure and mechanical properties of additively manufactured AlSi10Mg_200C using recycled powder, Mater. Sci. Eng. A. 707 (2017) 148–158. doi:10.1016/j.msea.2017.09.041.

[84] G.F. Vander Voort, G.M. Lucas, E.P. Manilova, Metallography and Microstructures of Heat-Resistant Alloys, ASM Handb. Metallogr. Microstruct. 9 (2004) 820–859. doi:10.1361/asmhba0003737.

[85] N.T. Aboulkhair, N.M. Everitt, I. Ashcroft, C. Tuck, Reducing porosity in AlSi10Mg parts processed by selective laser melting, Addit. Manuf. 1 (2014) 77–86. doi:10.1016/j.addma.2014.08.001.

[86] S. Sivasankaran, K. Sivaprasad, R. Narayanasamy, V.K. Iyer, An investigation on flowability and

compressibility of AA 6061100-x-x wt.% TiO2 micro and nanocomposite powder prepared by blending and mechanical alloying, Powder Technol. 201 (2010) 70–82. doi:10.1016/j.powtec.2010.03.013.

[87]   P.W. Cleary, M.L. Sawley, DEM modelling of industrial granular flows: 3D case studies and the effect of particle shape on hopper discharge, Appl. Math. Model. 26 (2002) 89–111. doi:10.1016/S0307-904X(01)00050-6.

[88]   I. Yadroitsev, P. Bertrand, I. Smurov, Parametric analysis of the selective laser melting process, Appl. Surf. Sci. 253 (2007) 8064–8069. doi:10.1016/j.apsusc.2007.02.088.

[89]   F. Duflos, J.F. Stohr, Comparison of the quench rates attained in gas-atomized powders and melt-spun ribbons of Co- and Ni-base superalloys: influence on resulting microstructures, J. Mater. Sci. 17 (1982) 3641–3652. doi:10.1007/BF00752209.

[90]   W.Z. Abuzaid, M.D. Sangid, J.D. Carroll, H. Sehitoglu, J. Lambros, Slip transfer and plastic strain accumulation across grain boundaries in Hastelloy X, J. Mech. Phys. Solids. 60 (2012) 1201–1220. doi:10.1016/j.jmps.2012.02.001.

[91]   S. Li, Q. Wei, Y. Shi, Z. Zhu, D. Zhang, Microstructure Characteristics of Inconel 625 Superalloy Manufactured by Selective Laser Melting, J. Mater. Sci. Technol. 31 (2015) 946–952. doi:10.1016/j.jmst.2014.09.020.

[92]   E. Brandl, U. Heckenberger, V. Holzinger, D. Buchbinder, Additive manufactured AlSi10Mg samples using Selective Laser Melting (SLM): Microstructure, high cycle fatigue, and fracture behavior, Mater. Des. 34 (2012) 159–169.

[93]   R. Konečná, L. Kunz, G. Nicoletto, A. Bača, Long fatigue crack growth in Inconel 718 produced by selective laser melting, Int. J. Fatigue. 92 (2016) 499–506. doi:10.1016/j.ijfatigue.2016.03.012.

[94]   W. Muhammad, U. Ali, A.P. Brahme, J. Kang, R.K. Mishra, K. Inal, Experimental analyses and numerical modeling of texture evolution and the development of surface roughness during bending of an extruded aluminum alloy using a multiscale modeling framework, Int. J. Plast. (2017). doi:10.1016/j.ijplas.2017.09.013.

[95]   A.B. Spierings, N. Herres, G. Levy, Influence of the particle size distribution on surface quality and mechanical properties in AM steel parts, Rapid Prototyp. J. 17 (2011) 195–202. doi:10.1108/13552541111124770.

[96]   A. Simchi, H. Pohl, Effects of laser sintering processing parameters on the microstructure and

densification of iron powder, Mater. Sci. Eng. A. 359 (2003) 119–128. doi:10.1016/S0921-5093(03)00341-1.

[97]   A.B. Spierings, G. Levy, Comparison of density of stainless steel 316L parts produced with selective laser melting using different powder grades, Solid Free. Fabr. Proc. (2009) 342–353.

[98]   M. Ma, Z. Wang, M. Gao, X. Zeng, Layer thickness dependence of performance in high-power selective laser melting of 1Cr18Ni9Ti stainless steel, J. Mater. Process. Technol. 215 (2015) 142–150. doi:10.1016/j.jmatprotec.2014.07.034.

[99]   H. Meier, C. Haberland, Experimental studies on selective laser melting of metallic parts, Materwiss. Werksttech. 39 (2008) 665–670. doi:10.1002/mawe.200800327.

[100]   C. Qiu, N.J.E. Adkins, M.M. Attallah, Microstructure and tensile properties of selectively laser-melted and of HIPed laser-melted Ti-6Al-4V, Mater. Sci. Eng. A. 578 (2013) 230–239. doi:10.1016/j.msea.2013.04.099.

[101]   S.K. Everton, M. Hirsch, P.I. Stavroulakis, R.K. Leach, A.T. Clare, Review of in-situ process monitoring and in-situ metrology for metal additive manufacturing, Mater. Des. (2016). doi:10.1016/j.matdes.2016.01.099.

[102]   R. Casati, J. Lemke, M. Vedani, Microstructure and Fracture Behavior of 316L Austenitic Stainless Steel Produced by Selective Laser Melting, J. Mater. Sci. Technol. (2016). doi:10.1016/j.jmst.2016.06.016.

[103]   L. Thijs, K. Kempen, J.P. Kruth, J. Van Humbeeck, Fine-structured aluminium products with controllable texture by selective laser melting of pre-alloyed AlSi10Mg powder, Acta Mater. (2013). doi:10.1016/j.actamat.2012.11.052.

[104]   H.K. Rafi, N. V Karthik, H. Gong, T.L. Starr, B.E. Stucker, Microstructures and mechanical properties of Ti6Al4V parts fabricated by selective laser melting and electron beam melting, J. Mater. Eng. Perform. 22 (2013) 3872–3883.

[105]   E. Liverani, S. Toschi, L. Ceschini, A. Fortunato, Effect of selective laser melting (SLM) process parameters on microstructure and mechanical properties of 316L austenitic stainless steel, J. Mater. Process. Technol. (2017). doi:10.1016/j.jmatprotec.2017.05.042.

[106]   N. Read, W. Wang, K. Essa, M.M. Attallah, Selective laser melting of AlSi10Mg alloy: Process optimisation and mechanical properties development, Mater. Des. (2015). doi:10.1016/j.matdes.2014.09.044.

[107] D.C. Montgomery, Design and analysis of experiments, John wiley & sons, 2017.

[108] H.E. McCoy, J.P. Strizak, J.F. King, Hastelloy-X for High Temperature Gas-Cooled Reactor Applications, Nucl. Technol. 66 (1984) 161–174.

[109] J.H. Culling, Heat and corrosion resistant iron-nickel-chromium alloy, (1994).

[110] B. Swaminathan, W. Abuzaid, H. Sehitoglu, J. Lambros, Investigation using digital image correlation of Portevin-Le Chatelier Effect in Hastelloy X under thermo-mechanical loading, Int. J. Plast. (2014). doi:10.1016/j.ijplas.2014.09.001.

[111] M.A. Sofuoğlu, F.H. Çakır, S. Gürgen, S. Orak, M.C. Kuşhan, Experimental investigation of machining characteristics and chatter stability for Hastelloy-X with ultrasonic and hot turning, Int. J. Adv. Manuf. Technol. (2018). doi:10.1007/s00170-017-1153-9.

[112] J.C. Lippold, S.D. Kiser, J.N. DuPont, Welding metallurgy and weldability of nickel-base alloys, John Wiley & Sons, 2011.

[113] A. Keshavarzkermani, R. Esmaeilizadeh, U. Ali, P.D. Enrique, Y. Mahmoodkhani, N.Y. Zhou, A. Bonakdar, E. Toyserkani, Materials Science & Engineering A Controlling mechanical properties of additively manufactured hastelloy X by altering solidi fi cation pattern during laser powder-bed fusion, Mater. Sci. Eng. A. 762 (2019) 138081. doi:10.1016/j.msea.2019.138081.

[114] ASTM (American Society for Testing and Materials), E8/E8M standard test methods for tension testing of metallic materials, 2010. doi:10.1520/E0008.

[115] R. Esmaeilizadeh, U. Ali, A. Keshavarzkermani, Y. Mahmoodkhani, E. Marzbanrad, E. Toyserkani, On the effect of spatter particles distribution on the quality of Hastelloy X parts made by laser powder-bed fusion additive manufacturing, J. Manuf. Process. 37 (2019) 11–20. doi:https://doi.org/10.1016/j.jmapro.2018.11.012.

[116] U. Ali, R. Esmaeilizadeh, F. Ahmed, D. Sarker, W. Muhammad, A. Keshavarzkermani, Y. Mahmoodkhani, E. Marzbanrad, E. Toyserkani, Identification and characterization of spatter particles and their effect on surface roughness, density and mechanical response of 17-4 PH stainless steel laser powder-bed fusion parts, Mater. Sci. Eng. A. 756 (2019). doi:10.1016/j.msea.2019.04.026.

[117] T. Qi, H. Zhu, H. Zhang, J. Yin, L. Ke, X. Zeng, Selective laser melting of Al7050 powder: Melting mode transition and comparison of the characteristics between the keyhole and conduction mode, Mater. Des. (2017). doi:10.1016/j.matdes.2017.09.014.

[118] W.E. King, H.D. Barth, V.M. Castillo, G.F. Gallegos, J.W. Gibbs, D.E. Hahn, C. Kamath, A.M. Rubenchik, Observation of keyhole-mode laser melting in laser powder-bed fusion additive manufacturing, J. Mater. Process. Technol. (2014). doi:10.1016/j.jmatprotec.2014.06.005.

[119] R. Cunningham, S.P. Narra, C. Montgomery, J. Beuth, A.D. Rollett, Synchrotron-Based X-ray Microtomography Characterization of the Effect of Processing Variables on Porosity Formation in Laser Power-Bed Additive Manufacturing of Ti-6Al-4V, JOM. (2017). doi:10.1007/s11837-016-2234-1.

[120] K. Darvish, Z.W. Chen, T. Pasang, Reducing lack of fusion during selective laser melting of CoCrMo alloy: Effect of laser power on geometrical features of tracks, Mater. Des. (2016). doi:10.1016/j.matdes.2016.09.086.

[121] R.W. Hertzberg, Deformation and Fracture Mechanics of Engineering Materials, 1996. doi:10.1016/0261-3069(84)90070-0.

[122] J. Llorca, A. Needleman, S. Suresh, An analysis of the effects of matrix void growth on deformation and ductility in metal-ceramic composites, Acta Metall. Mater. (1991). doi:10.1016/0956-7151(91)90014-R.

[123] J.P. Bandstra, D.A. Koss, On the influence of void clusters on void growth and coalescence during ductile fracture, Acta Mater. (2008). doi:10.1016/j.actamat.2008.05.009.

[124] N. Bonora, On the Effect of Triaxial State of Stress on Ductility Using Nonlinear CDM Model, Int. J. Fract. (1998). doi:10.1023/A:1007479522972.

[125] X. Wang, J.A. Muñiz-Lerma, O. Sánchez-Mata, M.A. Shandiz, M. Brochu, Microstructure and mechanical properties of stainless steel 316L vertical struts manufactured by laser powder bed fusion process, Mater. Sci. Eng. A. 736 (2018) 27–40. doi:https://doi.org/10.1016/j.msea.2018.08.069.

[126] K. Guan, Z. Wang, M. Gao, X. Li, X. Zeng, Effects of processing parameters on tensile properties of selective laser melted 304 stainless steel, Mater. Des. (2013). doi:10.1016/j.matdes.2013.03.056.

[127] M. Simonelli, Y.Y. Tse, C. Tuck, Effect of the build orientation on the mechanical properties and fracture modes of SLM Ti–6Al–4V, Mater. Sci. Eng. A. 616 (2014) 1–11. doi:https://doi.org/10.1016/j.msea.2014.07.086.

[128] L.N. Carter, C. Martin, P.J. Withers, M.M. Attallah, The influence of the laser scan strategy on

grain structure and cracking behaviour in SLM powder-bed fabricated nickel superalloy, J. Alloys Compd. (2014). doi:10.1016/j.jallcom.2014.06.172.

[129]   Y. Lu, S. Wu, Y. Gan, T. Huang, C. Yang, L. Junjie, J. Lin, Study on the microstructure, mechanical property and residual stress of SLM Inconel-718 alloy manufactured by differing island scanning strategy, Opt. Laser Technol. 75 (2015) 197–206. doi:10.1016/j.optlastec.2015.07.009.

[130]   B. Song, S. Dong, S. Deng, H. Liao, C. Coddet, Microstructure and tensile properties of iron parts fabricated by selective laser melting, Opt. Laser Technol. 56 (2014) 451–460. doi:10.1016/j.optlastec.2013.09.017.

[131]   A. Keshavarzkermani, E. Marzbanrad, R. Esmaeilizadeh, Y. Mahmoodkhani, U. Ali, P.D. Enrique, N.Y. Zhou, A. Bonakdar, E. Toyserkani, An investigation into the effect of process parameters on melt pool geometry, cell spacing, and grain refinement during laser powder bed fusion, Opt. Laser Technol. 116 (2019) 83–91. doi:10.1016/j.optlastec.2019.03.012.

[132]   ASTM, ASTM E112-13: Standard test methods for determining average grain size, ASTM Int. (2013). doi:10.1520/E0112-13.1.4.

[133]   N. Hansen, Hall--Petch relation and boundary strengthening, Scr. Mater. 51 (2004) 801–806.

[134]   L.L. Shaw, A.L. Ortiz, J.C. Villegas, Hall--Petch relationship in a nanotwinned nickel alloy, Scr. Mater. 58 (2008) 951–954.

[135]   W. Kurz, B. Giovanola, R. Trivedi, Theory of microstructural development during rapid solidification, Acta Metall. (1986). doi:10.1016/0001-6160(86)90056-8.

[136]   W.E. Frazier, Metal additive manufacturing: A review, J. Mater. Eng. Perform. 23 (2014) 1917–1928. doi:10.1007/s11665-014-0958-z.

[137]   A. Hadadzadeh, B.S. Amirkhiz, S. Shakerin, J. Kelly, J. Li, M. Mohammadi, Microstructural investigation and mechanical behavior of a two-material component fabricated through selective laser melting of AlSi10Mg on an Al-Cu-Ni-Fe-Mg cast alloy substrate, Addit. Manuf. 31 (2020) 100937. doi:10.1016/j.addma.2019.100937.

[138]   U. Ali, R. Esmaeilizadeh, F. Ahmed, D. Sarker, W. Muhammad, A. Keshavarzkermani, Y. Mahmoodkhani, E. Marzbanrad, E. Toyserkani, Identification and characterization of spatter particles and their effect on surface roughness, density and mechanical response of 17-4 PH stainless steel laser powder-bed fusion parts, Mater. Sci. Eng. A. 756 (2019) 98–107.

doi:10.1016/j.msea.2019.04.026.

[139] F. Ahmed, U. Ali, D. Sarker, E. Marzbanrad, K. Choi, Y. Mahmoodkhani, E. Toyserkani, Study of powder recycling and its effect on printed parts during laser powder-bed fusion of 17-4 PH stainless steel, J. Mater. Process. Technol. 278 (2020) 116522. doi:10.1016/j.jmatprotec.2019.116522.

[140] M. Salarian, H. Asgari, M. Vlasea, Pore space characteristics and corresponding effect on tensile properties of Inconel 625 fabricated via laser powder bed fusion, Mater. Sci. Eng. A. 769 (2020) 138525. doi:10.1016/j.msea.2019.138525.

[141] A. du Plessis, I. Yadroitsava, I. Yadroitsev, Effects of defects on mechanical properties in metal additive manufacturing: A review focusing on X-ray tomography insights, Mater. Des. 187 (2020) 108385. doi:10.1016/j.matdes.2019.108385.

[142] Y. Mahmoodkhani, U. Ali, F. Liravi, R. Esmaeilizadeh, E. Marzbanrad, Determination of the Most Contributing Laser Powder Bed Fusion Process Parameters on the Surface Roughness Quality of Hastelloy X Components, Glob. Power Propuls. Soc. (2018) 1–8.

[143] Y. Mahmoodkhani, U. Ali, S. Imani Shahabad, A. Rani Kasinathan, R. Esmaeilizadeh, A. Keshavarzkermani, E. Marzbanrad, E. Toyserkani, On the measurement of effective powder layer thickness in laser powder-bed fusion additive manufacturing of metals, Prog. Addit. Manuf. (2018). doi:10.1007/s40964-018-0064-0.

[144] R. Esmaeilizadeh, A. Keshavarzkermani, U. Ali, Y. Mahmoodkhani, B. Behravesh, H. Jahed, A. Bonakdar, E. Toyserkani, Customizing mechanical properties of additively manufactured Hastelloy X parts by adjusting laser scanning speed, J. Alloys Compd. 812 (2020). doi:10.1016/j.jallcom.2019.152097.

[145] A. Keshavarzkermani, R. Esmaeilizadeh, U. Ali, P.D. Enrique, Y. Mahmoodkhani, N.Y. Zhou, A. Bonakdar, E. Toyserkani, Controlling mechanical properties of additively manufactured hastelloy X by altering solidification pattern during laser powder-bed fusion, Mater. Sci. Eng. A. 762 (2019) 138081. doi:10.1016/j.msea.2019.138081.

[146] A. Hadadzadeh, B.S. Amirkhiz, J. Li, M. Mohammadi, Columnar to equiaxed transition during direct metal laser sintering of AlSi10Mg alloy: Effect of building direction, Addit. Manuf. 23 (2018) 121–131. doi:10.1016/j.addma.2018.08.001.

[147] S.I. Shahabad, Z. Zhang, A. Keshavarzkermani, U. Ali, Y. Mahmoodkhani, R. Esmaeilizadeh, A.

Bonakdar, E. Toyserkani, Heat source model calibration for thermal analysis of laser powder-bed fusion, Int. J. Adv. Manuf. Technol. 106 (2020) 3367–3379. doi:10.1007/s00170-019-04908-3.

[148] H. Torbati-sarraf, I. Ghamarian, B. Poorganji, S.A. Torbati-sarraf, An Investigation on the role of crystallographic texture on anisotropic electrochemical behavior of a commercially pure nickel manufactured by laser powder b e d fusion (L-PBF) additive, Electrochim. Acta. 354 (2020) 136694. doi:10.1016/j.electacta.2020.136694.

[149] M.L. Montero-Sistiaga, Z. Liu, L. Bautmans, S. Nardone, G. Ji, J.P. Kruth, J. Van Humbeeck, K. Vanmeensel, Effect of temperature on the microstructure and tensile properties of micro-crack free hastelloy X produced by selective laser melting, Addit. Manuf. 31 (2020) 100995. doi:10.1016/j.addma.2019.100995.

[150] D. Tomus, P.A. Rometsch, M. Heilmaier, X. Wu, Effect of minor alloying elements on crack-formation characteristics of Hastelloy-X manufactured by selective laser melting, Addit. Manuf. 16 (2017) 65–72. doi:10.1016/j.addma.2017.05.006.

[151] S. Rosenthal, S. Platt, R. Hölker-Jäger, S. Gies, S. Kleszczynski, A.E. Tekkaya, G. Witt, Forming properties of additively manufactured monolithic Hastelloy X sheets, Mater. Sci. Eng. A. 753 (2019) 300–316. doi:10.1016/j.msea.2019.03.035.

[152] R. Fadida, A. Shirizly, D. Rittel, The static and dynamic shear-tension mechanical response of AM Ti6Al4V containing spherical and prolate voids, Int. J. Eng. Sci. 141 (2019) 1–15. doi:10.1016/j.ijengsci.2019.05.003.

[153] R. Fadida, A. Shirizly, D. Rittel, Dynamic tensile response of additively manufactured Ti6Al4V with embedded spherical pores, J. Appl. Mech. Trans. ASME. 85 (2018) 1–10. doi:10.1115/1.4039048.

[154] H. Torbati-sarraf, S.A. Torbati-sarraf, N. Chawla, A. Poursaee, A comparative study of corrosion behavior of an additively manufactured Al-6061 RAM2 with extruded Al-6061 T6, Corros. Sci. 174 (2020) 108838. doi:10.1016/j.corsci.2020.108838.

[155] T. Nicholas, High cycle fatigue: a mechanics of materials perspective, Elsevier, 2006.

[156] A. Yadollahi, N. Shamsaei, Additive manufacturing of fatigue resistant materials: Challenges and opportunities, Int. J. Fatigue. 98 (2017) 14–31. doi:10.1016/j.ijfatigue.2017.01.001.

[157] A. Fatemi, R. Molaei, N. Phan, Multiaxial Fatigue of Additive Manufactured Metals: Performance, Analysis, and Applications, Int. J. Fatigue. 134 (2020) 105479.

doi:10.1016/j.ijfatigue.2020.105479.

[158] M. Hamidi Nasab, S. Romano, D. Gastaldi, S. Beretta, M. Vedani, Combined effect of surface anomalies and volumetric defects on fatigue assessment of AlSi7Mg fabricated via laser powder bed fusion, Addit. Manuf. (2019) 100918. doi:10.1016/j.addma.2019.100918.

[159] P.D. Enrique, A. Keshavarzkermani, R. Esmaeilizadeh, S. Peterkin, H. Jahed, E. Toyserkani, N.Y. Zhou, Enhancing fatigue life of additive manufactured parts with electrospark deposition post-processing, Addit. Manuf. 36 (2020) 101526. doi:10.1016/j.addma.2020.101526.

[160] P. Edwards, M. Ramulu, Fatigue performance evaluation of selective laser melted Ti-6Al-4V, Mater. Sci. Eng. A. 598 (2014) 327–337. doi:10.1016/j.msea.2014.01.041.

[161] J. Pegues, M. Roach, R. Scott Williamson, N. Shamsaei, Surface roughness effects on the fatigue strength of additively manufactured Ti-6Al-4V, Int. J. Fatigue. 116 (2018) 543–552. doi:10.1016/j.ijfatigue.2018.07.013.

[162] J.W. Pegues, N. Shamsaei, M.D. Roach, R.S. Williamson, Fatigue life estimation of additive manufactured parts in the as-built surface condition, Mater. Des. Process. Commun. 1 (2019) e36. doi:10.1002/mdp2.36.

[163] P.D. Nezhadfar, R. Shrestha, N. Phan, N. Shamsaei, Fatigue behavior of additively manufactured 17-4 PH stainless steel: Synergistic effects of surface roughness and heat treatment, Int. J. Fatigue. 124 (2019) 188–204. doi:10.1016/j.ijfatigue.2019.02.039.

[164] B. Ellyson, M. Brochu, M. Brochu, Characterization of bending vibration fatigue of SLM fabricated Ti-6Al-4V, Int. J. Fatigue. 99 (2017) 25–34. doi:10.1016/j.ijfatigue.2017.02.005.

[165] F. Wang, X.H. Wu, D. Clark, F. Wang, X.H. Wu, D. Clark, On direct laser deposited Hastelloy X : dimension , surface finish , microstructure and mechanical properties, 0836 (2011). doi:10.1179/026708309X12578491814591.

[166] M.. Montero-Sistiaga, N.M. Dhansay, L. Bautmans, S. Nardone, T.H. Becker, J.-P. Kruth, K. Vanmeensel, Fatigue performance of micro-crack free Hastelloy X produced by selective laser melting (SLM), Eur. Conf. Struct. Integr. Addit. Manuf. Mater. (2019) 9–11.

[167] D.B. Witkin, T. V. Albright, D.N. Patel, Empirical Approach to Understanding the Fatigue Behavior of Metals Made Using Additive Manufacturing, Metall. Mater. Trans. A Phys. Metall. Mater. Sci. 47 (2016) 3823–3836. doi:10.1007/s11661-016-3501-z.

[168] R. Shrestha, J. Simsiriwong, N. Shamsaei, Fatigue behavior of additive manufactured 316L stainless steel parts: Effects of layer orientation and surface roughness, Addit. Manuf. 28 (2019) 23–38. doi:10.1016/j.addma.2019.04.011.

[169] ASTM (American Society for Testing and Materials), E466 standard Practice for Conducting Force Controlled Constant Amplitude Axial Fatigue Tests of Metallic Materials, Test. 03 (2002) 4–8. doi:10.1520/E0466-07.2.

[170] L. Locati, Fatigue and other tests with progressively increasing load, Eng. Dig. 20 (1959).

[171] Y. Jiao, W. He, X. Shen, Enhanced high cycle fatigue resistance of Ti-17 titanium alloy after multiple laser peening without coating, Int. J. Adv. Manuf. Technol. 104 (2019) 1333–1343. doi:10.1007/s00170-019-03993-8.

[172] T. Nicholas, Step loading for very high cycle fatigue, Fatigue Fract. Eng. Mater. Struct. 25 (2002) 861–869. doi:10.1046/j.1460-2695.2002.00555.x.

[173] M.S. Pham, B. Dovgyy, P.A. Hooper, C.M. Gourlay, A. Piglione, The role of side-branching in microstructure development in laser powder-bed fusion, Nat. Commun. (n.d.) 1–12. doi:10.1038/s41467-020-14453-3.

[174] O. Sanchez-Mata, X. Wang, J.A. Muñiz-Lerma, M.A. Shandiz, R. Gauvin, M. Brochu, Fabrication of crack-free nickel-based superalloy considered non-weldable during laser powder bed fusion, Materials (Basel). 11 (2018) 1–9. doi:10.3390/ma11081288.

[175] J.M. Jeon, J.M. Park, J.H. Yu, J.G. Kim, Y. Seong, S.H. Park, H.S. Kim, Effects of microstructure and internal defects on mechanical anisotropy and asymmetry of selective laser-melted 316L austenitic stainless steel, Mater. Sci. Eng. A. 763 (2019) 138152. doi:10.1016/j.msea.2019.138152.

[176] J. Polák, V. Mazánová, M. Heczko, R. Petráš, I. Kuběna, L. Casalena, J. Man, The role of extrusions and intrusions in fatigue crack initiation, Eng. Fract. Mech. 185 (2017) 46–60. doi:10.1016/j.engfracmech.2017.03.006.

[177] H. Jiang, P. Bowen, J.F. Knott, Fatigue performance of a cast aluminium alloy Al-7Si-Mg with surface defects, J. Mater. Sci. 34 (1999) 719–725. doi:10.1023/A:1004560510632.

[178] U.C. Nwaogu, N.S. Tiedje, H.N. Hansen, A non-contact 3D method to characterize the surface roughness of castings, J. Mater. Process. Technol. 213 (2013) 59–68. doi:10.1016/j.jmatprotec.2012.08.008.

[179] B. Vayssette, N. Saintier, C. Brugger, M. El May, E. Pessard, Numerical modelling of surface roughness effect on the fatigue behavior of Ti-6Al-4V obtained by additive manufacturing, Int. J. Fatigue. 123 (2019) 180–195. doi:10.1016/j.ijfatigue.2019.02.014.

[180] Y. Tian, D. Tomus, P. Rometsch, X. Wu, Influences of processing parameters on surface roughness of Hastelloy X produced by selective laser melting, Addit. Manuf. 13 (2017) 103–112. doi:10.1016/j.addma.2016.10.010.

[181] L. Tonelli, A. Fortunato, L. Ceschini, CoCr alloy processed by Selective Laser Melting (SLM): effect of Laser Energy Density on microstructure, surface morphology, and hardness, J. Manuf. Process. 52 (2020) 106–119. doi:10.1016/j.jmapro.2020.01.052.

[182] R. Shrestha, N. Shamsaei, M. Seifi, N. Phan, An investigation into specimen property to part performance relationships for laser beam powder bed fusion additive manufacturing, Addit. Manuf. 29 (2019). doi:10.1016/j.addma.2019.100807.

[183] J.D. Carroll, W.Z. Abuzaid, J. Lambros, H. Sehitoglu, On the interactions between strain accumulation, microstructure, and fatigue crack behavior, Int. J. Fract. 180 (2013) 223–241. doi:10.1007/s10704-013-9813-8.

[184] P. Behjati, S. Asgari, Microstructural characterisation of deformation behaviour of nickel base superalloy IN625, Mater. Sci. Technol. 27 (2011) 1858–1862. doi:10.1179/1743284711Y.0000000056.

[185] L. Liu, Q. Ding, Y. Zhong, J. Zou, J. Wu, Y.L. Chiu, J. Li, Z. Zhang, Q. Yu, Z. Shen, Dislocation network in additive manufactured steel breaks strength–ductility trade-off, Mater. Today. 21 (2018) 354–361. doi:10.1016/j.mattod.2017.11.004.

[186] E. El-Danaf, S.R. Kalidindi, R.D. Doherty, Influence of grain size and stacking-fault energy on deformation twinning in fcc metals, Metall. Mater. Trans. A Phys. Metall. Mater. Sci. 30 (1999) 1223–1233. doi:10.1007/s11661-999-0272-9.

[187] M. Zhang, C.N. Sun, X. Zhang, J. Wei, D. Hardacre, H. Li, High cycle fatigue and ratcheting interaction of laser powder bed fusion stainless steel 316L: Fracture behaviour and stress-based modelling, Int. J. Fatigue. 121 (2019) 252–264. doi:10.1016/j.ijfatigue.2018.12.016.

[188] S.K. Paul, A critical review of experimental aspects in ratcheting fatigue: Microstructure to specimen tocomponent, J. Mater. Res. Technol. (2019) 1–21. doi:10.1016/j.jmrt.2019.06.014.

[189] T. Hassan, S. Kyriakides, Ratcheting in cyclic plasticity, part I: uniaxial behavior, Int. J. Plast. 8

(1992) 91–116.

[190] M. Noban, H. Jahed, Ratchetting strain prediction, Int. J. Press. Vessel. Pip. 84 (2007) 223–233. doi:10.1016/j.ijpvp.2006.10.003.

[191] Y.C. Chiou, J.K. Yang, The effects of pre-deformation on the subsequent fatigue behaviors of SUS 430 Stainless Steel in load-control, Int. J. Solids Struct. 49 (2012) 3263–3268. doi:10.1016/j.ijsolstr.2012.06.023.

[192] H.Y. Wan, Z.J. Zhou, C.P. Li, G.F. Chen, G.P. Zhang, Effect of scanning strategy on mechanical properties of selective laser melted Inconel 718, Mater. Sci. Eng. A. 753 (2019) 42–48. doi:10.1016/j.msea.2019.03.007.

[193] W. Ren, T. Nicholas, Effects and mechanisms of low cycle fatigue and plastic deformation on subsequent high cycle fatigue limit in nickel-base superalloy Udimet 720, Mater. Sci. Eng. A. 332 (2002) 236–248. doi:10.1016/S0921-5093(01)01742-7.

[194] G.E. Dieter, D.J. Bacon, Mechanical metallurgy, McGraw-hill New York, 1986.

[195] Z. Liao, B. Yang, Y. Qin, S. Xiao, G. Yang, T. Zhu, N. Gao, Short fatigue crack behaviour of LZ50 railway axle steel under multi-axial loading in low-cycle fatigue, Int. J. Fatigue. 132 (2020) 105366. doi:10.1016/j.ijfatigue.2019.105366.

[196] P. Gauthier, H. De Rabaudy, J. Auvinet, Secondary cracking process during fatigue crack propagation, Eng. Fract. Mech. 5 (1973) 977–981. doi:10.1016/0013-7944(73)90062-3.

[197] P. Karimi, E. Sadeghi, J. Ålgårdh, J. Andersson, EBM-manufactured single tracks of Alloy 718 : In fl uence of energy input and focus o ff set on geometrical and microstructural characteristics, Mater. Charact. 148 (2019) 88–99. doi:10.1016/j.matchar.2018.11.033.

[198] E. Hosseini, V.A. Popovich, A review of mechanical properties of additively manufactured Inconel 718, Addit. Manuf. 30 (2019) 100877. doi:10.1016/j.addma.2019.100877.

[199] A. Keshavarzkermani, R. Esmaeilizadeh, P.D. Enrique, H. Asgari, N.Y. Zhou, A. Bonakdar, E. Toyserkani, Materials Characterization Static recrystalization impact on grain structure and mechanical properties of heat-treated Hastelloy X produced via laser powder-bed fusion, Mater. Charact. 173 (2021) 110969. doi:10.1016/j.matchar.2021.110969.

[200] M. Jin, A. Piglione, B. Dovgyy, E. Hosseini, P.A. Hooper, S.R. Holdsworth, M.S. Pham, Cyclic plasticity and fatigue damage of CrMnFeCoNi high entropy alloy fabricated by laser powder-bed

fusion, Addit. Manuf. 36 (2020) 101584. doi:10.1016/j.addma.2020.101584.

[201] H. Brooks, K. Brigden, Design of conformal cooling layers with self-supporting lattices for additively manufactured tooling, Addit. Manuf. 11 (2016) 16–22. doi:10.1016/j.addma.2016.03.004.

[202] P. Karimi, C. Schnur, E. Sadeghi, J. Andersson, Contour design to improve topographical and microstructural characteristics of Alloy 718 manufactured by electron beam-powder bed fusion technique, Addit. Manuf. 32 (2020) 101014. doi:10.1016/j.addma.2019.101014.

[203] Y. Wang, L. Zhang, S. Daynes, H. Zhang, S. Feih, M. Yu, Design of graded lattice structure with optimized mesostructures for additive manufacturing, Mater. Des. 142 (2018) 114–123. doi:10.1016/j.matdes.2018.01.011.

[204] E. Sadeghi, P. Karimi, S. Momeni, M. Seifi, A. Eklund, Materials Characterization Influence of thermal post treatments on microstructure and oxidation behavior of EB-PBF manufactured Alloy 718, Mater. Charact. 150 (2019) 236–251. doi:10.1016/j.matchar.2019.02.016.

[205] S.E. Aghili, M. Shamanian, R. Amini Najafabadi, A. Keshavarzkermani, R. Esmaeilizadeh, U. Ali, E. Marzbanrad, E. Toyserkani, Microstructure and oxidation behavior of NiCr-chromium carbides coating prepared by powder-fed laser cladding on titanium aluminide substrate, Ceram. Int. 46 (2020) 1668–1679. doi:10.1016/j.ceramint.2019.09.139.

[206] A.P. Jirandehi, M. Mehdizadeh, M.M. Khonsari, International Journal of Mechanical Sciences Temperature-induced buckling of ductile metals during cyclic loading and the subsequent early fracture, Int. J. Mech. Sci. 176 (2020) 105525. doi:10.1016/j.ijmecsci.2020.105525.

[207] S. Lee, J.W. Pegues, N. Shamsaei, Fatigue Behavior and Modeling for Additive Manufactured 304L Stainless Steel : The effect of Surface Roughness, Int. J. Fatigue. (2020) 105856. doi:10.1016/j.ijfatigue.2020.105856.

[208] S. Romano, L. Patriarca, S. Foletti, S. Beretta, LCF behaviour and a comprehensive life prediction model for AlSi10Mg obtained by SLM, Int. J. Fatigue. 117 (2018) 47–62. doi:10.1016/j.ijfatigue.2018.07.030.

[209] R. Branco, J.D.M. Costa, F. Berto, S. Mohammad, J. Razavi, A.M. Ferreira, C. Capela, F. Antunes, Low-Cycle Fatigue Behaviour of AISI 18Ni300 Maraging Steel Produced by Selective Laser Melting, (2018). doi:10.3390/met8010032.

[210] T. Lindström, M. Calmunger, R. Eriksson, D. Leidermark, Fatigue behaviour of an additively

manufactured ductile gas turbine superalloy, Theor. Appl. Fract. Mech. (2020) 102604. doi:10.1016/j.tafmec.2020.102604.

[211] T. Lindstrom, D. Ewest, K. Simonsson, R. Eriksson, J. Lundgren, D. Leidermark, Constitutive model of an additively manufactured ductile nickel-based superalloy undergoing cyclic plasticity, Int. J. Plast. (2020) 102752. doi:10.1016/j.ijplas.2020.102752.

[212] A. E606/E606M-12, Standard test method for strain-controlled fatigue testing, (2012).

[213] R. Esmaeilizadeh, A. Keshavarzkermani, U. Ali, B. Behravesh, A. Bonakdar, H. Jahed, E. Toyserkani, On the effect of laser powder-bed fusion process parameters on quasi-static and fatigue behaviour of Hastelloy X: A microstructure/defect interaction study, Addit. Manuf. 38 (2021) 101805. doi:10.1016/j.addma.2020.101805.

[214] D.H. Smith, J. Bicknell, L. Jorgensen, B.M. Patterson, N.L. Cordes, I. Tsukrov, M. Knezevic, Materials Characterization Microstructure and mechanical behavior of direct metal laser sintered Inconel alloy 718, Mater. Charact. 113 (2016) 1–9. doi:10.1016/j.matchar.2016.01.003.

[215] W. Chen, T. Voisin, Y. Zhang, J. Florien, C.M. Spadaccini, D.L. Mcdowell, T. Zhu, Y.M. Wang, Microscale residual stresses in additively manufactured stainless steel, Nat. Commun. (n.d.) 1–12. doi:10.1038/s41467-019-12265-8.

[216] S. Pourbabak, M.L. Montero-Sistiaga, D. Schryvers, J. Van Humbeeck, K. Vanmeensel, Microscopic investigation of as built and hot isostatic pressed Hastelloy X processed by Selective Laser Melting, Mater. Charact. 153 (2019) 366–371. doi:10.1016/j.matchar.2019.05.024.

[217] G. Wang, H. Ouyang, C. Fan, Q. Guo, Z. Li, W. Yan, The origin of high-density dislocations in additively manufactured metals, 3831 (2020). doi:10.1080/21663831.2020.1751739.

[218] K.M. Bertsch, G.M. De Bellefon, B. Kuehl, D.J. Thoma, Acta Materialia Origin of dislocation structures in an additively manufactured austenitic stainless steel 316L, Acta Mater. 199 (2020) 19–33. doi:10.1016/j.actamat.2020.07.063.

[219] X. Wang, L.N. Carter, B. Pang, M.M. Attallah, M.H. Loretto, Acta Materialia Microstructure and yield strength of SLM-fabricated CM247LC, Acta Mater. 128 (2017) 87–95. doi:10.1016/j.actamat.2017.02.007.

[220] W. Ramberg, W.R. Osgood, Description of stress-strain curves by three parameters, (1943).

[221] G.V.P. Reddy, P. Harini, R. Sandhya, K.B. Sankara, R.K. Paretkar, On dual-slope linear cyclic

hardening of Hastelloy X, Mater. Sci. Eng. A. 527 (2010) 3848–3851. doi:10.1016/j.msea.2010.02.062.

[222] R.L. Mcdaniels, L. Chen, R. Steward, P.K. Liaw, R.A. Buchanan, S. White, K. Liaw, D.L. Klarstrom, The strain-controlled fatigue behavior and modeling of Haynes ® HASTELLOY ® C-2000 ® superalloy, 528 (2011) 3952–3960. doi:10.1016/j.msea.2010.10.024.

[223] M.D. Sangid, The physics of fatigue crack initiation, Int. J. Fatigue. 57 (2013) 58–72. doi:10.1016/j.ijfatigue.2012.10.009.

[224] S.M.H. Karparvarfard, S.K. Shaha, S.B. Behravesh, H. Jahed, B.W. Williams, Fatigue characteristics and modeling of cast and cast-forged ZK60 magnesium alloy, Int. J. Fatigue. 118 (2019) 282–297. doi:10.1016/j.ijfatigue.2018.03.019.

[225] J. Bannantine, J.J. Comer, H.J. L, Fundamentals of metal fatigue analysis((Book)), Res. Support. by Univ. Illinois. Englewood Cliffs, NJ, Prentice Hall, 1990, 286. (1990).

[226] S.S. Manson, M.H. Hirschberg, Fatigue: an interdisciplinary approach, in: Proc. X Sagamare Army Mater. Res. Conf. Univ. Press., 1964: p. 133.

[227] N.E. Dowling, Mechanical behavior of materials: engineering methods for deformation, fracture, and fatigue, Pearson, 2012.

[228] A. E73910, Standard practice for statistical analysis of linear or linearized stress-life (SN) and strain-life (ε-N) fatigue data, (2015).

[229] K. Smith, P. Watson, T. Topper, A stress-strain function for the fatigue of metals, J. Mater. 5 (1970) 767–778.

[230] H. Jahed, A. Varvani-Farahani, M. Noban, I. Khalaji, An energy-based fatigue life assessment model for various metallic materials under proportional and non-proportional loading conditions, Int. J. Fatigue. 29 (2007) 647–655. doi:10.1016/j.ijfatigue.2006.07.017.

[231] A.A. Roostaei, A. Pahlevanpour, S.B. Behravesh, H. Jahed, On the definition of elastic strain energy density in fatigue modelling, Int. J. Fatigue. 121 (2019) 237–242.

[232] J.W. Pegues, S. Shao, N. Shamsaei, N. Sanaei, A. Fatemi, D.H. Warner, P. Li, N. Phan, Fatigue of additive manufactured Ti-6Al-4V , Part I : The effects of powder feedstock , manufacturing , and post-process conditions on the resulting microstructure and defects, 132 (2020). doi:10.1016/j.ijfatigue.2019.105358.

[233] R. Molaei, A. Fatemi, N. Sanaei, J. Pegues, N. Shamsaei, S. Shao, P. Li, D.H. Warner, N. Phan, Fatigue of additive manufactured Ti-6Al-4V , Part II : The relationship between microstructure , material cyclic properties , and component performance Theory of Critical Distance, 132 (2020). doi:10.1016/j.ijfatigue.2019.105363.

[234] Y. Murakami, Material defects as the basis of fatigue design, Int. J. Fatigue. 41 (2012) 2–10. doi:10.1016/j.ijfatigue.2011.12.001.

[235] C.R. Williams, Y. Lee, J.T. Rilly, A practical method for statistical analysis of strain – life fatigue data, 25 (2005) 427–436. doi:10.1016/S0142-1123(02)00119-6.

[236] C.L. Shen, P.H. Wirsching, G.T. Cashman, Design Curve to Characterize Fatigue Strength, 118 (1996).

[237] B.F. Langer, Design of pressure vessels for low-cycle fatigue, (1962).

[238] Y.-L. Lee, J. Pan, R. Hathaway, M. Barkey, Fatigue testing and analysis: theory and practice, Butterworth-Heinemann, 2005.